Camera-based close-range coordinate metrology

University of Nottingham
UK | CHINA | MALAYSIA

Danny Sims-Waterhouse

Faculty of Engineering

University of Nottingham

This dissertation is submitted for the degree of

Doctor of Philosophy

September 2019

I would like to dedicate this thesis to my family. Without their unwavering support, this would not have been possible.

Acknowledgements

I would like to acknowledge Richard Leach and Samanta Piano for their vital supervision throughout the PhD project.

I would also like to thank my colleagues and friends for their support and technical expertise throughout my PhD. This includes Patrick Bointon, Sofia Catalucci, Amrozia Shaheen, Joe Eastwood and Mohammed Isa.

Abstract

The main focus of this thesis was on the development of techniques and methodologies to allow the effective application of photogrammetry to coordinate metrology. The current understanding of the propagation of uncertainty through camera-based measurement systems is limited due to the highly complex and non-linear nature of the techniques. Additionally, the application of existing verification standards is unclear and difficult to apply directly to high-accuracy photogrammetry systems. The aim of this work was, therefore, to develop techniques to evaluate the coordinate measurement uncertainty of photogrammetry systems as well methods that allow existing verification standards to be effectively applied.

Based on Monte Carlo simulations, an evaluation of the contributing factors to the expanded uncertainty on measurements made by a stereo photogrammetry system was performed. A traceable scaling methodology was also applied to the stereo system, allowing the identification of the key contributing factors to the stereo system measurement to be highlighted and targeted for future. Additionally, the effect of systematic errors on the measurement volume was simulated and then verified through experimental observations.

A laser speckle texture projection methodology was also developed in order to allow existing verification standards to be applied to conventional photogrammetry systems. By projecting artificial texture onto the verification artefact surface, the verification outlined in the VDI/VDE 2634 part 3 standards were applied. The

results of the verification tests demonstrated the high levels of accuracy that can be achieved by photogrammetry based coordinate measurement systems.

Through the use of fringe projection techniques, an additional method of applying verification standards to a stereo photogrammetry system was also performed. By using phase encoding to find correspondence between cameras, the verification tests were applied and were in agreement with predicted values. Additionally, the use of phase encoded correspondence also presents a promising method to vastly improve the accuracy of the characterisation of stereo system properties.

Finally, the principles of photogrammetry were applied to several case studies. The photogrammetry principles developed in this thesis were used to develop data fusion methods to greatly improve the bandwidth of measurements, use laser speckle to produce material agnostic measurements of part geometry and calibrate reconstruction scale factors using light-field imaging principles.

Table of contents

List of figures

List of tables

Chapter 1

Introduction

1.1 Motivation

The ability to precisely and accurately measure the geometry of parts has always been the limiting factor in manufacturing. Ensuring manufactured parts are within tolerance is key in guaranteeing that parts will fit within assemblies, reducing wasted material and energy, prolonging part life-time and providing confidence in that part for potential customers. As a result, coordinate metrology forms a key foundation in modern high precision manufacturing.

Contact-based coordinate measurement machines have been common place in metrology labs for several decades, and as such, are very well understood and trusted. However, there is an increasing complexity of parts that are able to be manufactured that require large numbers of measured points in order to ensure the part is within tolerance. Contact-based coordinate metrology systems are highly accurate, but are inherently slow when a large number of points must be acquired. However, in more recent years, non-contact optical methods of coordinate measurement are becoming more widely used in industrial settings in order to measure highly complex parts.

Although optical coordinate measurement systems, such as laser triangulation, fringe projection and photogrammetry, are becoming more prevalent, they are still less well understood than contact techniques. Understanding the complex interactions of light with object surfaces and how this affects the coordinate measurement uncertainty of the optical metrology system is a key area of research for the future of coordinate metrology.

1.2 Aims and objectives

The aim of this work is to develop the technique of photogrammetry for application in coordinate metrology. The key areas targeted are the understanding of the uncertainty, the application of verification standards and accurate scaling of photogrammetry measurements. As such, the aims of this work are to develop a better understanding of the error sources and propagation of uncertainty in photogrammetry measurements, as well as devising a traceable scaling methodology for those measurements. Additionally, methodologies for the implementation of existing verification standards to photogrammetry will be investigated.

In order to achieve a better understanding of the propagation of errors through the photogrammetry measurement process, a computational method of a photogrammetry system will be developed. The computational model will then be used to probe the effect of error sources on the measurement uncertainty. In addition to the computational model development, a methodology for high-accuracy and traceable scaling of the photogrammetry will be outlined. Complimentary to computational modelling, a method for the application of existing verification standards to conventional photogrammetry systems will also be outlined. Specifically, the methods will be developed for a system comprising of a consumer DSLR cameras, as well as a stereo-system of industrial machine vision cameras. Finally,

the methods and knowledge collected from the previous objectives will be applied to a series of case studies, demonstrating the application of photogrammetry in metrology.

1.3 Description of work

Chapter 2 provides a overview of the existing work on the application of photogrammetry to coordinate metrology. The review covers the background of photogrammetry, current research relevant to this work as well as the current state of uncertainty evaluation and verification standards for photogrammetry methods.

Chapter 3 demonstrates the application of Monte Carlo methods in order to evaluate the three dimensional coordinate expanded uncertainty for measurements made by a stereo photogrammetry system. The chapter also covers a methodology for the traceable calibration of the stereo system scale factor, as well as investigating the effect of systematic errors on the system properties in the measurements.

Chapter 4 covers the use of laser speckle texture projection in order to allow the measurement of smooth artefacts that do not exhibit visible texture. The laser speckle texture projection is used to perform verification tests on a standard photogrammetry system demonstrating the high accuracies that photogrammetry is able to achieve.

Chapter 5 presents an alternative method of applying verification standards to photogrammetry systems with optics that do not allow the use of laser speckle texture projection. Additionally, it provides measurement uncertainties in agreement with results from chapter 3 as well as providing some potential work for the improvement of the calibration process.

Chapter 6 presents four case studies in which the photogrammetry systems and techniques presented in earlier chapters have been applied. The case studies include

the development of a portable photogrammetry system for dental anthropology, the fusion of photogrammetry and coherence scanning interferometer data, the use of laser speckle texture projection to measure objects with little observable texture and the fusion of photogrammetry and light-field camera data.

Finally, chapter 7 outlines the current state of photogrammetry for coordinate metrology, describes the contribution of the work covered in this thesis to the field and suggests future work to be done to further advance the technology.

Chapter 2

Background and related work

2.1 Photogrammetry

Photogrammetry is defined by Luhmann et al as the science of measurement through the use of photographs [71]. The main principle of photogrammetry for form measurement is the triangulation of corresponding points using two or more images. Correspondences are determined through a variety of methods, including physical targets or the detection of image features. The measurement of form, in this case, refers to the measurement of the external shape of the object [103]. Stereo-photogrammetry is the most common application of photogrammetry, in which the measurement process is applied using only two images. The simplicity of photogrammetry has meant that it has been used as a method of measurement since photography was invented in the 1830's [71]. For the first fifty years, photogrammetry was mainly used by architects as a fast and easy method of measuring the shape buildings. The nature of the photographic techniques meant that building facade dimensions could be measured without the risk of typically dangerous manual methods in which workers would be exposed hazards. It was not until the late 1800's that the scope of photogrammetry became more wide spread. The develop-

ment of stereo comparators allowed topographic measurements to be made and became invaluable in the mapping of inaccessible mountainous regions [71]. In the first half of the 20th Century this topographic measurement from aerial photography led to significant advancement. However, the use of close-range photogrammetry was yet to be properly developed due to severe instrument limitations and little to no economic incentive [71]. The definition of close-range photogrammetry is not defined, but typically applies to measurement working distances of up to 300 m.

It was not until the rise of digital computers that close-range photogrammetry could truly be considered for accurate close range measurements. The potential of close-range photogrammetry was now only limited by the reconstruction algorithms and imaging process used. As a result, research into reconstruction and calibration algorithms flourished, giving rise to the modern methods seen today. The recent advancements in digital photography have also been significant. Through careful calibration and the equipment, the three-dimensional digitisation of sub-millimetre object features to a three-dimensional point measurement uncertainty of a few microns is possible [39].

2.1.1 Modern stereo-photogrammetry

Although micro-scale measurements are feasible with photogrammetry, modern applications are still predominately applied to much larger scales. For the scope of this work, micro-scale will refer to geometries with features less than a millimetre in size. The non-invasive nature of the method allows for the measurement of objects or surfaces that cannot be physically accessed or are easily damaged. Consequently, photogrammetry is widely used in archaeology, architecture, automotive, aerospace, medicine, and crime scene and accident reconstruction. In archaeology, photogrammetry means that the three-dimensional structure of very

delicate objects and buildings can be measured without physical contact [93]. This means the historical significance of such objects can be determined without the potential to destroy or damage them. During the investigation of an accident or crime there may be a point at which the only remaining evidence is photographic. Photogrammetry allows a scene to be reconstructed in three dimensions from a series of images. Applications of photogrammetry to accident scene modelling date back to as early as 1933 and are still used today [71, 34]. The non-invasive nature of photogrammetry makes it well suited to medical applications. By taking a three-dimensional scan of the human body prior to surgery, photogrammetry can be used to tailor reconstructive surgery to a patient [55]. Augmented reality during surgery can also be implemented to aid surgeons in the accurate removal of tumours. The three-dimensional position of the tumour can be determined and separated from healthy tissue allowing a complete removal [10].

Most relevant to metrological applications are the uses of photogrammetry in automotive and aerospace engineering. Stereo photogrammetry and other optical techniques are widely used as a means of quality control during machining and forming processes [79, 118]. By scanning a component through various techniques, a three-dimensional model can be created from the resulting point cloud. The scan can then be compared against the original CAD model to ensure that the required specifications have been met. Accurately adjusting and measuring mounting rigs and tools is also an important application in both fields. Being able to produce precision manufactured components and highly accurate alignments is critical in modern manufacturing engineering [69].

2.2 Micro-scale and nano-scale manufacturing

Micro- and nanotechnology are now becoming a significant part of industry; the miniaturisation of mechanical components, or even engineering surfaces of larger ones, has become highly desirable. Being able to produce such micro-components in meaningful quantities will have a high impact on manufacturing engineering. In order for micro and nano-manufacturing to become more widely applied, a metrology infrastructure must be in place to ensure the traceability and quality control of such small components.

Micro coordinate measurement machines (micro-CMMs) provide the precision and accuracy required to successfully measure micro-components. The bulk of current methods are based on a touch probe system. Essentially a stylus is moved over a surface and the resulting deflections can be used to determine the topography of the object. Vertical accuracies of around tens of nanometres can be achieved with such methods, however, around a few hundred nanometres is typical [18]. Horizontal accuracies have a high dependence on tip diameter and surface topography, but are typically sub-micrometre. Relative to the depth accuracy of touch probe techniques, the lateral accuracies are significantly lower but appropriate for most applications. The level of accuracy achieved by micro-CMMs is more than adequate to provide a method of verification in micro-scale manufacturing. As each data point must be taken individually, touch probe micro-CMMs are slow taking around a second for each data point. For many thousands of required data points, this rate of measurement is not suitable. The small surface area of the probe also results in high pressures on the surface, potentially resulting in damage to the object [3]. This can be reduced by having very low force probes leading to even longer scan times to stop the probe jumping. The long scan times required make touch probe

methods unsuitable for applications in which a high number of measured points is required.

Fortunately, optical techniques can measure millions of points in just a few seconds without the potential to cause damage. Optical techniques, such confocal [51] and focus variation microscopy [80], can both achieve sub-micrometre accuracies over an area of several millimetres for a single view [22, 48]. Unfortunately, both confocal and focus variation microscopy both have a lateral working range of only a few tens of millimetres. A stitching process can be applied to a series of images, but for a single image no larger scale features can be measured. Although the level of accuracy and speed achieved by confocal and focus variation microscopy is more appropriate for micro-scale applications, the working range is problematic for larger parts.

The application of photogrammetry to the measurement of sub-millimetre features is still early in development, but several applications have already been demonstrated. Gallantucci et al has demonstrated the ability of a photogrammetry system to measure sub-millimetre scale features on a purposely designed artefact [36]. Photogrammetry has also demonstrated its ability to measure the geometry of the channels of micro-fluidic devices in which the channel geometries were on the order of 600 μm deep and a millimetre across [49]. Additionally, photogrammetry has also shown promise in the measurement of palaeontology samples, such as the micro-scale geometries on bones [4].

Structured light based methods can also achieve the required level of accuracy for micro-scale metrology. For example, fringe projection can produce accuracies around a few tens of micrometres over scales of around a metre [88]. Unlike photogrammetry, which relies on passive light sources, structured light based methods instead control the nature of the light in order to ascertain form information. In

fringe projection, this is achieved through the use of a projector and camera, in which the distortion of the projected image can be used to determine the form of the object. The basic principle of fringe projection is shown in figure 2.1. Although fringe projection provides an ideal method of micro-scale measurement, the use of a projector introduces other complications. Fringe projection relies on the projector being aligned accurately with respect to the camera, which can prove difficult [73]. Additionaly, non-linearities between the projector must be corrected for, resulting in additional sources of error [6].

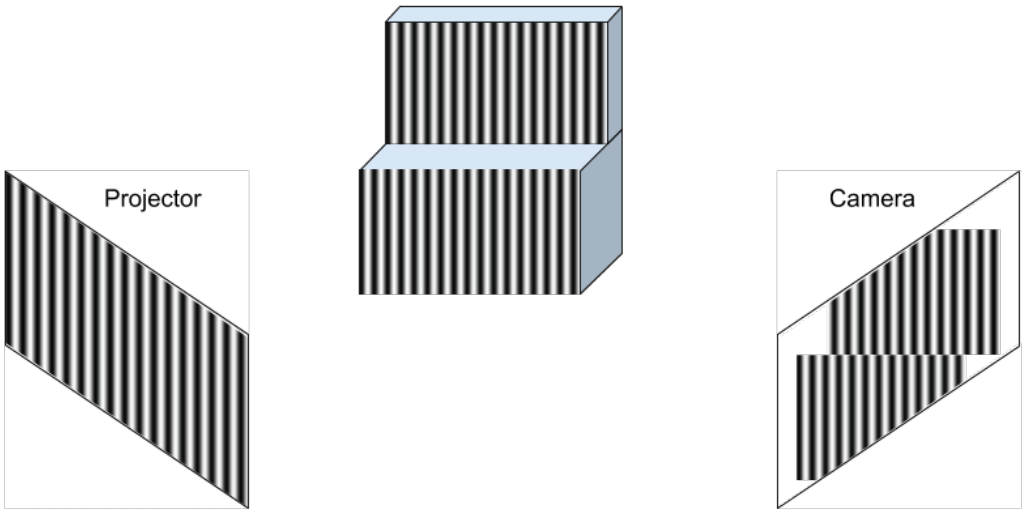

Fig. 2.1 Basic principle of fringe projection.

Highly reflective or transparent materials can also affect the performance of structured light methods due to the specular reflections and sub-surface scattering within the object [35, 64]. Laser triangulation is also widely applied structured light based technique, with applications in a range of industries, with higher accuracies than fringe projection systems [5, 24]. Rather than projecting over the entire part, laser triangulation instead determines the object form through the scanning of a laser over the object and detecting that lasers location within the camera, as shown in figure 2.2. The form of the laser can vary from a single dot to a scanning line.

However, the need to scan the laser over the surface means that laser triangulation methods are typically low-resolution and still suffer from the same surface effects as fringe projection techniques [35, 64].

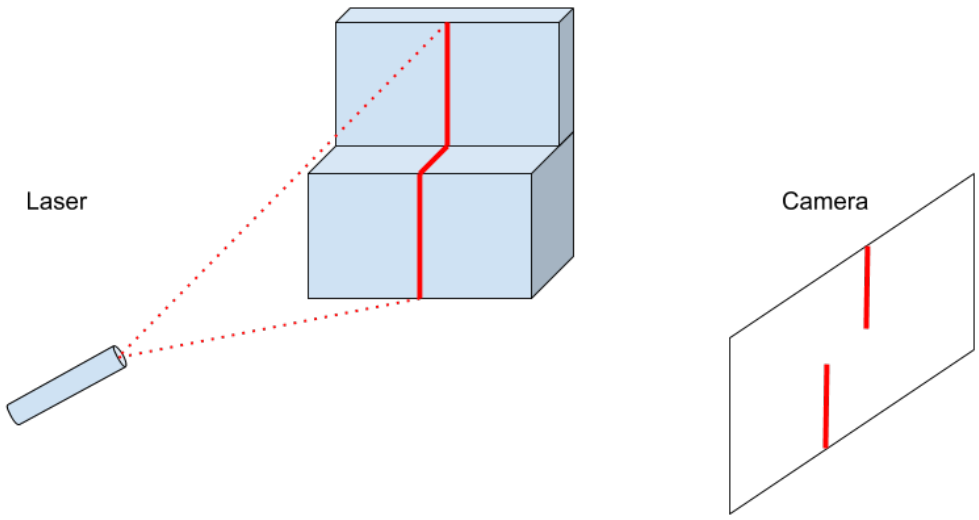

Fig. 2.2 Basic principle of laser triangulation.

2.3 Camera projection theory

2.3.1 Overview

The aim of camera projection theory is to model how three-dimensional space is projected onto a 2D image. Stereo photogrammetry can then, using a camera model, take 2D images and project them back in three-dimensional space to deduce some information about the original object. Unfortunately, the direct transfer from three-dimensional to 2D infers some loss of information. This loss of information is exemplified by the inability of a camera to capture depth information. A point on an image will correspond to any point along a line in space, therefore, when taking an image, the distance along this line is not measured. An object will also

appear smaller or larger depending on how far it is away from the camera. An ambiguity in the depth information captured in an image will, therefore, produce a loss of scale in the lateral directions. It is possible to use corresponding pixels in two or more images from different perspectives to triangulate that point in three-dimensional space based on their projections. This triangulation method forms the main principle of reconstruction in stereo photogrammetry to determine the projection of a pixel. Camera models provide the mathematical basis for the geometric projections and hence must be accurately characterised for accurate three-dimensional reconstruction.

2.3.2 The pinhole camera model

The pinhole camera model forms the basis for the majority of cameras and lenses that exhibit perspective projection. For the most part, depending on the required level of accuracy, only small adaptations are required. Central projection theory describes how an image is formed in a pinhole camera. In essence, a camera can be modelled as a central projection point C and an image plane. A ray can then be projected from a point in three-dimensional space through the projection centre, resulting in an intersection with the imaging plane. This intersection can then be used to calculate the point at which an object at the world coordinates $[x\ y\ z]$ would appear on the image produced by the camera [50]. The principle of central projection is shown in figure 2.3.

For a point X projected through a pinhole at C, the coordinates must first be transformed into the camera coordinates $[x_c, y_c, z_c]$. This transformation can be broken down into two stages. Firstly, a simple translation vector, T, is applied so that the object coordinates are relative to the camera centre of projection. Secondly, a rotation, R, is used to orientate the camera axis with the z axis of the camera

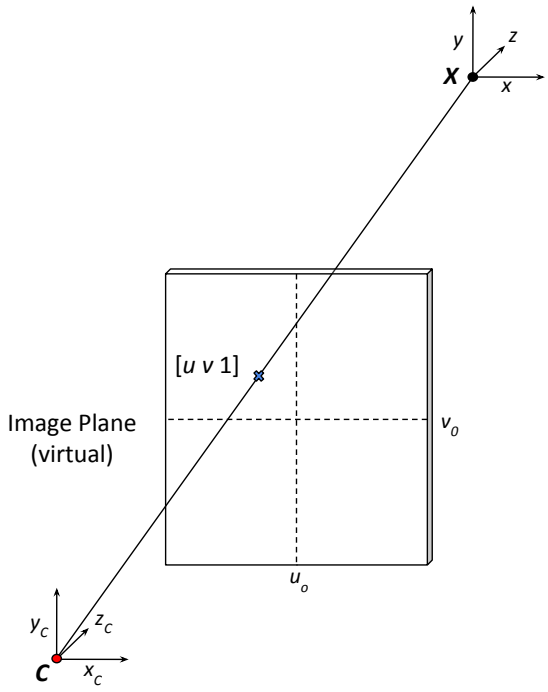

Fig. 2.3 Basic principle of image plane intersection in a pinhole camera. The image plane is labelled as virtual because, although the actual imaging takes place behind the projection centre, the mathematics is simplified by using the virtual image plane.

coordinate system. With the coordinates now in the correct frame, the intrinsic camera matrix, K, can be applied to determine the intersection point of the ray with the imaging plane. This projection is given by

$$t\begin{bmatrix} u \\ v \\ 1 \end{bmatrix} = P\begin{bmatrix} x \\ y \\ z \\ 1 \end{bmatrix} = K\begin{bmatrix} R & T \\ 0 & 1 \end{bmatrix}\begin{bmatrix} x \\ y \\ z \\ 1 \end{bmatrix} \tag{2.1}$$

where $\begin{bmatrix} u & v & 1 \end{bmatrix}^T$ is the intersection point with the imaging sensor, t is a scale factor and $P = K\begin{bmatrix} R & T \\ 0 & 1 \end{bmatrix}$ [131].

The intrinsic camera matrix (K) depends on the internal properties of the camera being used. As a result, properties such as pixel size and the focal length of the lens have a significant impact on the final image. The general form of K is given by

$$K = \begin{bmatrix} k_u & s & u_0 \\ 0 & k_v & v_0 \\ 0 & 0 & 1 \end{bmatrix} \tag{2.2}$$

where k_u and k_v represent the focal lengths in terms of pixels in the u and v directions respectively, u_0 and v_0 are the coordinates of the principle point and s is an additional term describing the skew of the image [125]. The principle point is the point at which the principle axis of the imaging system intersects with the imaging plane. Although it would typically be assumed that the principle point would lie at the centre of the image, small manufacturing errors of the camera body and lens can lead to a slight offset of the optical components. This offset of the

optical components results in the actual principle point being offset from the centre of the camera sensor. Although the offset may be small, it must still be accounted for.

For a pinhole camera, equation 2.1 perfectly describes the image. Unfortunately, with camera optical components, such as lenses, the simple linear relationship given by equation 2.1 no longer accurately describes the imaging process due to image distortions. Many of the cameras required to achieve sub-millimetre resolutions use optical components that result in such distortions. These distortions require further adaptations to the pinhole model to account for the non-linear behaviour.

2.3.3 Epipolar geometry

An outcome of the pinhole camera model is the ability to mathematically describe the relationship between corresponding points in different images. The ability to mathematically describe the relationship between corresponding points, as a function of the camera properties, is known as epipolar geometry and forms the basis of many stages within the photogrammetry pipeline [50]. The properties of the fundamental matrix F for a pair of cameras is described by

$$\begin{bmatrix} u_2 & v_2 & 1 \end{bmatrix} F \begin{bmatrix} u_1 \\ v_1 \\ 1 \end{bmatrix} = 0 \tag{2.3}$$

where u_n and v_n are the image feature coordinates in camera n [50]. Physically, the fundamental matrix is a result of the each pixel corresponding to some three dimensional line projected back into space. The three dimensional projection in space can then be imaged by a second camera to give a two dimensional line, referred to as the epipolar line. The epipolar line l for the second camera in

equation 2.3 is given by

$$l = F \begin{bmatrix} u_1 \\ v_1 \\ 1 \end{bmatrix}. \tag{2.4}$$

The epipolar line l describes a line in the image space in which the point (u_1,v_1) must exist. A representation of the epipolar geometry is shown in figure 2.4, in which a point imaged by C_1 is projected into space and imaged by C_2 to give the epipolar line shown as a dashed line.

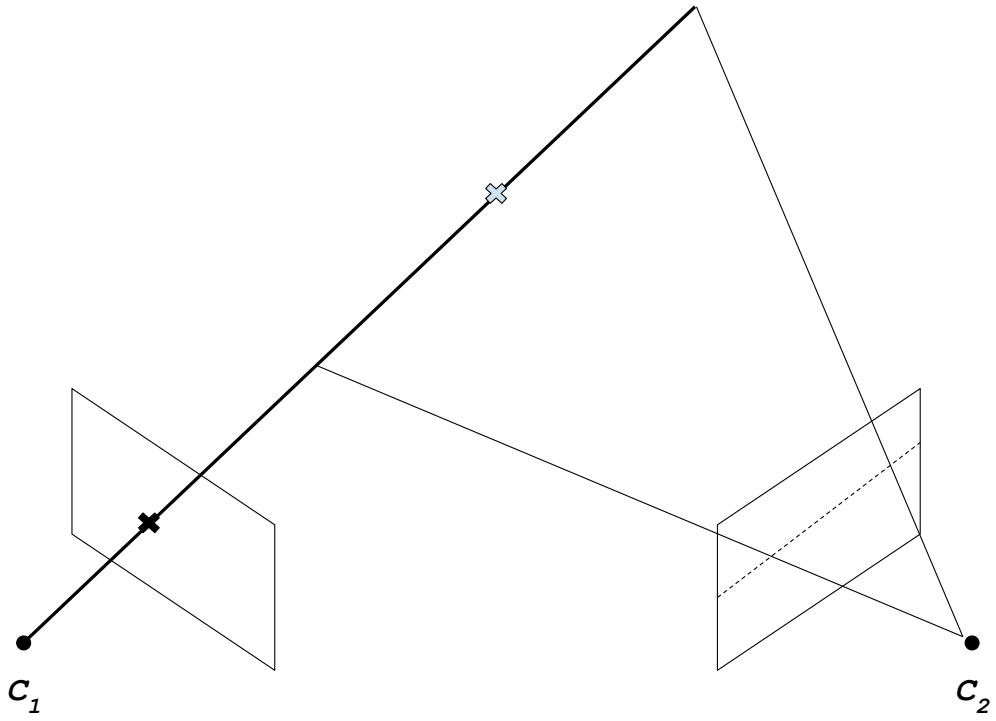

Fig. 2.4 Representation of epipolar geometry in which the epipolar line is represented by the dashed line.

The fundamental matrix can also be written in terms of the camera projection matrix described in equation 2.1 and is given by

$$F = [e']_X P_2 P_1^+ \tag{2.5}$$

where e' is the epipole of the second image given by

$$e' = P_2 C_1, \tag{2.6}$$

C_1 is the projection centre of the first camera, $[a]_X$ is the skew-symmetric matrix of $a = (a_1, a_2, a_3)^T$ given by

$$[a]_X = \begin{bmatrix} 0 & -a_3 & a_2 \\ a_3 & 0 & -a_1 \\ -a_2 & a_1 & 0 \end{bmatrix}, \tag{2.7}$$

and P_1^+ is the psuedo-inverse of the projection matrix of the first camera [50]. The structure of the fundamental matrix described in equation 2.5 forms the basis of several methods of characterising the camera properties and will be discussed in more detail in section 2.4.

2.3.4 Distortion modelling

Most recent advancements of the pinhole model include the lens distortions within the model parameters. Using extensive models that include these distortions is vital when attempting to achieve accurate characterisation of the camera system. Therefore, it is important to fully understand the sources and effects of these

distortions. In general, the distortions are parameterised through the additional terms δu and δv, as shown in figure 2.5.

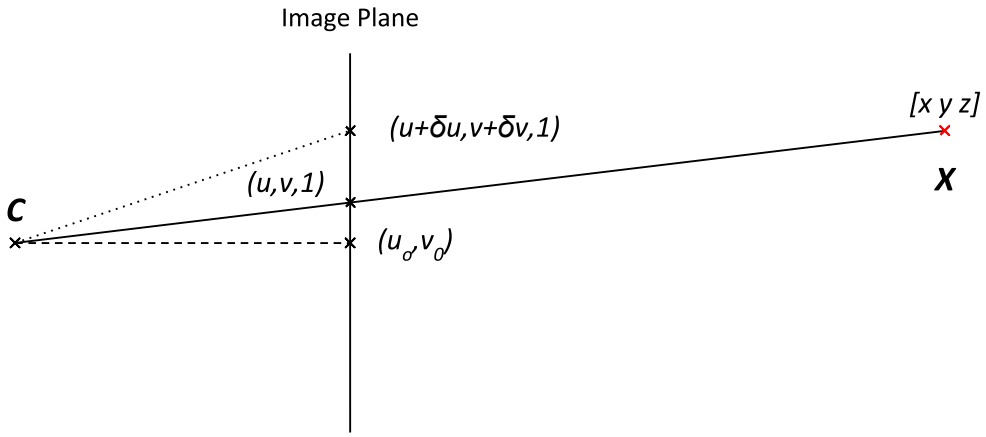

Fig. 2.5 Lens distortion effect on the image plane intersection point. The observed intersection is now at $[u + \delta u,\ v + \delta v]$.

There are three typical forms of distortion: radial, decentring and thin prism distortion. Radial distortion is simply a radially symmetric deformation about the principle point resulting in either a barrel or pin-cushion effect [38], as can be seen in figure 2.6. Decentring distortions are a result of the optical centre not being correctly aligned with the centre of the camera. This misalignment of the optical centre, results in both radial and tangential distortions that must also be included in the model. Thin prism distortion is a result of imperfections in the design and manufacturing of the camera lens and can be modelled as a thin prism being added to the optical system [95].

With all the potential sources of error, it is important to include enough parameters within the model such that it is flexible enough to fit the data. This concept is used in Percoco and Sánchez Salmerón in order to properly calibrate long focal length macro lenses [84]. With a long focal length lens, the distortions become significant and require consideration during both the calibration process and reconstruction. Through modelling up to sixth order radial and second order

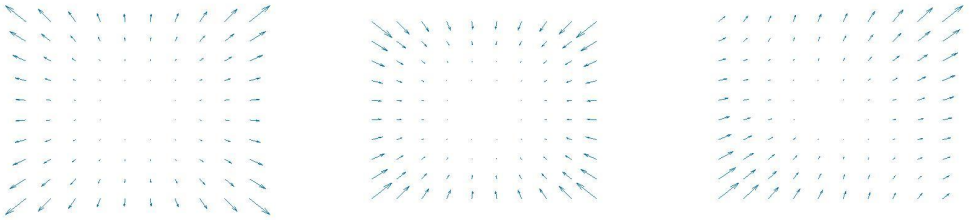

Fig. 2.6 Vectors corresponding to the relative movement of points in an image for barrel, pincushion and tangential distortions.

tangential distortion, Percoco and Sánchez Salmerón were able to digitise a tool part with an radial standard deviation of 8 μm over a 3.4° angle of view [86]. Despite earlier models predicting a minimum angle of view of 10°, correct modelling allows lower angles to be achieved, resulting in higher spatial resolutions [102].

2.3.5 Alternative camera models

Despite the wide application of the pinhole model, there are some cameras that require a significantly different approach. One such example is in the use of a telecentric lens (see [17], for example). Telecentric lenses only allow parallel light rays through the camera via the addition of an aperture stop between the lens and sensor array. A result of viewing only parallel rays is that there is no longer any perspective in the images; an object appears the same size regardless of its distance from the camera. Despite small fields of view, a constant magnification of objects regardless of their distance from the camera is produced. The effect of constant magnification on imaging the scene shown in figure 2.7 (a) can be seen in figure 2.7 (c), compared to a typical image shown in figure 2.7 (b).

The telecentric lens camera is best described by an orthogonal camera projection model. For the most part, the orthogonal projection model is the same as the pinhole camera and only replaces the intrinsic camera matrix with a new form

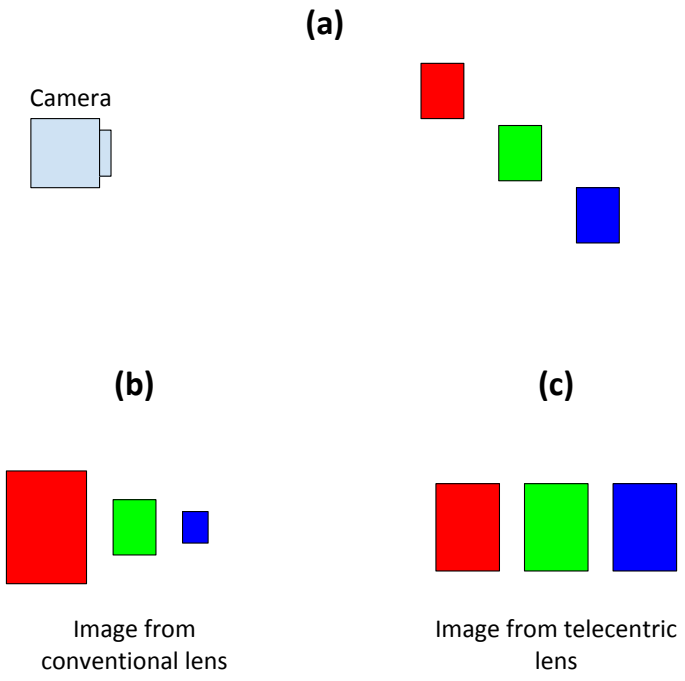

Fig. 2.7 Effect of imaging the scene shown in (a) with a telecentric lens. The image produced by a typical lens is shown in (b), whereas (c) shows the image that would be produced by a telecentric lens.

given by

$$K = \begin{bmatrix} k_u & 0 & 0 & 0 \\ 0 & K_v & 0 & 0 \\ 0 & 0 & 0 & 1 \end{bmatrix} \tag{2.8}$$

where the terms are the same as described in equation 2.2. Despite the orthogonal camera model requiring slightly different methods of calibration, overall the process is the same as the pinhole model. Through careful calibration of a pair of stereo telecentric cameras, Chen et al were able to measure the displacement of a calibration artefact with an average error of 2.9 μm [17]. Despite only measuring a simple displacement, this level of accuracy demonstrates the potential of telecentric cameras as a tool in photogrammetry.

Light-field cameras

There are a small number of other camera models available, but for the most part, they are just slight adaptations to either the pinhole or orthogonal models. There are, however, some completely different optical arrangements, such as the use of micro-lenses in light field cameras [129, 75]. Light field cameras are capable of measuring the colour, position and direction of incident light rays through the use of a micro-lens array. The main principle of imaging in light field cameras is shown in Figure 2.8. In a typical imaging system, the main lens would focus the light from an object directly on to the sensor. However, as can be seen in figure 2.8 (a), a light field camera instead focuses the light from the object onto an array of micro-lenses. The light from each micro-lens is then split into its angular components and is captured by the sensor, as can be seen in figure 2.8 (b). Effectively, each micro-lens within the micro-lens array becomes a single pixel, with each sensor pixel behind the micro-lens corresponding to a different ray direction.

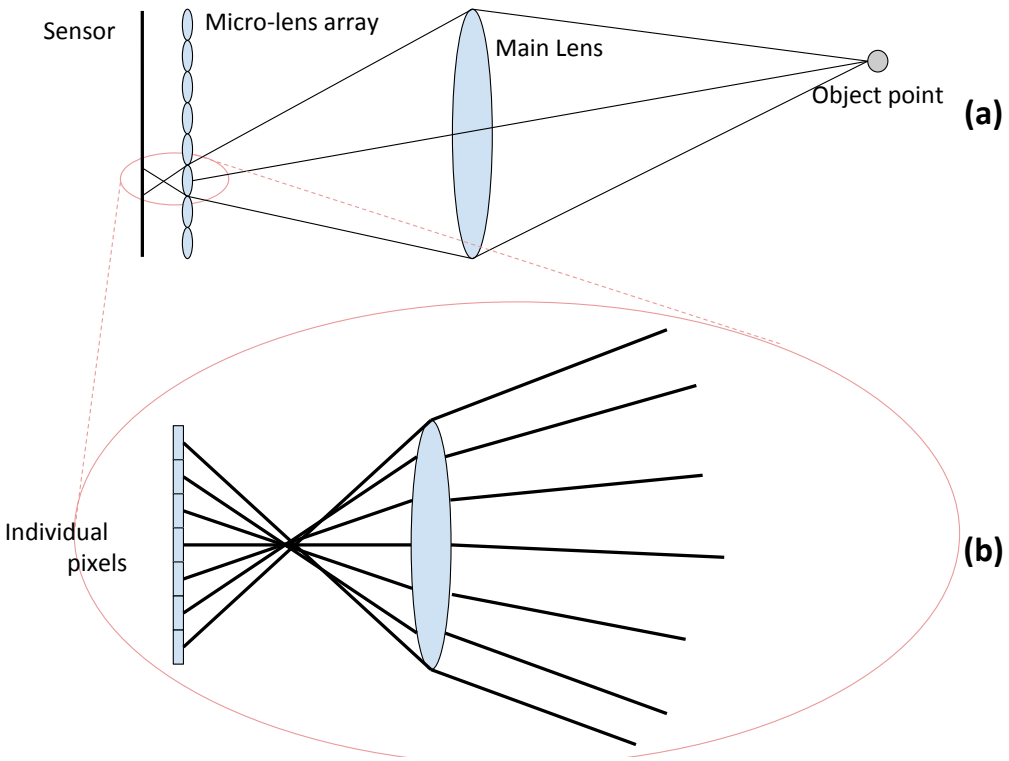

Fig. 2.8 The main imaging principle of light field cameras. A simplified version of the whole imaging system is shown by (a), where (b) shows a magnified view of a single micro-lens and sensor area.

The amount of information captured in a single light field camera image is significantly greater than that of a typical camera and, as a result, can be used to determine three-dimensional information from single images. A notable advantage of the use of light field cameras is that no focusing is required. As single images can be reconstructed from the light field data after it has been taken, this results in a significantly larger depth of field than is possible with generic cameras [120]. As more pixels are required to detect what is effectively a single point in the image, there will be a significant loss in resolution compared to typical cameras. As a result, light field cameras will produce a smaller image resolution for a given sensor size. Light field camera applications to photogrammetry are still relatively new, however, with this wide availability and research, light field cameras have the potential for significant improvement [127].

2.4 Calibration methods

Calibration is required in order to achieve accurate and reliable measurements. The same is true of cameras in photogrammetric systems, although camera calibration is somewhat different to conventional methods. Camera calibration aims to precisely determine the exterior orientation and intrinsic properties of the camera, effectively determining all the parameters described by the chosen camera model. Reconstructions are possible with un-calibrated cameras; however, no metric information can be obtained making such applications unsuitable in a metrological context. Fortunately, the camera models discussed in the previous section provide a method of determining camera properties. By taking images of an object with known dimensions, it is possible to deduce the camera properties by fitting the image and object coordinates to a camera model. This method forms the basis of camera calibration.

Camera calibration methods fall into three basic categories: linear, non-linear optimisation and two-step techniques. Non-linear techniques are capable of dealing with models that exhibit non-linear relationships, such as lens distortions. The iterative nature of non-linear techniques mean that they can be slow and are not always guaranteed to produce a correct result [70]. Non-linear techniques rely on the minimisation of some function; as a result an initial guess must be made that is reasonably close to the global minima. A significant deviation in initial parameters may result in a local minima being reached instead, producing an incorrect calibration [95].

Linear techniques are much faster due to their more simplistic approach [71]. Rather than making iterative calculations as in the non-linear approach; a single calculation can be made using linear behaviour. The linear method requires at least six corresponding points to work; however, by including many more points a least-squares regression can be used to refine the parameters [71]. Although this method benefits from its simplicity and speed, it is incapable of taking into account lens distortions. There may also be some issues when extracting the camera properties from the transformation matrix as the method is not able to account for lens distortion [95].

Finally, the two step technique is simply a combination of both the linear and non-linear techniques. A linear technique is first used to calculate some initial guess and fix some of the camera parameters [67]. With a good initial guess, the non-linear technique can be used in order to improve the chances of reaching a glabal minima. The two step technique is perhaps the most widely used technique as it increases speed through linear methods whilst still being able to account for image distortions [95].

2.4.1 Linear techniques

Linear techniques first require a definition for the transformation matrix that is being solved. Equation 2.1 can be re-written in the form

$$t\begin{bmatrix} u \\ v \\ 1 \end{bmatrix} = A\begin{bmatrix} x \\ y \\ z \\ 1 \end{bmatrix} = \begin{bmatrix} A_{11} & A_{12} & A_{13} & A_{14} \\ A_{21} & A_{22} & A_{23} & A_{24} \\ A_{31} & A_{32} & A_{33} & A_{34} \end{bmatrix}\begin{bmatrix} x \\ y \\ z \\ 1 \end{bmatrix} \tag{2.9}$$

where A is the projection matrix [71].

Equation 2.9 can then be used to solve for u_i and v_i to give the collinearity equations

$$u = \frac{A_{11}x + A_{12}y + A_{13}z + A_{14}}{A_{31}x + A_{32}y + A_{33}z + A_{34}} \tag{2.10}$$

$$v = \frac{A_{21}x + A_{22}y + A_{23}z + A_{24}}{A_{31}x + A_{32}y + A_{33}z + A_{34}} \tag{2.11}$$

where the t term from equation 2.9 is cancelled, leaving only camera properties and the three-dimensional coordinate of the point being imaged [71]. The collinearity equations can then be used to define a linear relationship between the image and world coordinates and the vector matrix A' given by

$$QA' = 0 \tag{2.12}$$

where

$$Q = \begin{bmatrix} x_1 & 0 & \dots & \dots & x_n & 0 \\ y_1 & 0 & \dots & \dots & y_n & 0 \\ z_1 & 0 & \dots & \dots & z_n & 0 \\ 1 & 0 & \dots & \dots & 1 & 0 \\ 0 & x_1 & \dots & \dots & 0 & x_n \\ 0 & y_1 & \dots & \dots & 0 & y_n \\ 0 & z_1 & \dots & \dots & 0 & z_n \\ 0 & 1 & \dots & \dots & 0 & 1 \\ -u_1x_1 & -v_1x_1 & \dots & \dots & -u_nx_n & -v_nx_n \\ -u_1y_1 & -v_1y_1 & \dots & \dots & -u_ny_n & -v_ny_n \\ -u_1z_1 & -v_1z_1 & \dots & \dots & -u_nz_n & -v_nz_n \\ u_1 & v_1 & \dots & \dots & u_n & v_n \end{bmatrix}^T, \tag{2.13}$$

$$A = \begin{bmatrix} A_{11} \\ A_{12} \\ A_{13} \\ A_{14} \\ A_{21} \\ A_{22} \\ A_{23} \\ A_{24} \\ A_{31} \\ A_{32} \\ A_{33} \\ A_{34} \end{bmatrix}, \tag{2.14}$$

and n is the number of points [95].

There are twelve unknown parameters in equation 2.12; as a result, a minimum of six corresponding points are required ($n \geq 6$). When n is higher than six, using the linear relation given in equation 2.12 it is possible to solve for A' using a least-squares regression method. The least-squares regression aims to minimise the function $\left\|QA'\right\|^2$ with the constraint that $\left\|A'\right\| = 1$. Through solving the minimisation of $\left\|QA'\right\|^2$, the solution of A' is found to be the eigenvector of Q^TQ corresponding to the smallest eigenvalue [131].

Solving the eigenvector of Q^TQ to calculate A' provides a fast and simple method of camera calibration [67]. As discussed earlier, linear calibration methods are unable to account for distortions within images making them unsuitable for accurate calibrations. However, linear methods do offer a method for initial parameter estimation. The eigenvector method of parameter initialisation is used by Gu et al in order to calculate initial extrinsic and focal length estimations [47]. In order to make the linear method applicable, two assumptions are made: all coefficients of lens distortion are zero and the principle point is located at the exact centre of the image. Based on the assumption of zero lens distortion and principle point in the centre of the image, the extrinsic and focal length parameters can be extracted from A', and calculated using the eigenvector method described above [130]. With the initial parameters calculated, the values can be further refined using a non-linear minimisation technique.

2.4.2 Non-linear methods

As linear techniques are incapable of modelling image distortions; other, more complex, approaches must be considered. The methods of calibrating camera models that take into account the complex distortions that occur in many cameras are in general non-linear techniques.

For radial distortion, δu and δv are given by

$$\delta u = u(1 + k_1 r^2 + k_2 r^4 + k_3 r^6) \tag{2.15}$$

$$\delta v = v(1 + k_1 r^2 + k_2 r^4 + k_3 r^6) \tag{2.16}$$

where $r = \sqrt{x^2 + y^2}$ is the radial distance and k_1, k_2 and k_3 are the radial distortion coefficients. The effect of the various radial distortion coefficients is shown in figure 2.9, where k_1, k_2 and k_3 correspond to the second, fourth and sixth order contributions to the distortion.

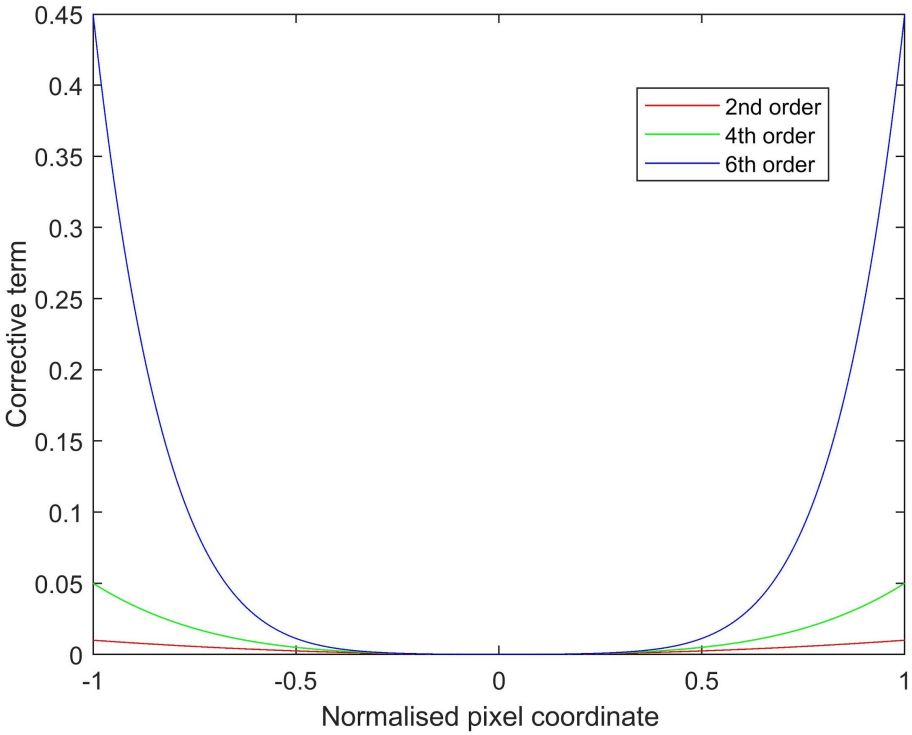

Fig. 2.9 Representation of the effect of radial distortion of varying order. The legend refers to the maximum order of distortion that is taken into account.

Typically equations 2.15 and 2.16 are estimated up to the second or third term in order to have sufficient parameters (see [17] and [87] for examples). Equations 2.15 and 2.16 can then be combined with equations 2.10 and 2.11 respectively to

produce the distorted collinearity equations. With radial distortion now included, the camera model exhibits non-linear behaviour due to the addition of the radial distance term, r.

Non-linear techniques are centred on the minimisation of some function $f(\tilde{x}, m_i, M_i)$, where m_i is the image coordinates of point i, M_i the physical coordinates and $\tilde{x}$ is a vector containing all the chosen camera properties. Mathematically, this minimisation is expressed as

$$\sum_{i=1}^{N} \left\| f(\tilde{x}, m_i, M_i) \right\|^2 \tag{2.17}$$

where $f(\tilde{x}, m_i, M_i) = m_i - \bar{m}(\tilde{x}, M_i)$ and $\bar{m}$ is the projection of the three-dimensional coordinates M_i onto 2D image coordinates based on the camera properties $\tilde{x}$ [131]. The minimisation problem shown in equation 2.17 can be solved via already established algorithms, such as the Levenberg-Marquardt (LM) algorithm [77]. There are other algorithms capable of solving the minimisation problem shown in equation 2.17; however, the LM algorithm is the most suitable and widely used [99]. The LM algorithm is an iterative process by which the variable vector is iteratively updated in the direction that minimises the cost function. For the case of camera calibration, the variable to be changed is the camera properties vector $\tilde{x}$. For iteration, n, the next value of $\tilde{x}$ is given by $\tilde{x}_{n+1} = \tilde{x}_n + \Delta\tilde{x}$, where $\Delta\tilde{x}$ is calculated as

$$\Delta\tilde{x} = (J^T J + \lambda I)^{-1} J^T f(\tilde{x}_n) \tag{2.18}$$

where J is the Jacobian and λ is the damping factor [112]. The damping factor, λ, shifts the minimisation between a gradient decent and a Gauss-Newton method of minimisation. Reducing the damping factor makes the minimisation algorithm behave like the Gauss-Newton algorithm, suitable for when the reduction in the

minimisation function is fast. However, the damping factor can be increased when the reduction in the residual slows down, resulting in an algorithm that behaves similarly to a gradient decent method. The variation in the damping factor ensures the LM algorithm approaches the global minima rather than becoming trapped in local minima. The Jacobian matrix is given by

$$J = \begin{bmatrix} \frac{\delta f_1}{\delta \tilde{x}_1} & \frac{\delta f_1}{\delta \tilde{x}_2} & \cdots & \frac{\delta f_1}{\delta \tilde{x}_m} \\ \frac{\delta f_2}{\delta \tilde{x}_1} & \frac{\delta f_2}{\delta \tilde{x}_2} & \cdots & \frac{\delta f_2}{\delta \tilde{x}_m} \\ \vdots & \vdots & \ddots & \vdots \\ \frac{\delta f_k}{\delta \tilde{x}_1} & \frac{\delta f_k}{\delta \tilde{x}_2} & \cdots & \frac{\delta f_k}{\delta \tilde{x}_m} \end{bmatrix} \tag{2.19}$$

where $\tilde{x}_m$ represents one of m camera properties and f_k is one of k functions.

Many current areas of research in micro-scale photogrammetry are focused on altering the LM algorithm to produce a more accurate calibration. Gu et al provides an ideal example of such an adaptation of the LM algorithm through use of back projection [47]. Equation 2.17 is essentially the sum of the residual vectors produced from the difference between the expected and observed image coordinates for given camera parameters. The method described by Gu et al instead calculates the residual as the difference between known three-dimensional coordinates and the observed image coordinates projected back into three-dimensional space. Conventional calibration algorithms typically attempt to minimise the difference between the detected image point and the expected image point given by the projection model. However, by instead assuming that the three-dimensional point lies on a plane, the intersection between the observed image point vector and the plane can be calculated. The difference between the known point on the plane and the observed image point vector intersection can then be minimised instead. Through the use of the back projection calibration method, Gu et al was able to increase accuracies by

2 μm to 6 μm compared to the typical forward imaging process, achieving errors of 42 μm and 41 μm in the x and y directions respectively [47].

The nature of the LM algorithms allows it to be applied to any camera model, including the orthogonal projection model. Chen et al use the LM algorithm in order to calibrate a telecentric lens based camera through the use of a 2D checkerboard artefact. The checkerboard artefact provides the known world points required for calibration, and by measuring a known depth change of the artefact, the depth uncertainty was also determined. Through the use of the LM algorithm on the telecentric lens camera, a depth uncertainty of 2.9 μm was attained with a lateral resolution of 11 μm [17].

Algorithm efficiency also becomes an important factor when considering iterative methods. The Jacobian matrix is particularly time consuming to calculate, reducing the computational cost would, therefore, be beneficial. Vaudrey and Klette outline a method that separates the intrinsic and extrinsic camera parameters and solves them individually [112]. By splitting up the intrinsic and extrinsic parameters, the new form of the Jacobian exhibits significant sparsity. The sparsity of the Jacobian is a result of the majority of non-zero components lying on the diagonal. The sparsity of the new matrix allows it to be calculated more efficiently, particularly when calculating the inverse of $(J^T J + \lambda I)$ as required in equation 2.18 [112].

2.4.3 Self-calibration

In some circumstances it is difficult or impossible to know the geometry of a scene within a set of images. In the case of unknown scene geometry, the methods described in section 2.4.2 are no longer applicable. The term M_i now becomes an unknown parameter and to minimise the function given by equation 2.17 no longer

applies. Rather than considering M_i as missing information, self-calibration treats it as another variable to be refined when minimising equation 2.17. Through the comparison of multiple images from cameras at different positions, it is possible to simultaneously alter both the camera parameters, $\tilde{x}$, and corresponding point coordinates, M_i. The self-calibration minimisation problem requires a slight adaptation to equation 2.17 to give

$$minimise_{\tilde{x}} \sum_{i=1}^{N} \sum_{j=1}^{M} \left\| m_{i,j} - \bar{m}(\tilde{x}_i, M_j) \right\|^2 \tag{2.20}$$

where $m_{i,j}$ is the image coordinate of point i produced by camera j [130]. The minimisation problem described in equation 2.20 is solved in exactly the same way as described in section 2.4.2 and effectively calibrates the camera and reconstructs the three-dimensional scene at the same time.

With three or more views of eight or more points, the solution to equation 2.20 will produce a unique solution [50]; however, this solution will be a projective reconstruction and not a true metric reconstruction. Fortunately, camera projection theory allows a metric reconstruction to be calculated from the projective reconstruction through the use of the rectifying homography matrix, H. The rectifying homography can be calculated through the decomposition of the absolute dual quadric, Q_∞^*, which is defined as a conic on the plane at infinity. The absolute dual quadric can be calculated using the dual image of the absolute conic which is given by

$$\omega^* = PQ_\infty^* P^T \tag{2.21}$$

where P is the camera matrix for a projective reconstruction as described in section 2.3 [50]. As the name suggests, the dual image of the absolute conic is simply the image projection of the absolute dual quadric. Figure 2.10 shows both the

absolute dual quadric and dual image of the absolute conics for a stereo camera configuration.

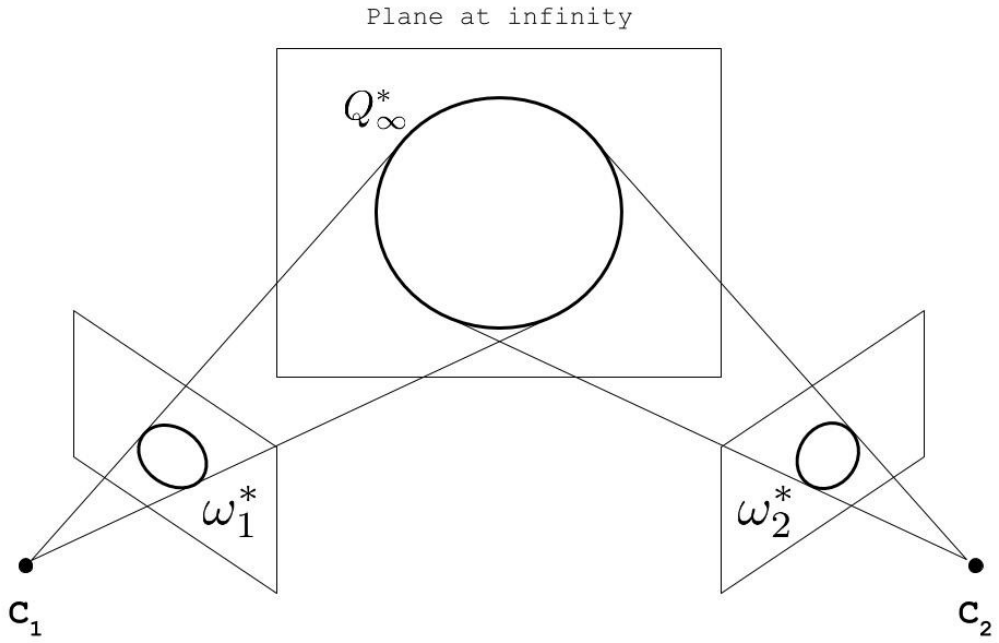

Fig. 2.10 Diagram for the absolute dual quadric and dual image of the absolute conic in a stereo-camera configuration.

The issue with self-calibration arises when estimating the dual image of the absolute conic. In order to make some estimates about ω^*, it must be calculated from the equation

$$\omega^* = KK^T \tag{2.22}$$

where K is the camera intrinsic property matrix described in equation 2.2. As the whole point of calibration is to determine K, estimating ω^* first requires some assumptions to be made about the camera's intrinsic properties. The intrinsic parameters of the camera are not completely unknown, they will be within some reasonable range values. By using some assumptions about the intrinsic camera

parameters, such as zero skew, a principle point at the centre of the image and an initial guess for the focal length, ω^* can be estimated up to some factor to a sufficient level of accuracy [50]. However, as the calculation of the rectifying homography is based on estimates, it will not be completely accurate. Fortunately, the estimate for the rectifying homography simply provides an initial guess and the values can be further refined via a non-linear minimisation process similar to that used in section 2.4.2.

As would be expected, micro-scale photogrammetry requires micro-scale calibration artefacts. This requirement of micro-scale calibration artefacts is what makes self-calibration so useful in photogrammetry at such small scales. This is the method used by Galantucci et al in order to design a scanning methodology and physical apparatus capable of digitising objects with sub-millimetre features [36]. The apparatus used by Galantucci et al consists of a rotating stage with a digital SLR camera (10 megapixel sensor, 50 mm lens focused to infinity with a 36 mm extension tube) at a fixed position. The rotating stage of the scanner has 12 bit coded targets on its surface that can be detected in each image and easily matched. By taking a series of images as the stage rotates, Galantucci et al were able to determine the camera properties through self-calibration methods. The calibrated apparatus was then used to scan a complex part with a pyramidal geometry exhibiting various features. The level of accuracy achieved by Galantucci et al varied slightly over the twenty-four measurements, but in general achieved high accuracy. Overall, Galantucci et al obtained standard deviations in depth measurements of 44 μm at most.

In this work, the measurement uncertainties of two photogrammetry systems are evaluated by computationally evaluating the measurement uncertainty and then verifying the results through acceptance tests. The key background for this work

will be the consideration of the influence factors to the measurements uncertainty and the current standards for the verification of photogrammetry. In section 2.5, the potential influence factors will be discussed after which the current standards in uncertainty analysis will be presented in section 2.6. The current standards available for the verification of photogrammetry systems will also be outlined in section 2.7.

2.5 Fundamental limitations of photogrammetry accuracy

No optical method directly measures the physical coordinates of a point on an object. The measurement is made using the information captured by the optical system, after which calculation of the object geometry is made. Therefore, the fundamental limitations to the potential geometric accuracy of photogrammetry can be divided into two key factors; pixel uncertainty and triangulation uncertainty. The pixel uncertainty corresponds to the accuracy to which image features can be localised within the image and is a result of the properties of the optical system and the nature of the image feature that is used. The triangulation uncertainty, on the other hand, describes the accuracy to which the corresponding image features can be triangulated in space and is a result of the uncertainties of the characterised system parameters. The two factors are heavily linked, with the pixel uncertainty heavily influencing the uncertainty of the parameter characterisation and the combination of the two factors determining the overall measurement uncertainty. In sections 2.5.1 and 2.5.2, the sources of uncertainty will be described. However, the effects of triangulation uncertainty will be further addressed in section 2.6 as well as being the main focus of chapter 3.

2.5.1 Pixel uncertainty

In this section, the contributing factors to the localisation of a image feature is discussed. The uncertainty on the localisation of an image feature is highly complex and is the result of a multitude of factors. Although this discussion is not exhaustive, the main influence factors identified in the literature review will be addressed.

Optical resolution

Optical resolution determines the ability of an imaging system to resolve an object being imaged [94]. Many factors affect the optical resolution, however, for a perfect imaging system the resolution limit will be determined by either the diffraction limit, or pixel size. In principle, the optical resolution will either be limited by the size of the sensor pixels or the diffraction limit of the optical system, depending which is larger. This section will address the contribution of the diffraction limit on the optical resolution. Figure 2.11 shows the imaging principle of a point source produced by a simple lens and aperture system, the image produced is the point spread function (PSF) [94].

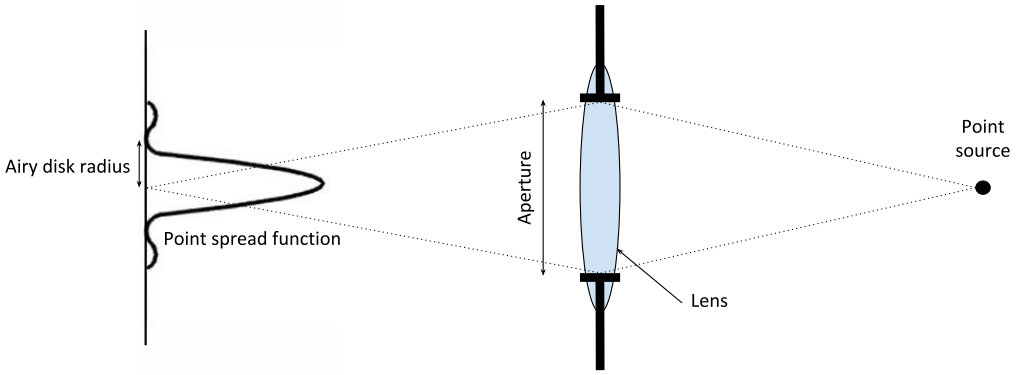

Fig. 2.11 Image produced by a point source passing through a simple optical system consisting of a lens and circular aperture. The image produced is the point spread function.

The radius of the central region of the PSF, corresponding to the distance between the peak and the first minima and known as the Airy disk, determines the maximum resolution of the imaging system with a circular aperture [12]. The Airy disk radius is a function of both the lens focal length and objective aperture diameter. The Rayleigh criterion is defined as the minimum distance between two PSFs for which both can still be resolved and is given by

$$r = 1.22\lambda N \tag{2.23}$$

where λ is the light wavelength and N is the f-number of the lens [20]. The f-number (usually shown as f/N, where N is the f-number) is simply the ratio of the focal length to the objective aperture diameter [12]. In order to minimise r and improve resolution, the f-number, N, must be minimised. Typical lens arrangements used in micro-scale photogrammetry applications have an f-number of around one to three. For visible light ($\lambda \approx 500$ nm), a minimum resolvable distance of 610 nm could be obtained with a $f/1$ lens arrangement. In practice, it is not possible to just make the f-number as small as possible. Decreasing the f-number will also lead to a loss in depth of field and image brightness; depth of field being the most problematic at the high-magnifications required for micro-scale measurements. The depth of field simply describes the range over which an object will appear in focus and will be discussed in section 2.5.1.

It is not as simple as defining some cut off distance for when two points are indistinguishable. There is instead a loss of contrast between points over all scales, just by differing amounts. This loss of contrast is best described by the modulation transfer function (MTF). The MTF describes how an optical system will affect the contrast of spatial frequencies of an image [56]. Effectively the MTF acts as a filter on the 2D Fourier transform of an image to alter the contrast of spatial

frequencies. The MTF ranges from zero to one corresponding to 0 % to 100 % contrast respectively. The basic form of the MTF can be seen in figure 2.12 where the Rayleigh criterion corresponds to the value of 0.264.

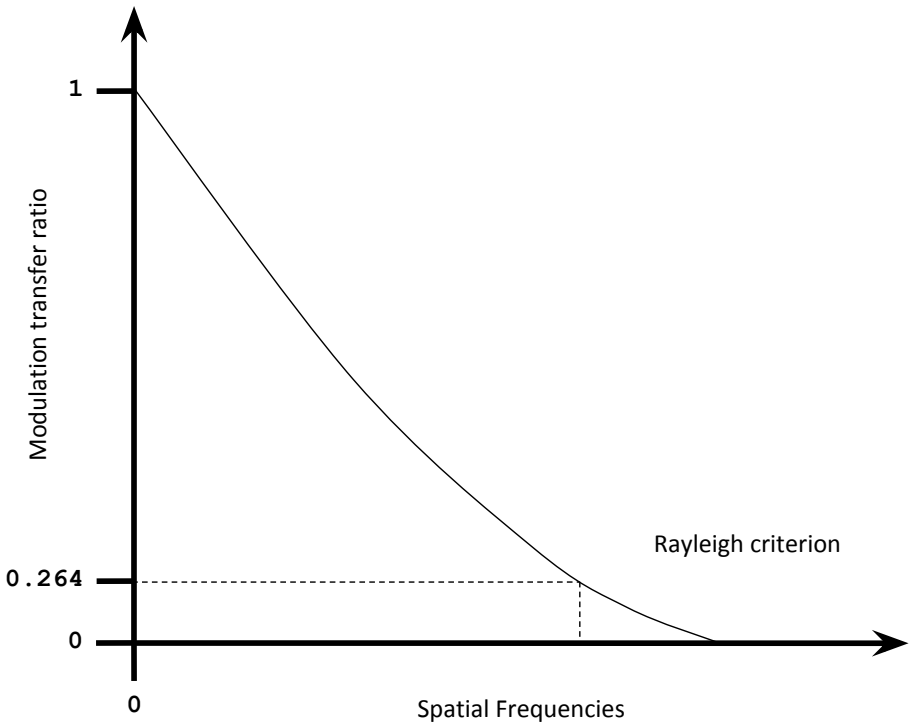

Fig. 2.12 Basic form of the modulation transfer function. The MTF value of 0.264 corresponds to the Rayleigh criterion.

Although the MTF gives a more complete description of the response of an optical system, there is still little work as to how this would translate to photogrammetry. Further research is required on determining how the MTF of multiple images can be used to determine some MTF for the three-dimensional reconstruction. The problem of determining the MTF of reconstruction is complex and requires significant work, for now calculations based on the Rayleigh criterion will be used.

Sampling

Although diffraction limits give an indication of the best possible resolution, in practice this is not the case. As digital cameras take images as discrete samples, there will be an effect of discrete sampling on the PSF. The effect of sampling is best described through the change in contrast of an image. The contrast of two PSFs is the difference between the minimum and maximum values of intensity across the object, for two perfectly resolved points this would be 100 %. The concept of contrast can also be applied to the Rayleigh criterion; two PSFs separated by the radius of the Airy disk will have a contrast of 26.4 % [104]. The effect of sampling is to essentially average over an area, a consequence of which is to average out local maxima and minima. The reduced contrast and pixellation of the object also has the effect of making the exact position of the maxima ambiguous. As photogrammetry relies on precise determination of a point within an image, the ambiguity of maxima points can mean the pixel size is the limiting factor rather than diffraction. Given an average wavelength of 610 nm and a typical sensor pixel size of around 1 μm to 10 μm [108], the f-number of the imaging system can be chosen in order to ensure that the pixel size is the dominant factor in the imaging resolution.

Noise

As with sampling, the addition of noise into an image further reduces the contrast. The effect of adding 5 %, 10 % and 30 % of noise to a PSF is shown in figure 2.13.

As figure 2.13 illustrates, noise can substantially reduce contrast of a PSF as well as shift the apparent position of the maxima point. As a result of the loss of contrast and maxima shift, noise must be carefully considered during calibration and reconstructions in stereo camera systems. In order to deal with

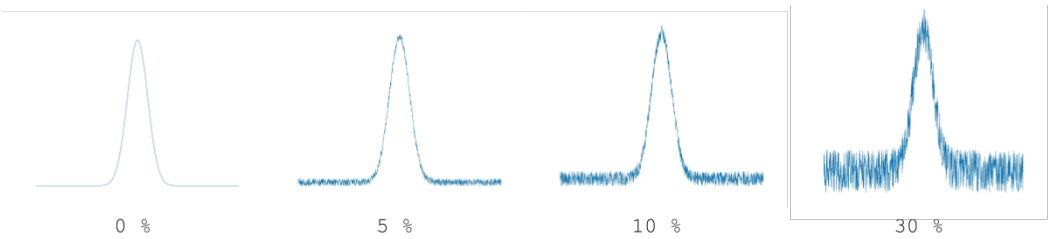

Fig. 2.13 Effect of noise on a PSF. A noise level of 0 %, 5 %, 10 % and 30 % are shown.

noise effectively, mathematical models and sources must first be identified. One of the most prominent sources of noise is from the camera itself [13]. Noise produced by the electrical amplifiers and detectors, thermal vibrations and thermal emissions from within a camera all contribute to the noise present within an image. These natural sources of noise can generally be modelled by a Gaussian distribution given by

$$P(g) = \sqrt{\frac{1}{2\pi\sigma^2}} e^{-\frac{(g-\mu)^2}{2\sigma^2}} \tag{2.24}$$

where g is the grey level value, σ is the standard deviation of the distribution and μ is the peak position of the distribution. Salt and pepper noise can also arise due to effects within the camera [13]. Salt and pepper noise arises due to corruption of the image data; as a result, certain pixels within the image will be randomly changed. For 8-bit images, the colour levels will range from 0 to 255 in integer steps, for grey-scale this corresponds to black to white respectively. Salt and pepper noise presents itself as a replacement of a dark pixel with 255 or a light pixel with 0, resulting in a salt and pepper appearance [13]. Interference within the electrical components of a camera can also result in structured noise being present in an image. Structured noise appears as periodic or aperiodic variations over the image of varying phase, frequency and amplitude.

Noise can be substantially reduced through choice of equipment, lighting and camera settings. By having sufficient light, low ISO sensitivity settings [66], repeat exposures and appropriate lenses, the noise present in an image can be reduced to appropriate levels. In order to further reduce the noise, image processing techniques can be applied to improve the contrast of any features within the images. Image filtering is a widely used method of noise reduction and can be used in a variety of ways to produce the desired effect [83, 132]. Low pass, smoothing filters can be used to suppress noise and other unwanted effects; whilst high pass, sharpening filters can enhance the contrast of particular features [74]. Band filters can also be used to remove periodic noise by rejecting the correct spatial frequencies [13]. Although filtering methods are useful at noise removal, there are some downsides. Filtering effectively smooths out any noise, in doing so there will be a loss of sharpness in some features. Conversely, sharpening filters will also enhance any noise present in the image leading to even greater noise levels.

The models, algorithms and equipment discussed in this work utilise only simple filters for noise reduction [40]. There is work covering the effects of noise in the calibration process, relating the error in pixel position to the resultant errors in intrinsic camera parameters (see [131, 47, 130]). The level of pixel coordinate noise typically considered is around 0.1 to 1.5 pixels, and work suggests that non-linear optimisation algorithms can cope with such errors and still produce accurate calibration [70]. The relative contributions of the various influence factors will be considered in more detail in chapter 3. However, with a decrease in scale, there will be an unavoidable increase in relative noise; which, as of yet, micro-scale photogrammetry does not sufficiently address. Therefore, for micro-scale photogrammetry to be applied to even smaller scales than are currently used, much more robust methods of calibration and reconstruction will have to be developed.

Feature matching algorithms

No matter how well the camera images the object, unless features can be detected and matched between images, the lower limits of reconstruction error cannot be obtained. As a result, great care must be taken to ensure feature matching between images is carried out correctly and accurately. A popular method of feature matching is the use of Scale Invariant Feature Transform (SIFT) algorithms [40, 36, 14]. SIFT algorithms work by assigning a 128 variable descriptor vector to each feature in an image which can then be used to match each feature in multiple images [65]. The descriptor vector is calculated as a function of the gradient magnitude and angle for neighbouring pixels. The nature of the descriptor vector means that it is largely invariant to both rotation and scale transforms, ideal for matching features under different image projections. Normalisation of the descriptor vector also provides some invariance to illumination changes, however, for the most part, illumination is easily controlled in a laboratory setting.

SIFT algorithms also allow for targets to be searched for, within an image. By placing coded targets within the space to be sampled, each individual target can be detected and matched without comparing between images. The main benefit of using coded targets is the significantly reduced possibility of false-positive matches, leading to improved reconstruction and calibrations. For the most part, coded targets are used in the calibration process [36]. Another benefit of determining the structure of the target is that it allows for an even more accurate determination of its centre. By having some central region of the target with a basic known geometry, a sub-pixel accuracy of the centre can be extrapolated. Xiao et al was able to detect coded targets on a calibration artefact to an accuracy of around 0.05 pixels through the sub-pixel detection of the target centre [121]. This method of using known target geometry can also be extended to more than just coded targets. The use

of a checkerboard as a calibration artefact is also a widely used technique. The geometry of the checkerboard ensures that it is easily automatically detected by algorithms. Again the geometry of a checkerboard allows a sub-pixel accuracy detection of the corners, as is used by Fathi and Brilakis [31].

An issue with feature matching is that with some objects and surfaces there will not be any features to detect. Surfaces that are particularly smooth or do not exhibit any distinct changes in colour will not show up during a feature detection algorithm. Without any points to triangulate, there may be significant areas of missing data. A simple way of solving this issue is to force some form of texture onto the surface. Koutsoudis et al create features on a smooth surface by projecting a series of noise patterns on a complex object [57]. By projecting a noise pattern, Koutsoudis et al was able to significantly increase the number of cloud points whilst reducing the reconstruction error from 108 μm to 43 μm compared to the original reconstruction. In chapter 4, an additional method of solving the correspondence issue is presented using laser speckle texture projection.

Model limits

The mathematical models used to describe the camera projections are far from the limiting factor in photogrammetry. With a sufficient number of parameters, the pinhole and orthogonal projection models are more than adequate to describe a wide variety of cameras. This use of long focal lengths results in a very narrow field of view, and projected rays become close to parallel. When small fields of view are used, significant errors will be produced when the pinhole model is applied, particularly when the field of view drops below 10° [86, 102]. The issue with the pinhole model arises due to the projected rays becoming almost parallel; as a result, the pinhole model will no longer be valid.

Stamatopoulos and Fraser suggested that, through the use of both the pinhole and orthogonal projection models, accurate reconstructions could be achieved [102]. Through a use of both models, Stamatopoulos and Fraser were able able to achieve a calibration where other pinhole methods failed due to instabilities in the calibration algorithm. Lateral errors of 1.3 µm and depth errors of 0.8 µm were recorded by Stamatopoulos and Fraser on a scan of a coin. Based on the equipment used by Stamatopoulos and Fraser, the camera would have a magnification of one, pixel size of 6.1 µm and a diffraction limit of 1.7 μm. Considering the equipment specification, Stamatopoulos and Fraser should acheive a theoretical maximum standard deviation of around 6.1 µm due to the pixel size. The discrepancy between theoretical maximums and actual recorded error by Stamatopoulos and Fraser does cast some doubt on the validatity of their results. However, the concept of a hybrid model approach to calibration and reconstruction could still be valid.

Percoco and Sánchez Salmerón experimentally tested the effect of angle of view on the pinhole camera model on camera calibration and object reconstruction [86]. Percoco and Sánchez Salmerón found that the pinhole camera was successful with angles of view as low as 3.4° and could produce accuracies comparable to other scanning methods. The level of error produced by Percoco and Sánchez Salmerón is also consistent with expected accuracies. Verification of the pinhole models to small angles of view suggests that it is possible to produce a photogrammetry system with magnifications of around two. Coupled with small pixel sizes and f-numbers, a magnification of two could achieve accuracies of around a micrometre in the right circumstances.

Depth-of-field

In theory there will only be a single plane that will be in focus when taking an image. In practice there will, in fact, be a range of points that appear to be in focus. The range over which points appear to be in focus is the depth-of-field, and is a result of being unable to notice the blurring effect of a point being out of focus [86]. The ability of a system to detect whether or not a point is in focus is determined by the circle of confusion, defined as the diameter of the largest blurred spot that appears as a point to the human eye. For 35 mm aperture, the circle of confusion is conventionally set to 0.03 mm, differences in viewing conditions and individual differences can, however, lead to small changes to this value [86]. The principle of the depth of field is shown in figure 2.14.

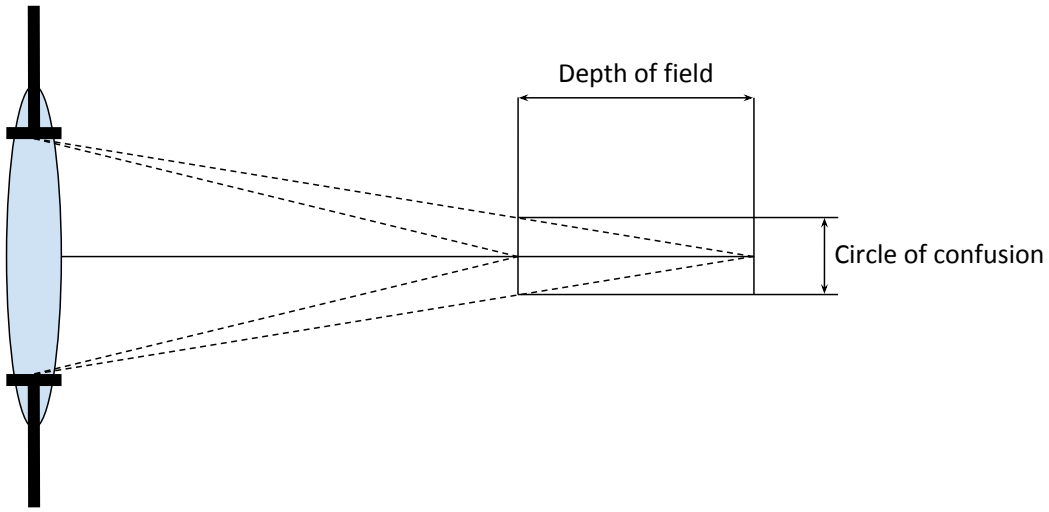

Fig. 2.14 Principle of depth of field for a lens and aperture. The dashed lines correspond to the light rays from the closest and furthest points in focus.

As figure 2.14 suggests, the circle of confusion fixes the minimum and maximum distances for which a point will be in focus for a particular f-number. By changing the f-number, and hence the aperture size, the ray lines in figure 2.14 will either be squeezed inwards or spread out. As the circle of confusion is a constant value,

reducing the angle of the light rays will increase the depth of field and decrease it for increased angle. This effect is highlighted by the equation for depth of field given by

$$d = 2NC(1 + \frac{1}{M}) \tag{2.25}$$

where N is the numerical aperture, C is the diameter of the circle of confusion and M is the magnification.

As discussed in section 4.1, in order to ensure diffraction effects do not limit the imaging system, a very low f-number must be chosen. Choosing such a low f-number directly leads to a decreased depth of field, meaning a reduced working range. This trade-off between resolution and depth of field is purely a result of optical effects and, therefore, is very difficult to overcome. For many applications, simply choosing the optimal f-number for the sample dimensions would be adequate. However, in order for photogrammetry to be useful from a micro-manufacturing stand-point, this trade-off between resolution and depth of field must be overcome.

Gallo et al provide a method of overcoming the small depths of field produced by macro lenses through the use of image stacking. By taking many images at varying focus distances, a stack of images can be produced for which each pixel is in focus in at least one image [40]. A fusion algorithm can then be applied to the stack of images in order to produce a singular image for which all points are in focus. Gallo et al was able to measure step heights of 20 μm to 100 μm to an uncertainty of 10 μm with the multi-focus image stacking method at a magnification of one [40]. Compared to Percoco and Sánchez Salmerón, Gallo et al were able to achieve similar accuracies at half the magnification and with a significantly larger sampling area. The downside to the image stacking method is the significant image acquisition times; complex objects took around two hours to image due to the

methodology used. Future work was suggested to improve the automation of the process and, therefore, bring imaging times down to suitable durations.

Another less obvious method of overcoming depth of field constraints is to alter the optics and remove the issue entirely. Plenoptic cameras (light field cameras) use an entirely different method of image acquisition for which depth of field and focus are no longer limiting factors [127]. By placing an array of micro-lenses between the imaging sensor and optical components the entirety of the light field can be detected, not just intensity and position. Plenoptic cameras are able to detect the position, incoming angle, intensity and colour of incoming light rays allowing for image reconstruction after acquisition. Current use of plenoptic cameras for depth mapping is limited to single camera methods using only the light field data [120, 127]. The level of accuracy achieved by plenoptic cameras is still relatively low; however, their current resolution is significantly lower than is typical for regular DSLR cameras. Higher resolution cameras are beginning to become widely available, but are yet to be tested in micro-scale photogrammetry applications.

2.5.2 Triangulation uncertainty

Projection errors

Photogrammetry requires more than one image to determine three-dimensional coordinates, reconstruction errors will, therefore, be dependent on the errors provided from multiple images. In principle, the reconstruction process involves calculating the intersection of two or more vectors. The vectors are a result of projecting out individual pixel positions, hence pixel position uncertainty results in vector uncertainty. The pinhole camera model also leads to a divergence of projected rays as they get further from the camera. A result of the ray divergence

is that projected vectors will also experience increased error as their magnitude increases.

This divergence of rays is best visualised through its more notable effect, magnification. An object of size X will appear in an image the size $x = X/m$, where m is the image scale number [71]. The translation of image error to object error is identical to that for image height, simple magnification by multiplication. For a known focal length, object distance and feature location error, the lateral triangulation error can be calculated using the thin lens equation to give

$$\Delta X = m\Delta x = (c/f - 1)^{-1}\Delta x \tag{2.26}$$

where f is the focal length, $c = (1/f - 1/h)^{-1}$ is the principle distance and h is the distance to the object. Image scale numbers achieved in recent papers using macro lenses range between 0.5 and 5 with lower values being most favourable [40, 84, 86]. Assuming the imaging system is not diffraction limited, image point accuracies would be around a pixel in size. The camera used by Percoco and Sánchez Salmerón (Canon 400D) has a pixel size of 5.7 μm with lens parameters producing an image scale number of around 0.5. Based on the pixel size and magnification, Percoco and Sánchez Salmerón could achieve a potential minimum error of around 2.9 μm in the absence of noise and assuming perfect reconstruction [86]. In practice, Percoco and Sánchez Salmerón achieved a standard deviation of 8 μm when measuring the diameter of a 8 mm sphere, slightly more than twice the theoretical minimum value.

Figure 2.15 shows the principle of vector uncertainty when triangulating a point of intersection for a simple stereo photogrammetry set-up. Figure 2.15 shows that, given an uncertainty in projection, there will be some area (shown in red) corresponding to the uncertainty in the three-dimensional coordinate.

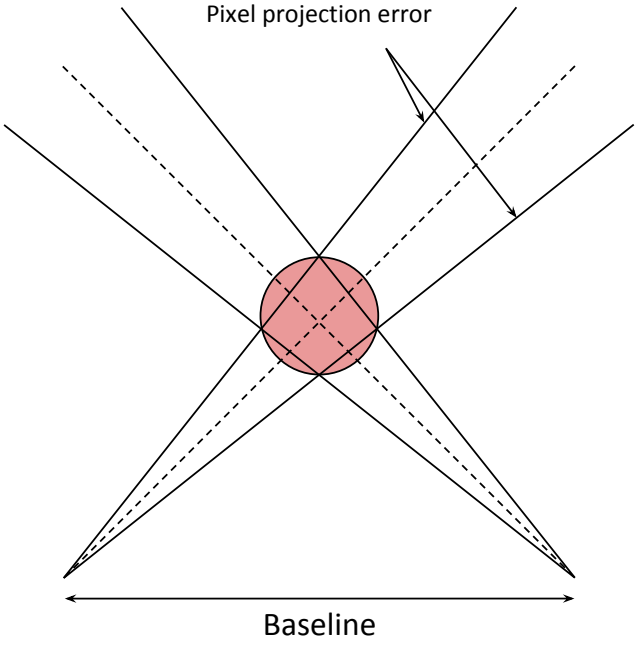

Fig. 2.15 Basic principle of triangulation error due to image error.

The error in the lateral direction of the triangulation is calculated using the magnification at that point; however, the depth error is dependent on other factors. Depth error is highly dependent on both the distance between the cameras, the baseline, and the distance to the point being measured. The equation for depth error is given as a function of image error by

$$\Delta Z = m(h/b)\Delta x \tag{2.27}$$

where b is the baseline, or distance between the cameras [71]. The ratio h/b is dependent on the angle between cameras; for some distance from the object, the depth error will be minimised when the cameras are placed at 90°. As well as camera orientation, the number of images and other external parameters will affect the errors of reconstruction. The effect of external parameters will be discussed in more detail in section 2.5.2.

External factors

As suggested in section 2.5.2, there is a significant effect of the external orientation of the cameras on the level of accuracy achieved in reconstruction. One particular variable to consider is the angle that the camera moves through between consecutive images. The effect of angle change has been investigated by Galantucci et al in order to develop a scanning methodology [39]. By scanning a complex object with a variety of feature types, Galantucci et al was able to investigate the effect of both the step angle between images and the tilt angle of the camera. Galantucci et al found that step angle had no significant effect on reconstruction errors at 20° compared to a 5° step. With only two sets of data to compare, it is difficult to definitively determine the behaviour between these values. The data produced by Galantucci et al does, however, suggest that reconstructions should be consistent, provided the SIFT algorithm can successfully match points between images. One limit Galantucci et al does not determine is the angle at which the SIFT algorithm fails to produce matching points, which would heavily impact the minimum angle between images required to produce a successful reconstruction.

Galantucci et al also report that a higher tilt angle produces a reduced reconstruction error. The method used to determine error by Galantucci et al involved making height comparisons between the reconstruction and the data from a more accurate conoscopic scanner (Optimet Conoscan 400). Based on the data given by Galantucci et al, the error of 2.5 µm quoted for the conoscopic scanner is on the height measurements. The method of error calculation suggest that it is heavily weighted to height measurement accuracies, rather than all three axes. The weighting of accuracy calculation to height measurements will, in itself, result in a preference towards higher tilt angles. The conclusion reached by Galantucci et al on the effect of tilt angle is, therefore, not entirely valid. A more thorough comparison

of the effect of tilt angle on reconstruction errors in all three axes would be required to reach a more valid conclusion on its effect.

Interestingly, there is a split in opinion when considering the effect of number of images on camera calibration and object reconstruction. Some suggest that an increased number of images will produce a better calibration and reconstruction [28, 37, 130] while others suggest that it has a minimal effect or can even be detrimental (see [84] and [36]). The difference in opinions is likely a result of the various different samples and types of measurement being made. Galantucci et al suggests that for relatively simple geometries, such as a single length measurement, the number of images does not have any significant effect. However, for much more complex object, the number of images becomes the most important factor [37]. This effect would result in a distinct split in opinions based on both the sample being measured and the way the accuracy of the reconstruction is evaluated. For a complex object being compared to a complete model, the number of images will have a significant effect on the level of accuracy obtained. However, if the accuracy of a complex sample is only evaluated through a single comparison, such as a step height, it will no longer exhibit a strong relation to the number of images.

It is evident that the effect of camera orientation is a complex issue. There is no general rule for optimal parameters; sample geometry and the type of measurement required all play significant roles in choosing the correct camera positions and angles. In order for micro-scale photogrammetry to become more widely accepted, a general guideline for camera orientation must be produced such that some constancy in measurements in achievable. Determining the best conditions requires significantly more research and testing, and ideally requires a computational method of solving this issue.

2.6 Measurement uncertainty

The strength of photogrammetry lies in its capacity to achieve reconstruction without relying on any additional information other than the images of the object to be measured. Despite the advantages of reconstructing geometries from images, this can only be achieved at the loss of scale information [33]. Additionally, the complex and non-linear process of characterising the system properties and triangulation of the sample form makes the propagation of error through the system difficult to calculate [59]. The lack of a standardised methodology for scaling and consequent lack of traceability, plus a poor understanding of the uncertainty of photogrammetry measurements, are significant hurdles in the widespread use of photogrammetry as a form measurement system.

2.6.1 Arbitrary scale

The solution to the arbitrary scale of photogrammetry reconstructions is a key area of research into the metrological applications of photogrammetry methods. Typically, some physical property of the measurement system and/or the sample must be fixed and calibrated in order for measurements to be appropriately scaled [69]. For example, a calibrated artefact can be placed within the measurement volume of the photogrammetry system allowing the correct scale factor to be applied after the measurement is taken. Although this approach is easily applied, it greatly limits the working volume of the system and requires a calibrated artefact to be available for all measurements.

Another common approach, in the case of a multi-camera system, is to fix the physical distance between the multiple cameras within the system and apply that physical property to the measurement reconstruction [106]. This is a typical approach in many optical form measurement techniques, particularly in structured

light-based measurement systems [26]. The calibrated artefact must be measurable by the system, as well as traceably calibrated to a sufficient level of accuracy for the system under consideration. For contact-based systems, gauge blocks are easily used and widely available whilst being traceably calibrated to very high accuracies ($<$ 0.06 μm for grade K gauge blocks) [32]. However, optical form measurement systems are typically not able to measure gauge blocks due to their highly specular surfaces [64]. Instead, two-dimensional patterned artefacts, such as checkerboards or dot patterns, are typically used in order to calibrate optical form measurement systems [130]. While checkerboard artefacts [130] may be effective for the calibration of optical form measurement systems, they are difficult to calibrate to high accuracies ($<$ 1 μm) and can be difficult to use for non-experts. Ball bars are also a widely used approach for the calibration of optical form measurement systems [101], with the sphere-to-sphere distances providing the scaled length. Similar to two-dimensional patterned artefacts, ball bars are difficult to use for calibration as they exhibit very little observable surface texture for photogrammetry measurements, although texture projection methods have been shown to make this feasible [101].

An alternative method to effectively calibrate optical form measurement systems is to use a combination of self-calibration and direct measurement of a single calibrated length [101]. Self-calibration does not require a calibrated object to effectively characterise the optical system up to some arbitrary scale factor. By then measuring some single calibrated length, such as a gauge block, the arbitrary scale factor of the system can be fixed. Although gauge blocks are typically difficult to measure with optical form measurement systems, this issue is simplified as only a single measurement is required: in fact, limiting the required number of measurements ensures that the gauge block can be measured in the most optimal

position, reducing specular reflection and maximising the measurement accuracy. This methodology is more easily implemented as an intermittent calibration procedure for optical measurement systems whilst only requiring widely available calibration artefacts.

2.6.2 Error modelling

The understanding of error propagation through contact-based coordinate measurement machines (CMMs) is relatively well established [7, 76]. However, the propagation of errors through optical form measurements is still a poorly understood area of research [59, 23, 58, 122, 97]. The non-linear nature of optical form measurement systems makes the analytical approach for the evaluation of the combined standard uncertainty highly complex. The non-linearity of optical methods arises for several reasons, such as choice of triangulation method [50] and optical distortion [69]. Various triangulation methods do not rely on a linear analytical solution, but instead use iterative approaches to minimise reprojection errors. Optical distortion is also particularly problematic as there are no analytical solutions to the inverse mapping of distorted camera points to their undistorted position [50].

A common approach to the assessment of measurement uncertainty in photogrammetry systems is to use comparison with other, more accurate, measurement technologies. For example, Lavecchia et al used a coherence scanning interferometer (CSI) to compare photogrammetry measurements to a more accurate measurement of a step height [59]. Although comparison with more accurate measurements provides some insight into the accuracy of the system, it is limited in the information that can be extracted about how errors propagate through the system. Comparison with other measurements only allows the user to observe the relative effects of

changing certain aspects of the system, such as camera angles and reconstruction methods. However, measurement comparisons do not provide any insight into the effect of the uncertainties of the system properties that cannot be as easily altered. For example, the requirements on the mechanical stability of the system and the performance of different cameras can be tested prior to the system being manufactured.

Monte Carlo (MC) based methods provide an ideal solution for the evaluation of the combined standard uncertainty for such complex systems [54]. Essentially, the Monte Carlo approach involves the simulation of many measurements for which the influence factors are varied according to their predetermined distribution [54]. The distribution of the simulated measurand can then be used to evaluate the combined standard uncertainty, as well as the individual contributions from each influence factor. Di Leo et al show that through MC simulations, it is possible to investigate the effect of varying system properties and isolating the effect of various parameters [23].

2.7 Performance verification

The only verification standards currently available for photogrammetry systems is VDI/VDE 2634, of which part 2 and part 3 are specifically required [114, 115]. VDI/VDE 2634 part 2 is for optical measurement systems based on area scanning making it appropriate for the verification of stereo-photogrammetry systems. VDI/VDE 2634 part 3, however, is instead applicable to mutliple view systems such as photogrammetry systems based on 3 or more images. In this section, the acceptance tests outlined by VDI/VDE 2634 part 2 and part 3 are outlined for chapters 4 and 5 in which the tests are adapted and applied to two photogrammetry systems that were developed as part of this work. The acceptance tests are performed by

comparing the manufacturer quoted values against the results of the verification tests described below. If the results of tests fall below the manufacturer quoted value, the system passes the verification test.

2.7.1 Area view system verification

Probing error

The probing error is defined in two separate parameters: form probing error, P_F, and size probing error, P_S. In VDI/VDE part 2, the probing errors are evaluated through the measurement of a calibrated sphere measured in at least ten abritrary positions within the measurement volume such as those shown in figure 2.16. The sphere radius must be between 0.02 and 0.2 of the longest diagonal of the measurement volume and the form error must be explicitly less than the expected value of the probing errors.

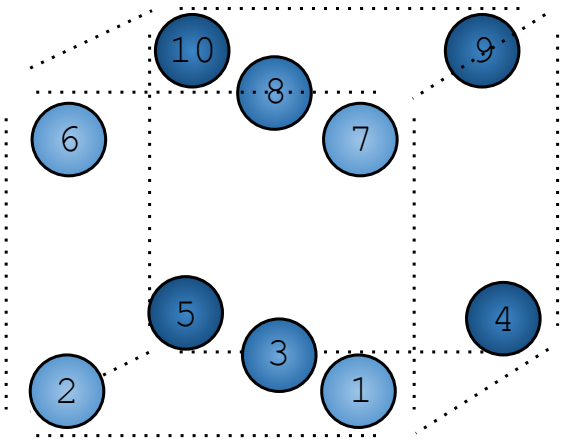

Fig. 2.16 Arbitrary sphere positions for VDI/VDE 2634 part 2.

Once the ten measurements of the test sphere have been made, a least-squares sphere is applied to each point cloud in which a maximum of three in every 1000 points may be removed. The form probing error, P_F, can then be calculated as the maximum range of the radial deviations of the point cloud. Additionally, the form probing error can be calculated from

$$P_S = D_a - D_r \tag{2.28}$$

where D_a is the diameter of the least-squares fit sphere and D_r is the sphere's calibrated diameter.

Sphere spacing error

The sphere spacing error, SD, quality parameter is determined by measuring the calibrated distance between two spheres of a ball bar. The ball bar must be measured in at least seven different orientations, as shown in figure 2.17. The length of the ball bar must be at least 0.3 of the longest diagonal of the measurement volume and the diameter of the spheres between 0.02 and 0.2 of the longest diagonal. The ball bar length must also be calibrated to an uncertainty substantially less than the expected spacing error of the system. The sphere spacing error is then calculated from

$$SD = L_a - L_r \tag{2.29}$$

where L_a is the measured length and L_r is the calibrated length. The measured length is determined through the least-squares fit of each sphere in which a maximum of three per 1000 points can be removed from the fit. The measured distance is then the geometric distance between the two sphere centres.

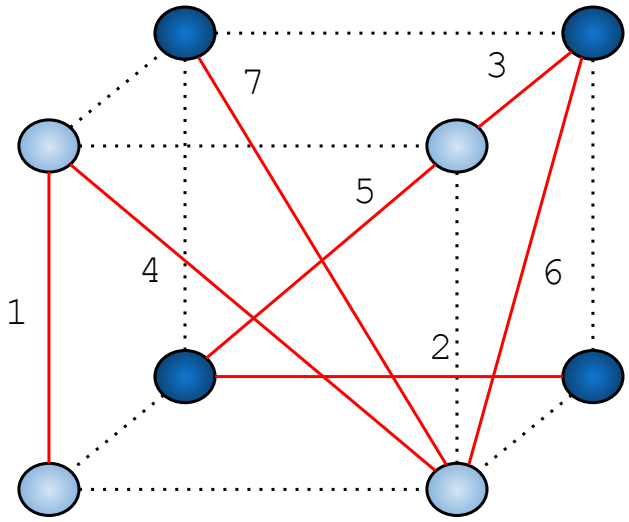

Fig. 2.17 Ball bar orientations according to VDI/VDE 2634 part2.

Flatness measurement error

The flatness measurement error F quality parameter is evaluated through the measurement of a flat plane. The flat plane must be measured in at least six different orientations as shown in figure 2.18. The width of the flat must be at least 50 mm and with a length of at least 0.5 of the longest diagonal of the measurement volume. Additionally, the flatness of the artefact must be substantially less than the expected flatness measurement error. A least-squares plane fit is then applied to the point cloud in which a maximum of three points per 1000 can be removed. The flatness measurement error, F, is then defined as the maximum deviation of all the points from the fitted plane.

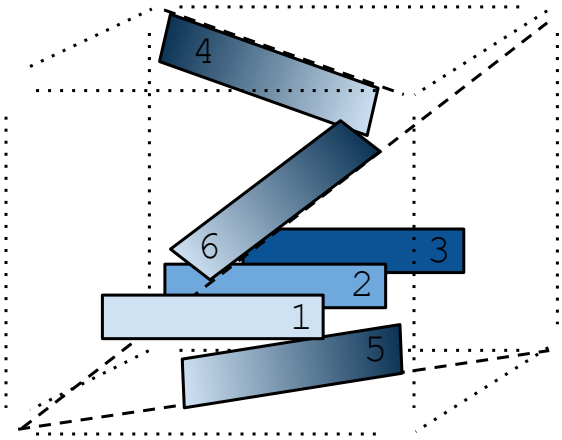

Fig. 2.18 Flatness measurement orientations according to VDI/VDE 2634 part 2.

2.7.2 Multi-view system verification

VDI/VDE 2634 part 3, by definition, is the standard to be used for the verification of a multi-view based optical measurement system. However, VDI/VDE 2634 part 3 is designed around measurement systems that make multiple areal measurements. Photogrammetry based on three or more images is not a series of areal measurements, but in fact the entire measurement process is based on the multi-view aspect. Therefore, it is difficult to directly apply VDI/VDE 2634 part 3 standards without significant adaptations. As a result, the majority of work typically attempts to verify photogrammetry systems using altered versions of the VDI/VDE 2634 part 3 standards. For example Lavecchia et al design their own artefact with a range of features for verification and calibration [58]. However, Percoco et al instead attempt to slightly alter the VDI/VDE standards in order to adhere to the limits of the photogrammetry system [85]. In particular, Percoco et al adapt the ball bar arrangement seen in figure 2.17 in order to be applicable to measurement systems

based on multiple views and a rotation stage. In chapters 4 and 5 further developments to the VDI/VDE 2634 part 2 and part 3 standards are demonstrated on two photogrammetry systems. These chapters provide novel techniques of applying standards to photogrammetry systems that would otherwise be difficult.

Chapter 3

System characterisation and calibration

3.1 Introduction to system characterisation and calibration

The aim of the work presented in this chapter is to model a stereo-camera based photogrammetry system in order to assess the expected measurement uncertainties as well as provide a traceable method of scaling subsequent measurements. The scaling will be performed using a laser interferometer and verified using a calibrated gauge block. The measurement uncertainty is considered as made up of two separate factors: geometric uncertainty and uncertainty on the global scale factor. The outcome of this chapter is an understanding of the measurement uncertainty produced by the system in question, as well as the identification of key areas for future work for the improvement of the technology.

3.2 Methodology for system characterisation and calibration

The methodology of this work falls into four main stages: 1. identification and evaluation of the measurement influence factors, 2. Monte Carlo simulation of the stereo-camera system, 3. evaluation of the global scale factor and 4. the verification of the coordinate measurement uncertainty and scale factor through the measurement of gauge blocks.

3.2.1 Uncertainty contributions

The influence factors were evaluated through two methods, type A and type B, as defined by the Guide to the Expression of Uncertainty in Measurement [53]. A list of the influence factors, their evaluation method, their distribution and their designation can be seen in table 3.1. The influence factors to be evaluated through the type A method correspond to the intrinsic and extrinsic properties of the stereo-camera system and are evaluated through a repeated calibration procedure. The uncertainties of the intrinsic and extrinsic properties are given by the characterisation algorithm [130]. As the distribution of the stereo-camera parameters is unknown, a rectangular distribution has been selected for these influence factors in order to provide a conservative estimate of their contribution.

Unlike type A evaluated uncertainties, type B uncertainties are instead evaluated using prior results, manufacturer specifications and experience of using the system. The key parameters to be evaluated using the type B method are the uncertainty in the laser interferometer measurements and environmental factors. However, the most important factor for the type B evaluation is the uncertainty on the feature position. The uncertainty on the feature position is in fact a combination of a wide

Table 3.1 Contributions to the measurement uncertainty

Influence factor	**Evaluation method**	**Distribution**	**Designation**
Focal length	Type A	Rectangular	$u(f_u)$,$u(f_v)$
Principle point	Type A	Rectangular	$u(u_0)$,$u(v_0)$
Radial distortion	Type A	Rectangular	$u(k_1)$,$u(k_2)$,$u(k_3)$
Tangential distortion	Type A	Rectangular	$u(s_1)$,$u(s_2)$
Camera rotation	Type A	Rectangular	$u(\theta)$,$u(\phi)$,$u(\rho)$
Camera translation	Type A	Rectangular	$u(T_x)$,$u(T_y)$,$u(T_z)$
Feature location	Type A	Normal	$u(u_p)$,$u(v_p)$
Temperature of system	Type A	Rectangular	$u(Temp)$
Measurement uncertainty of the laser interferometer	Type B	Rectangular	$u(cal)$

range of factors; such as, focus, feature detection method, feature size, depth-of-field, chromatic aberrations, sensor resolution and surface properties. Whereas all the other influence factors can be explicitly defined, the feature location uncertainty will be considered for a range of values typically expected in order to provide an indication of the measurement uncertainty in a variety of scenarios.

3.2.2 Software model

The stereo-photogrammetry system consists of two cameras for which a three-dimensional grid of points is imaged using the ideal system and then triangulated using the perturbed system. The perturbed system is produced by applying an offset to influence factors under investigation according to the probability distribution of that factor. The spatial deviation of the triangulated points can then be used to evaluate the accuracy of the measurement. The projection of

three-dimensional points onto the camera sensor is described by [69]

$$s_m \begin{bmatrix} u_{n,m} \\ v_{n,m} \\ 1 \end{bmatrix} = K_n \begin{bmatrix} & R_n & & T_n \\ 0 & 0 & 0 & 1 \end{bmatrix} \begin{bmatrix} X_m \\ Y_m \\ Z_m \\ 1 \end{bmatrix} = P_n \begin{bmatrix} X_m \\ Y_m \\ Z_m \\ 1 \end{bmatrix}, \tag{3.1}$$

where $(u_{m,n}, v_{m,n})$ are the pixel coordinates of the point m in camera n, s_m is a normalisation factor, K_n is the intrinsic matrix for camera n, R_n and T_n are the rotation and translation matrices of camera n, P_n is the camera projection matrix and (X_m, Y_m, Z_m) are the coordinates of point m. A schema of the projection process is shown in figure 3.1, where the cube represents the measurement volume.

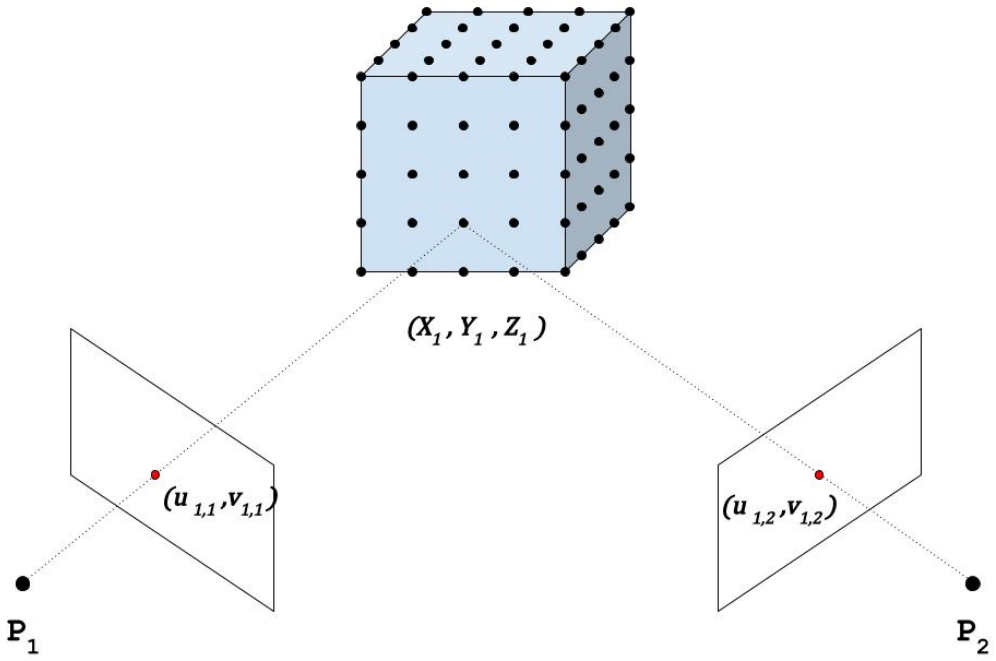

Fig. 3.1 Schema of the projection of a world point onto two images.

In addition to the linear projection process, there is an additional stage in which distortion parameters are applied in order to account for the non-linear distortion of the camera optics. As only the image pixel coordinates and camera intrinsic and extrinsic properties will be known, a minimum of two cameras is required in order to triangulate the position of the point in three-dimensional space. The linear solution to the triangulation is described by

$$A \begin{bmatrix} X_m \\ Y_m \\ Z_m \end{bmatrix} = \begin{bmatrix} um,1p_1^3 - p_1^1 \\ vm,1p_1^3 - p_1^2 \\ um,2p_2^3 - p_2^1 \\ vm,2p_2^3 - p_2^2 \end{bmatrix} \begin{bmatrix} X_m \\ Y_m \\ Z_m \end{bmatrix}, \tag{3.2}$$

where p_n^k is row k of the n camera projection matrix. The triangulated point can then be calculated as a solution to equation 3.2 through the calculation of the singular value decomposition of A. The triangulated point is then given as the smallest singular value of A.

Once the measured points have been triangulated, they are shifted in order to ensure their centre of mass coincides with that of the original grid of points, removing any systematic effects. The difference between the triangulated points and the original location is then calculated. This process is then repeated thousands of times with varying system properties in order to assess the expected response of the system. The details of how each property is perturbed will be discussed in the following sections.

Intrinsic parameters

The intrinsic properties of the stereo-photogrammetry system include the information about the internal properties of the camera, such as focal length, sensor size,

sensor position and the distortion effect of the imaging lens. The application of the intrinsic parameters is shown in equation 3.1 in terms of K given by

$$K = \begin{bmatrix} f_u & 0 & u_0 \\ 0 & f_v & v_0 \\ 0 & 0 & 1 \end{bmatrix}, \tag{3.3}$$

where f_u and f_v describe the focal length of the lens in the u and v direction respectively and u_0 and v_0 are the pixel coordinates of the intersection of the optical axis with the imaging plane. The inclusion of uncertainty within the intrinsic factors is straightforward as the offset value can be generated according to a rectangular distribution and added to each term. However, as the principle point is mainly a term for the characterisation of the centre of distortion, the uncertainty term is only added to the principle point when calculating the distortion correction.

Distortion

The distortion of the imaged object is a result of several factors, including the optical effects of the lenses and misalignment of the optical components. The two key forms of distortion are the radial and tangential components [69]. The influence of the tangential distortion was found to be lower than 0.1 pixels and substantially increased the calculation times for the Monte Carlo simulations. For the scope of this work, only the radial component of the distortion will be considered in order to simplify and accelerate the simulations. The radial distortion of image points is described by

$$u_d = u(1 + k_1 r^2 + k_2 r^4 + k_3 r^6 + ...), \tag{3.4}$$

$$v_d = v(1 + k_1 r^2 + k_2 r^4 + k_3 r^6 + ...), \tag{3.5}$$

where (u_d,v_d) is the distorted image coordinate of the points (u,v), r is the radius given by $r = \sqrt{(u-u_0)^2 + (v-v_0)^2}$ and k_n is the n^{th} distortion parameter. Typically, in order to determine the undistorted image coordinates from the known distorted points and distortion parameters, a non-linear solution is required. However, it is possible to define an inverse distortion given by

$$u_d = u(1 + b_1 r_d^2 + b_2 r_d^4 + b_3 r_d^6 + ...), \tag{3.6}$$

$$v_d = v(1 + b_1 r_d^2 + b_2 r_d^4 + b_3 r_d^6 + ...), \tag{3.7}$$

where r_d is the radius of the distorted points and b_n is the n^{th} inverse distortion parameter [25]. By defining the inverse distortion, the offset to the undistorted image points due to a difference in inverse distortion parameters is given by the equation

$$\Delta u = u_1 - u_2 = u_d(1 + b_{1,1} r_d^2 + b_{1,2} r_d^4) - u_d(1 + b_{2,1} r_d^2 + b_{2,2} r_d^4), \tag{3.8}$$

which can be further simplified to

$$\Delta u = u_d(\Delta b_1 r_d^2 + \Delta b_2 r_d^4), \tag{3.9}$$

where Δb_n is the offset on the n^{th} inverse distortion parameter and Δu is the corresponding offset to the pixel position. The conversion from distortion parameters to the inverse distortion parameters is given by

$$b_1 = -k_1, \tag{3.10}$$

$$b_2 = 3k_1^2 - k_2, \tag{3.11}$$

$$b_3 = -12k_1^3 + 8k_1k_2 - k_3, \tag{3.12}$$

$$b_4 = 55k_1^4 - 55k_1^2k_2 + 5k_2^2 + 10k_1k_3 - k_4. \tag{3.13}$$

Higher order terms for b can be defined, but four were used as the contribution from higher orders is negligible. Using equations 3.10 to 3.13, it is possible to calculate the uncertainty in each inverse distortion parameter using

$$U(b_n) = \sqrt{\sum_{i=1}^{4}(\frac{\delta b_n}{\delta k_i})U^2(k_i)}. \tag{3.14}$$

By using the associated uncertainties for the distortion parameters, the uncertainty on each inverse distortion parameter can be calculated and used to generate a normally distributed random offset to each parameter. With the random offsets to the inverse distortion parameters Δb_n, the offset in the pixel position can then be computed using equation 3.9.

Extrinsic properties

The extrinsic properties of the stereo-photogrammetry system correspond to the relative orientation between the two cameras. Physically, this represents the rotation and translation between the two cameras. For this work, one camera was fixed in space at the origin, with the second camera being subject to random perturbations. The rotational component to this transformation is implemented by applying a rotation matrix to the second camera in the form

$$R = R_x(\theta)R_y(\phi)R_z(\rho), \tag{3.15}$$

where $R_x(\theta)$ is a rotation of θ around the x-axis, $R_y(\phi)$ is a rotation of ϕ around the y-axis and $R_z(\rho)$ is a rotation of ρ around the z-axis. The angles θ, ϕ and ρ are

randomly generated from a normal distribution determined by the uncertainty on those angles and converted into a rotation matrix. This rotational offset matrix is then applied to the original matrix in order to produce the perturbation in rotation.

The translation matrix between the cameras is of the form

$$T = \begin{bmatrix} T_x \\ T_y \\ T_z \end{bmatrix}, \tag{3.16}$$

where T_x, T_y and T_z are the translations of the second camera in the x, y and z axis, respectively. However, as the magnitude of the translation matrix will only lead to a scale factor error, it is useful to isolate the magnitude and direction of the translation uncertainty. The camera translation can be represented in a spherical-polar coordinate system according to the equations

$$T_r = \sqrt{T_x^2 + T_y^2 + T_z^2}, \tag{3.17}$$

$$T_\theta = arccos\frac{T_z}{T_r}, \tag{3.18}$$

$$T_\phi = arctan\frac{T_y}{T_x}, \tag{3.19}$$

where T_r, T_θ and T_ϕ is the radius, elevation and azimuth of the second camera with respect to the first. As the magnitude of T_r will only affect the effective scale of the reconstruction, its uncertainty is taken to be zero for the Monte Carlo simulation and will instead be evaluated in section 2.4. Instead only the angular uncertainty

of the second camera is considered using the equations

$$u^2(T_\theta) = \left(\frac{T_z T_x}{T_r^3\sqrt{1-\frac{T_z^2}{T_r^2}}}\right)^2 u^2(T_x) + \left(\frac{T_z T_y}{T_r^3\sqrt{1-\frac{T_z^2}{T_r^2}}}\right)^2 u^2(T_y) + \left(\frac{T_x^2+T_y^2}{T_r^3\sqrt{1-\frac{T_z^2}{T_r^2}}}\right)^2 u^2(T_z), \tag{3.20}$$

$$u^2(T_\phi) = \left(\frac{T_x^2}{T_x^2+T_y^2}\right)^2 u^2(T_x) + \left(\frac{T_y}{T_x^2+T_y^2}\right)^2 u^2(T_y). \tag{3.21}$$

According to the angular uncertainties calculated using equations 3.20 and 3.21, normally distributed random angular offsets are added to the spherical polar coordinates of the second camera before being converted back to Cartesian coordinates.

3.2.3 Scaling factor

The scale factor of the stereo-photogrammetry system was evaluated using a high-accuracy laser interferometer (Renishaw XL-80). As can be seen in figure 3.1, the stereo-photogrammetry system was used to track a checkerboard artefact placed on the gantry plate of a linear actuator. The linear actuator was then used to translate the checkerboard artefact over a 90 mm travel range whilst the linear position was monitored using the laser interferometer. The linear motion observed by the stereo-photogrammetry system could then be compared to the linear distance provided by the laser interferometer in order to correct for scale factor errors introduced by the checkerboard calibration procedure.

The laser interferometer system utilises a refractive index corrector unit and has a stated relative accuracy of $\pm\ 5 \times 10^{-5}$ %, corresponding to a maximum error of around 45 nm over the complete range of motion used in this work (100 mm). The

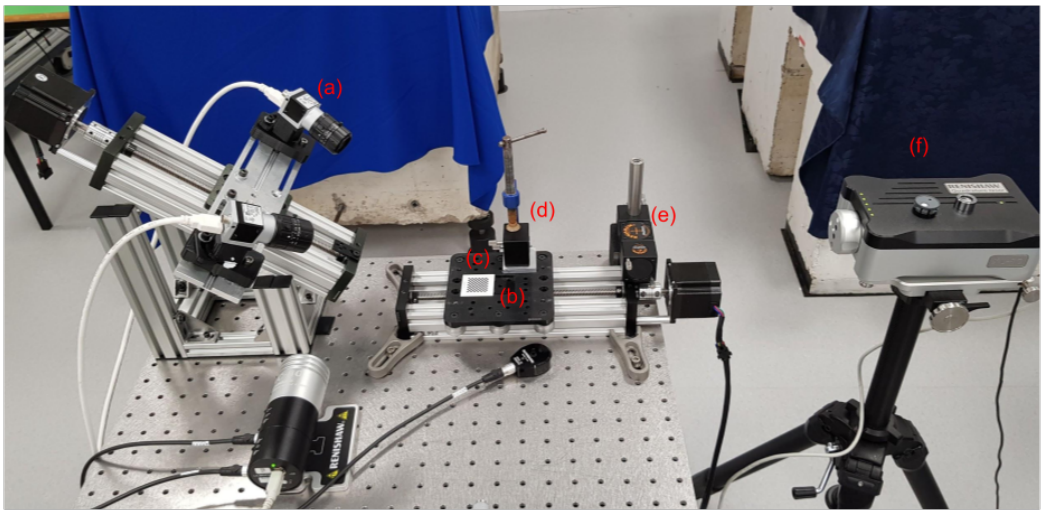

Fig. 3.2 Scale factor measurement set-up. (a) Stereo-photogrammetry system, (b) gantry plate, (c) checkerboard artefact, (d) retro-reflector, (e) beam splitter and (f) laser interferometer.

uncertainty on the calculated scale factor is given by

$$u(length) = \sqrt{u^2(cal) + u^2(p)}, \tag{3.22}$$

where $u(cal)$ is the uncertainty of the laser interferometer measurements and $u(p)$ is the uncertainty of the stereo-photogrammetry measurements. The uncertainty of the stereo-photogrammetry measurements was evaluated through 20 repeat measurements through the entire travel range of 100 mm.

3.2.4 Gauge block measurement

In order to verify the performance of the system, a calibrated 5 mm gauge block that has been wrung to a reference platen was measured. Although the gauge block exhibits a highly specular surface, a laser line projected on to the surface provides sufficient diffusely reflected light to triangulate points on both the gauge block and platen surface. As the laser line does not provide a pixel-to-pixel correspondence, a

line was fit to the two surfaces and the epipolar geometry [16] of the stereo-system was used to extract the corresponding points. The measurement was performed five times with the stereo-cameras rigidly mounted with respect to the gauge block, with the laser line scanned over the surface in order to provide enough points to fit a plane to the data.

3.3 Results

3.3.1 Software model results

Verification of distribution

In order to ensure that the number of iterations was sufficient to accurately represent the measurement uncertainty, the first step was to evaluate the standard deviation of the three-dimensional coordinate error as a function of number of iterations. Figure 3.3 shows the mean standard deviation of the position errors in the x axis as a function of number of iterations. As figure 3.3 shows, the variation in the uncertainty very quickly drops to less than 2 nm after only 1000 iterations. Between 4000 and 10 000 iterations, the standard deviation of the results falls below 1 nm. As the results are calculated as the mean of over 1000 points within the measurement volume, the effective number of iterations is a thousand times more than the actual number of iterations. For the sake of accuracy, 10 000 iterations were performed in order to ensure the extracted values are as representative as possible.

Contributions of each factor

Each influence factor from table 3.1 was evaluated through the calibration of the stereo-photogrammetry system using a checkerboard calibration artefact. The cameras used for this work were 12 mega-pixel sensors (4024 pixels by 3036 pixels)

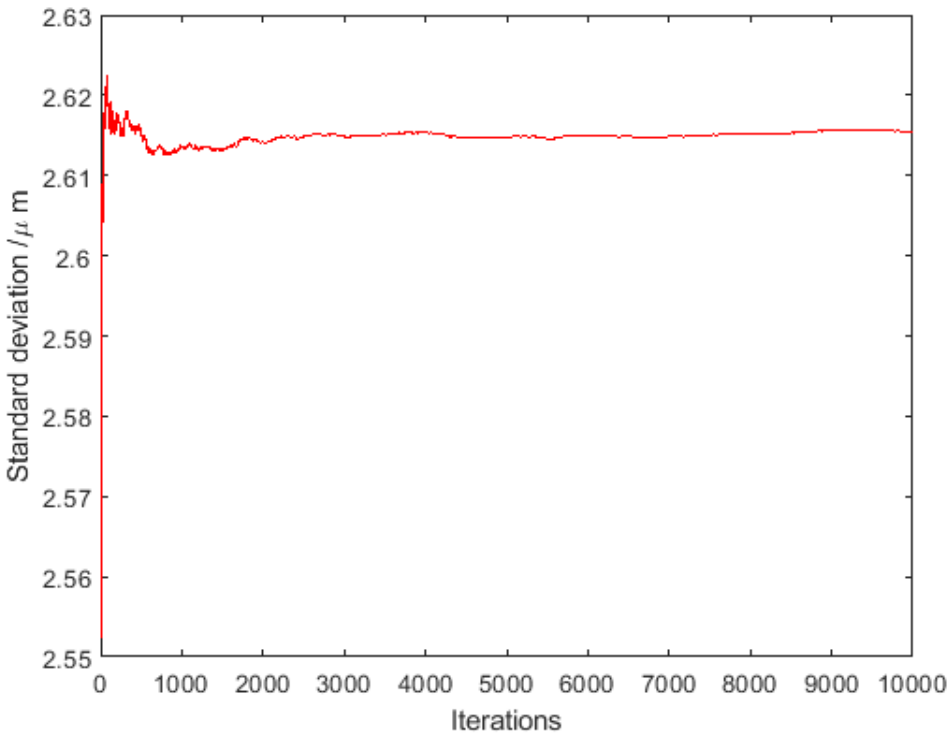

Fig. 3.3 Standard deviation of errors in x axis against number of iterations.

with 16 mm lenses that were found to be 16.74 mm and 16.66 mm when calibrated. The stereo-photogrammetry was found to have a baseline distance between the cameras of 199.35 mm and an angle of 38.64 ° between cameras. This baseline and camera angle leads to a convergence point of the two camera views at 301 mm away from each camera. At 301 mm, the magnification of each camera is around 0.055, with an optical resolution of 33 μm due to the pixel pitch of 1.85 μm. However, an f-stop value of 6 was used in order to provide a sufficient depth-of-field, leading to diffraction limited system with an airy disk with a radius of 8 μm. The diffraction limitation leads to an optical resolution of 0.145 mm at 301 mm away from the camera. The first and second order radial distortion parameters for the cameras were found to be -0.135 and 0.24 for the first camera and -0.13 and 0.17 for the second.

Table 3.2 shows the values of the influence factors that were evaluated, as well as their contribution to the combined standard uncertainty in the x, y and z axes. The combined standard uncertainty is calculated for each axis as

$$u_{comb} = \sqrt{\sum_{n=1}^{N} u_n^2}, \tag{3.23}$$

in which u_n is the uncertainty contribution of influence factor n and N is the total number of influence factors. The combined standard uncertainty for the contributions in table 3.2 was 10.1 μm, 6.0 μm and 14.8 μm in the x, y and z axis, respectively.

The Degrees of Freedom (DoF) for the influence factors are also shown in table 3.2. According the GUM methodology, the Welch–Satterthwaite equation was used to calculate the degrees of freedom on the combined standard uncertainties as 3, 37 and 96 giving coverage factors of 3.18, 2.03 and 1.98 for a 95 % confidence interval.

Table 3.2 Measurement standard deviations for each factor

Influence factor	**Value**	**DoF**	**Uncertainty /μm**		
			x	y	z
$u(u_p)$,$u(v_p)$	0.1 (pixels)	∞	3.1	2.3	6.7
$u(f_u)$,$u(f_v)$	0.82, 0.84 (pixels)	2244	1.7	1.3	3.6
$u(\theta)$,$u(\phi)$,$u(\rho)$	1.84, 1.52, 0.71 ($*10^{-4}$ radians)	14	9.1	4.7	9.1
$u(T_x)$,$u(T_y)$,$u(T_z)$	13, 8, 27 (μm)	14	1.5	0.4	3.2
$u(k_1)$,$u(k_2)$	0.001, 0.0362	2244	2.1	2.5	8.2

Based on the coverage factors, the expanded standard uncertainties are 32.1 μm, 12.1 μm and 29.2 μm for a 95 % confidence interval.

Influence of feature uncertainty

In order to assess the effect of feature position uncertainty, the Monte Carlo simulation was performed for ten different feature position errors between 0 and 1 pixels. The choice in range of pixels to simulate was chosen arbitrarily to reflect of values that would be typically expected. As can be seen in figure 3.4, the relationship between pixel error and uncertainty in the x axis is approximately linear.

Systematic error contribution

Although the uncertainties in the intrinsic and extrinsic stereo-camera parameters have been assumed to be randomly distributed, the uncertainties used in fact represent the uncertainty in the characterisation process. For any given measurement, the errors on the system parameters are likely to be mainly systematic, with a substantially smaller random component representing the mechanical stability of the system. As a result, it is useful to visualise how systematic offsets will propagate through the measurement and to see how they manifest in the measurement errors. However, as the uncertainties cannot be characterised easily, the combined standard uncertainties quoted in section 3.1.2 represent a realistic expectation of

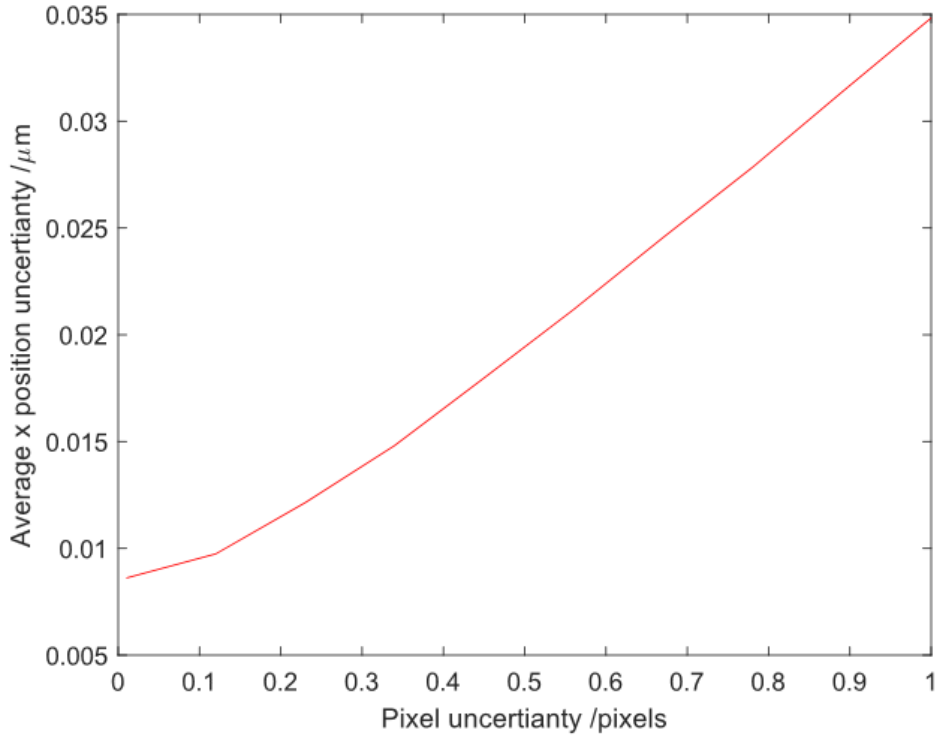

Fig. 3.4 Plot of average uncertainty in the x axis against level of feature position uncertainty.

what can be achieved. However, it is important to understand how systematic errors in the extrinsic and intrinsic properties manifest. In order to demonstrate the effect of systematic offsets, the computational model was used to simulate the triangulation errors in the presence of offsets applied to the system properties. As can be seen in figures 3.5 to 3.8, systematic offsets in the system properties lead to complex distortions in the measurement volume. Spatial offsets, differences in scale factor for each axis and non-linear distortions in the measurement volume are all observed for individual factors, with real measurements being the result of a combination of all the observed effects.

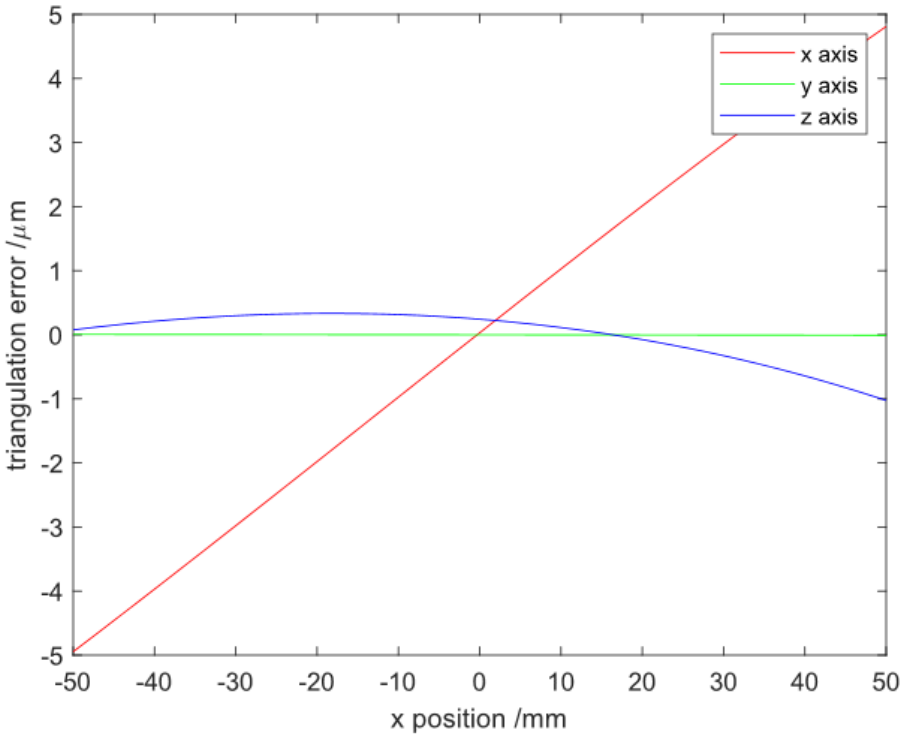

Fig. 3.5 Spatial variation of errors in x, y and z axis in the presence of an offset in the focal length.

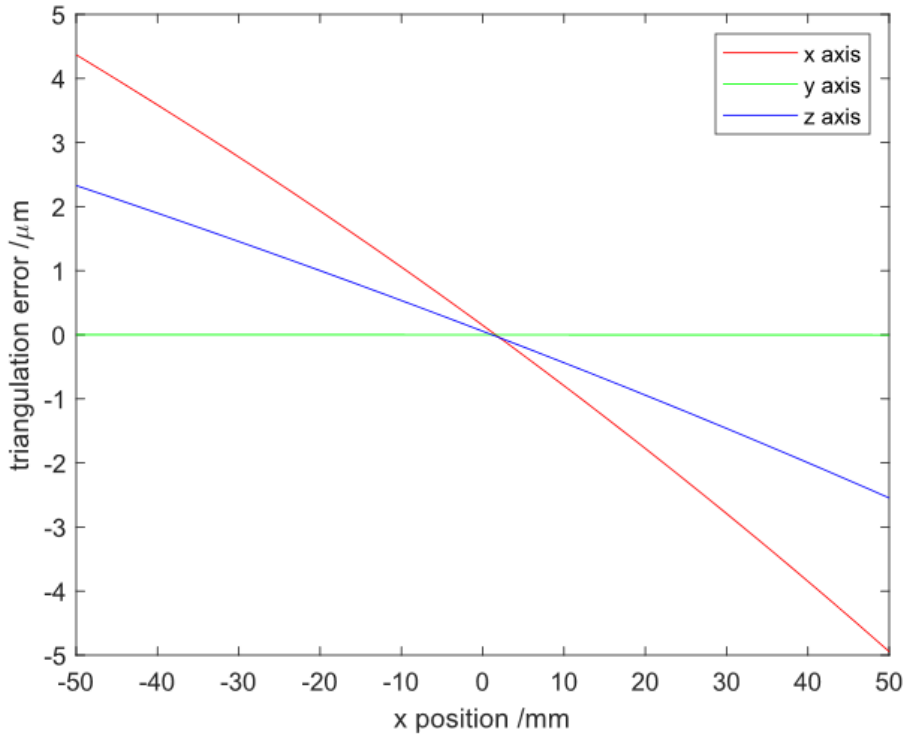

Fig. 3.6 Spatial variation of errors in x, y and z axis in the presence of an offset in the translation of the second camera.

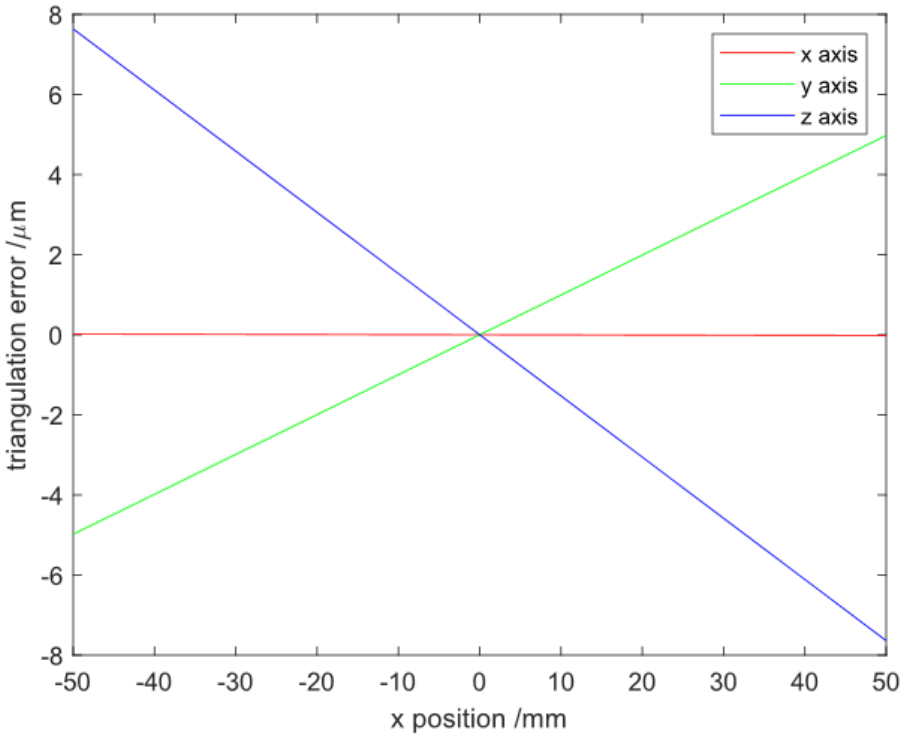

Fig. 3.7 Spatial variation of errors in x, y and z axis in the presence of an offset in the rotation of the second camera.

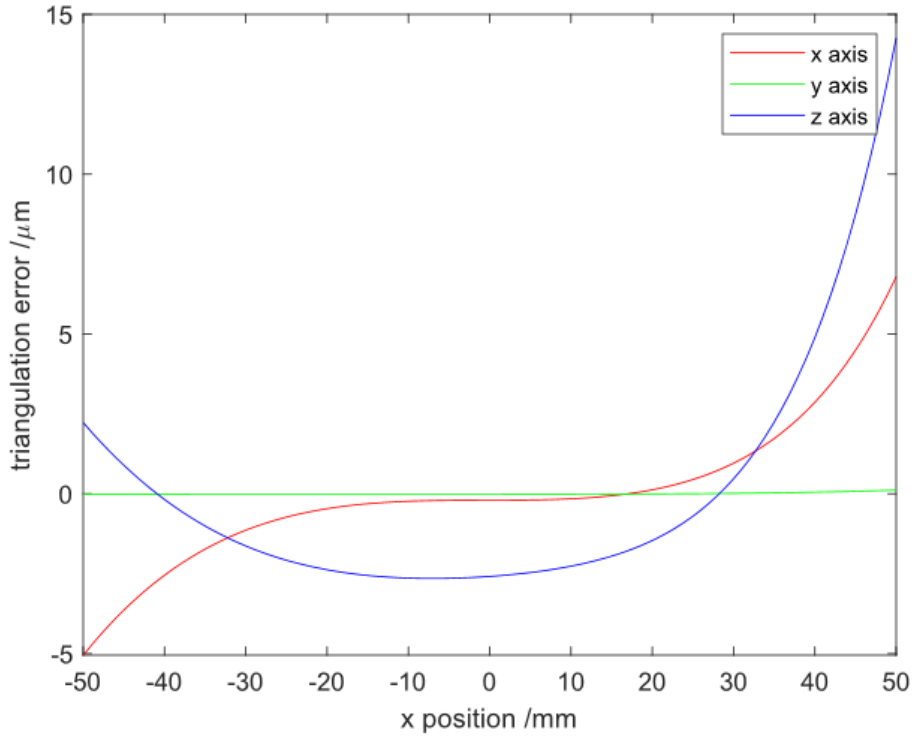

Fig. 3.8 Spatial variation of errors in x, y and z axis in the presence of an offset in the radial distortion parameters.

Spatial variation of measurement uncertainty

In addition to the spatial variation caused by systematic errors, there is also a variation of the combined standard uncertainty within the measurement volume. An additional Monte Carlo simulation was performed for a line of points in the x axis and the standard deviation in each axis was calculated for 100 000 iterations. As can be seen in figure 3.9, the triangulation uncertainty shows significant variation through the measurement volume. Variations of the order of 5 μm can be seen in both the y and z axes, leading to substantial variations in the combined standard uncertainty throughout the measurement volume.

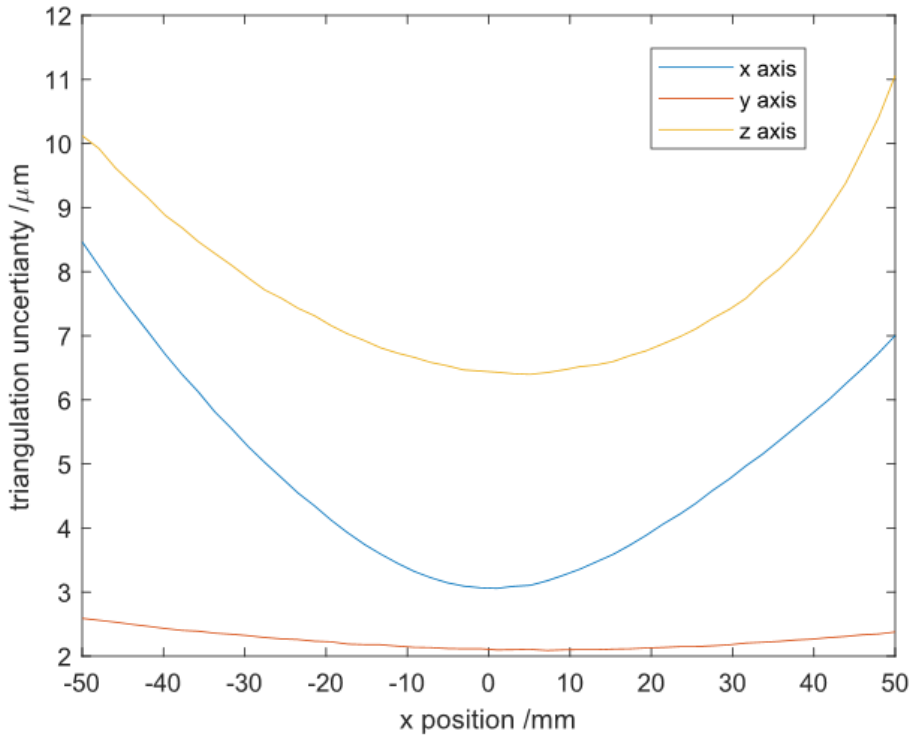

Fig. 3.9 Spatial variation of average uncertainty in x, y and z axis for random errors.

3.3.2 Scaling factor results

The uncertainty on the scale factor of the stereo-photogrammetry system was evaluated using a linear actuator tracked with a laser interferometer. A checkerboard artefact was placed on the linear actuator and tracked with the stereo-photogrammetry system. By then taking the average translation between the various checkerboard positions and comparing with the interferometer data, the scale factor of the system could be determined.

Figure 3.10 shows the stereo-photogrammetry based displacement, compared to the interferometer translation for two different orientations of the actuator in the measurement volume. A linear regression was then used to determine the scale factor for each repeat measurement with a standard deviation of the scale factor over all 20 measurements of 0.0068 %. The uncertainty on the scale factor corresponds to a measurement uncertainty contribution of 6.8 μm on a length measurement of 100 mm.

A result of the scale factor data is the shape of the plot of the linear displacement error for the photogrammetry system. Figure 3.11 shows the displacement errors for twenty repeat measurements of a 90 mm travel range with associated uncertainty on those points. As can be seen, there is a highly repeatable pattern in the displacement data, likely corresponding to the systematic offsets discussed in section 3.3.1. In fact, the standard deviation on any one point was typically on the order of 5 μm, despite a lack of accurate alignment between measurements.

3.3.3 Gauge block measurement

The calibrated gauge block was measured using the stereo-photogrammetry system and a laser line. As can be seen in figure 3.12, the gauge block measurement was split in order to provide points for a plane fit to be applied to the upper and lower

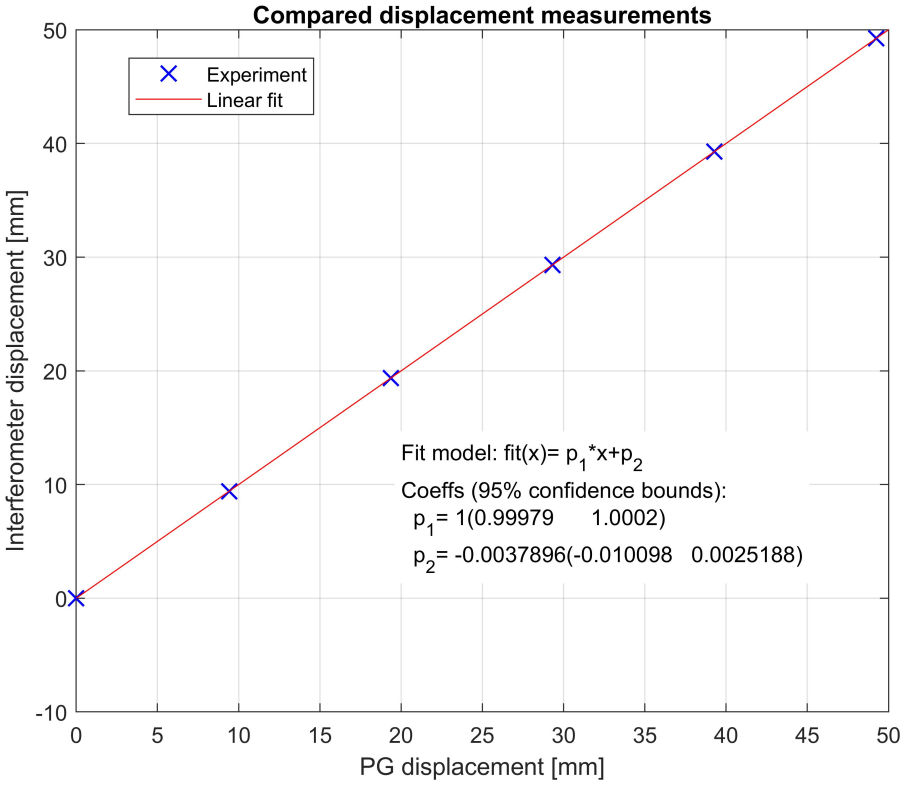

Fig. 3.10 Plot of translation of stage according to the photogrammetry system and the laser interferometer.

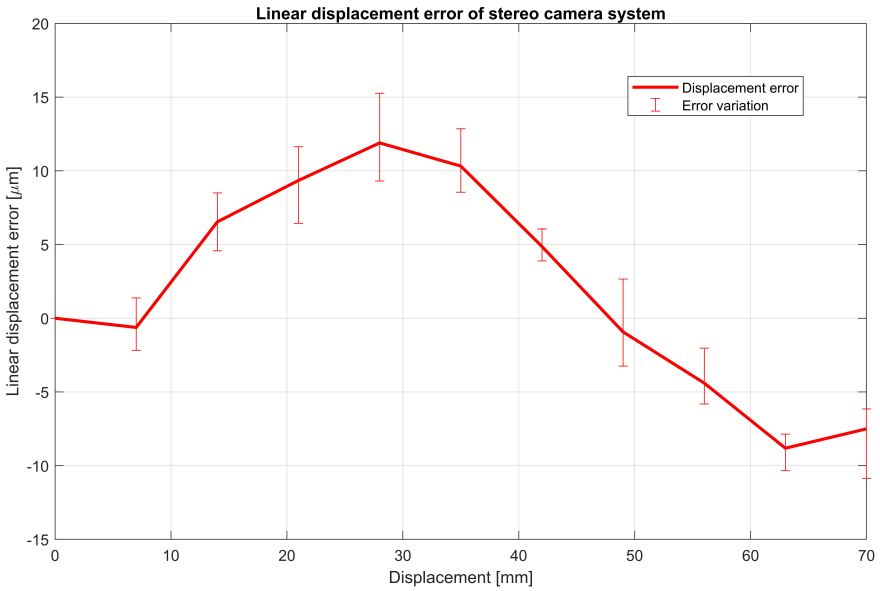

Fig. 3.11 Residual error of photogrammetry measurements.

surfaces. Once orientated with the platen surface on the z axis plane, the standard deviations and heights of each surface were calculated. The gauge block and platen points were found to have standard deviations from a fitted plane of 32 μm and 27 μm respectively. According to the stereo-photogrammetry measurement, the gauge block height was found to be 5.0086 mm, compared to the calibrated value of 5.0006 mm, resulting in a length measurement error of 8 μ m.

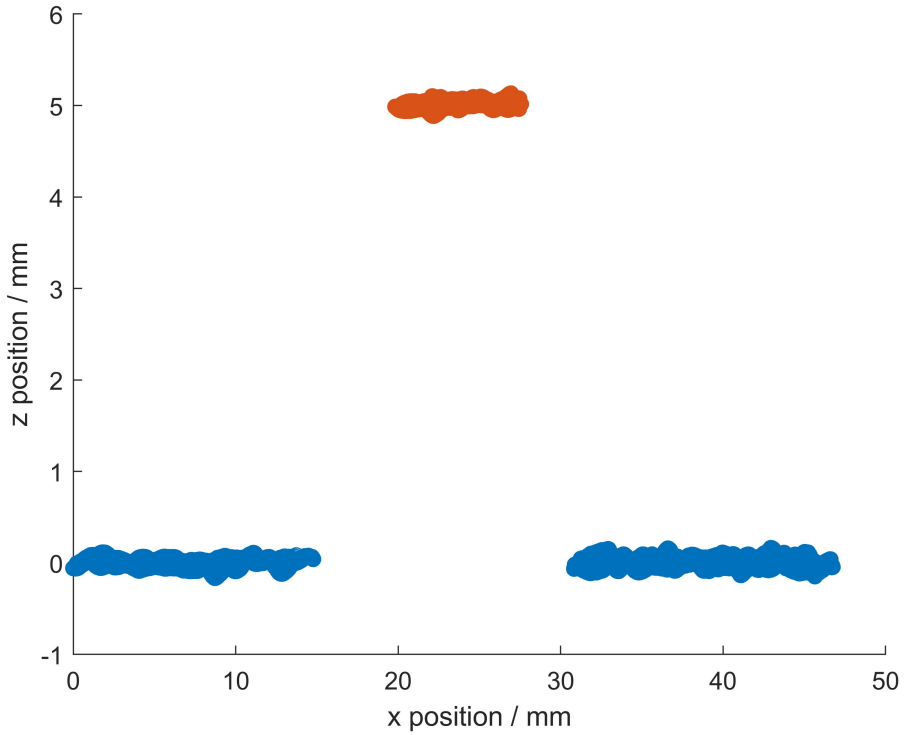

Fig. 3.12 Point cloud of gauge block points (Red points correspond to the gauge block surface and blue to the platen surface).

3.4 Discussion

3.4.1 Software model results

The results from the Monte Carlo simulations provide information about the importance of specific factors when considering improvements of a measuring system. As table 3.2 shows, the rotation and translation between the two cameras are by far the largest influence factor to the triangulation uncertainty. With a combined standard uncertainty of 5.9 μm, 6 μm and 14.8 μm for the x, y and z axes respectively, the contribution due to most of the properties is on the order of 5 μm, demonstrating the impact of the uncertainty on the camera rotation and distortion parameters. However, the rotation and distortion properties were only the main factors for the case of feature localisation uncertainties of 0.1 pixels. Figure 3.4 shows the effect that feature position uncertainty has on the combined standard uncertainty. Although the contribution is below 10 μm at 0.1 pixels, there is a linear increase up to around 35 μm for a feature positional uncertainty of around 1 pixel. Although in ideal circumstances, 0.1 pixels of uncertainty is obtainable, the vast number of contributions to the feature position uncertainty mean that, in reality, there will be a distribution of feature uncertainties within a measurement. The contrast of visible surface texture, focus and the feature detection algorithm used all have an impact on the feature uncertainty and depend on a range of internal and external factors, making the true value of feature position uncertainty difficult to quantity.

Although the rotational extrinsic properties were shown to be one of the main contributing factors in the combined standard uncertainty, it was also considered that in reality, the majority of the error contributions from the intrinsic and extrinsic factors would be systematic rather than random. As such, the effect of systematic

offsets to the focal length, translation, rotation and distortion factors were modelled in order to understand their effect on the triangulated point cloud. As can be seen in figures 3.4 to 3.8, the effects of systematic errors manifest as complex distortions to the triangulated point cloud, often being non-linear. Effectively, these distortions will result in length measurement being affected by both position and orientation within the measurement volume, being stretched and skewed in different axes. Although the values in table 3.2 demonstrate the effect of a random variation, they give some indication of the possible contribution of systematic offsets to the measurement uncertainty.

In addition to the spatial variation caused by systematic offsets, there is also a spatial variation to the combined measurement uncertainty for purely random influence factors. The nature of photogrammetry means that the uncertainty on a triangulated point will vary throughout the measurement volume, as shown in figure 3.9. Although the effect is relatively small, figure 3.9 shows that the combined uncertainty can vary by around 5 μm throughout the entire measurement volume.

3.4.2 Scaling factor results

Despite using an uncalibrated checkerboard artefact in order to provide the initial extrinsic parameters, the accuracy of the scale factor appears to be high, with an error of 0.0068% over the baseline length. Based on the linear regression of the length measurement data, the uncertainty on the scale factor was on the order of 7 μm over the entire 100 mm measurement volume. The interesting result from the stereo-photogrammetry comparison with the laser interferometer measurements is the shape of the residuals from the linear fit. As can be seen in figure 3.11, there is a repeatable trend to the error on the checkerboard position. There are a range of external factors that could have resulted in the trend of the residuals

in figure 3.11, however, systematic errors in the extrinsic and intrinsic properties are likely a substantial contributing factor. In fact, the maximum deviation of the length measurements was typically on the order of 5 μm or less for all repeated measurements. The high repeatability of the length measurements would suggest that the scale factor uncertainty can be reduced by compensating for the non-linear distortion of the measurement volume.

3.4.3 Gauge block measurement

Although the feature positional uncertainty is unknown for the gauge block measurements, the standard deviation from a plane for both the gauge block and platen surfaces agrees with the values predicted by the Monte Carlo simulations. Furthermore, the feature position uncertainty is expected to be much higher than for other methods due to the challenging surface properties, further suggesting that the extrinsic and intrinsic properties are likely systematic offsets, rather than randomly varying. Additionally, the error in the length measurement is somewhat higher than would be expected, based on the scale factor uncertainty. However, as can be seen in figure 3.11, non-linear distortions of the measurement volume could explain the 8 μm error in the gauge block measurement. In order to verify this, repeat measurements of the gauge block will be taken throughout the measurement volume.

3.5 Conclusion

This chapter presents the first attempt at an uncertainty analysis of a stereo-photogrammetry system, as well as a method for the traceable calibration of the photogrammetry scale factor. The outcome of this work is an estimate of the

expected measurement uncertainty of a stereo-photogrammetry system, as well as the identification of key influence factors that must be addressed in future work. Additionally, this work has also provided insight into the manifestation of characterisation uncertainty within a triangulation-based measurement system. Systematic errors in system properties lead to highly complex, non-linear effects in the resultant point cloud. In future work, the adjustment of systematic effects will be addressed as well as determining a methodology for calculating expected feature uncertainty. The future work that has developed from this work will be discussed in more detail in chapter 7.

Chapter 4

Single camera verification

4.1 Introduction to single camera verification

The existing specification standard for photogrammetry is VDI/VDE 2634 part 3 [114]. VDI/VDE 2634 part 3 has already been applied to larger scale photogrammetry systems, typically involving standard artefacts consisting of targets to act as points of correspondence [61, 114, 44]. When applying VDI/VDE 2634 part 3 to smaller scales with sub-millimetre features, the use of target detection methods becomes problematic. Manufacturing sub-millimetre targets is both expensive and complex, as well as the measurement being of the target location rather than the part geometry.

Photogrammetry methods for objects without targets are reliant on the process of feature detection and matching. Scale invariant feature transform (SIFT) algorithms are widely regarded as the most effective method of feature detection [65], and are based on the detection of local minima and maxima within a difference-of-Gaussian function. Detected features can then be matched by assigning unique descriptors based on local gradients and directions of the difference-of-Gaussian function [68]. In order for SIFT algorithms to detect any features, there must be

some variation within neighbouring pixels, which is observed as texture in the image, for this reason, objects with very little surface texture may not exhibit enough contrast for SIFT algorithms to detect features. Once the number of successfully detected features drops below some level, the estimation of the fundamental matrix between different perspectives will become inaccurate. As the initialisation of the photogrammetry self-calibration algorithm is based on the estimation of the fundamental matrix, poor feature detection will cause the calibration procedure to fail. Although this inability to detect objects with little texture is an intrinsic limitation of photogrammetry, it is particularly problematic when considering the verification of a photogrammetry system. As was discussed in section 2.7, verification artefacts are required to have surface height variation values significantly smaller than the anticipated measurement uncertainty. This means that for a photogrammetry system to be verified to a standard uncertainty of the order of a few micrometres, an artefact with surface height variations less than 1 μm is required.

Improving the effectiveness of photogrammetry based systems on surfaces with insufficient texture is already an established area of research. Koutsoudis et al. [57] have demonstrated that by projecting pseudo-random patterns onto an object during the imaging process, the density and accuracy of the resulting point-cloud is significantly increased. A similar method was also implemented by Siebert et al. [100] in which speckle patterns were projected onto human subjects to demonstrate the application of photogrammetry in medicine. The use of texture projection is not only used to improve spatial correspondence, in particular, by rapidly altering a speckle pattern produced by a laser and diffuser, Schaffer et al. were able to produce real-time reconstructions based on temporal matching algorithms [98].

Through the use of laser speckle projection, this chapter aims to provide a methodology that will allow the verification of photogrammetry systems to uncer-

tainties much lower than previously achieved. The methodology will also benefit from being easily implemented, without the need for any sophisticated or expensive equipment.

4.2 System design

The photogrammetry system can be seen in figure 4.1. The system consists of a simple rotating stage and camera mount that allows the desired number of images to be taken at a range of angles. The positions of the camera can also be altered in order to produce the required image magnification at a range of camera elevation angles. The imaging system itself consists of a commercial DSLR camera (Nikon D3300, 24 MP sensor) with a 60 mm macro lens to allow high-magnification images. The laser speckle system is mounted directly to the rotating table to ensure that the speckle pattern remains stationary with respect to the object as it rotates. Tests were also performed to ensure the projected pattern remained stable over one hour period, much longer than the time required for any particular experiment. Both the mean and standard deviation of all SIFT features were monitored for the length of the test relative to the first image. The mean motion of the pattern was determined by calculating the radial deviations of SIFT features in each image relative to the first. The mean motion was found to be around 3 pixels, and is due to the mechanical stability of the camera. For the duration of the test, the standard deviation of the mean motion was less then one pixel, corresponding to the relative motion of the speckle features on the object surface. Since the variation of the pattern is less than one pixel, we are confident that the pattern will remain stable for the duration of the measurements.

The laser speckle projection is achieved with the use of a laser diode (532 nm, 4.5 mW), focusing lens (50 mm, bi-convex) and glass diffuser (600 grit polished).

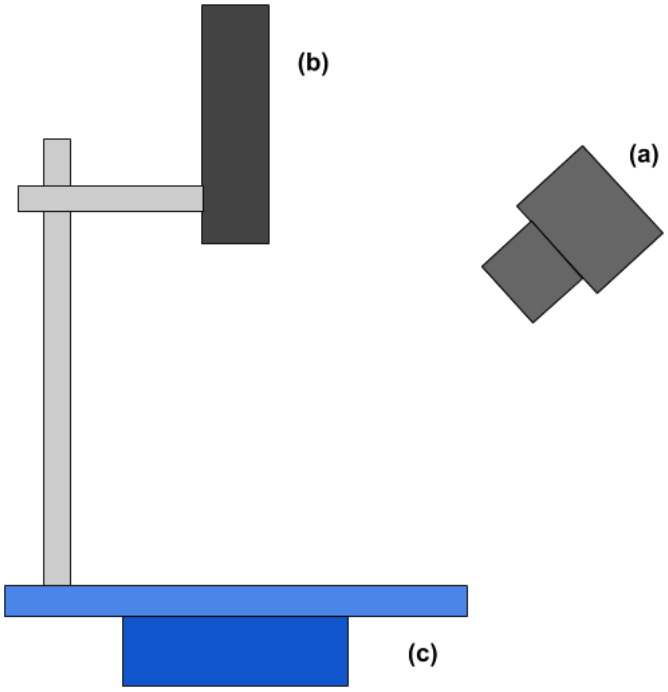

Fig. 4.1 Image of the photogrammetry system, consisting of a DSLR camera (a), laser speckle projector (b) and rotation stage (c).

The green laser diode was chosen to ensure the imaging system was most sensitive to intensity variations due to the Bayer filter and CMOS sensor design of the camera. The laser is then focused on to the glass diffuser by the focusing lens, as shown in figure 4.2. The interaction with the rough glass surface results in a complex, but structured interference pattern that can be projected onto the object surface [45]. As discussed in section 4.1, we have used the laser speckle pattern to provide artificial texture that can be detected and matched by SIFT algorithms. A significant requirement for the laser speckle system is that the object surface diffusely reflects the speckle pattern in order for the pattern to be observed on the objects surface. There will also be some further interaction of the laser speckle pattern with the object surface, creating "subjective speckle". Subjective speckle is an unwanted pattern as it will vary depending on the camera position and, therefore, will not produce corresponding features. However, by selecting a sufficiently low F-stop value (F/8), the contrast of the subjective speckle can be reduced to become effectively zero.

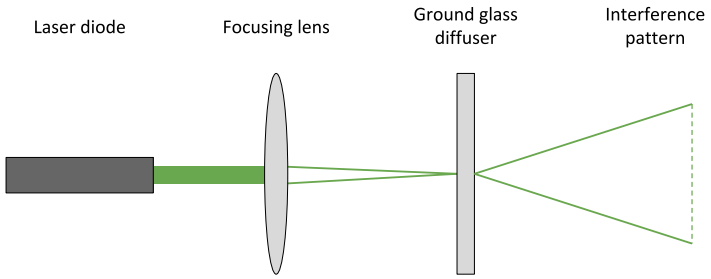

Fig. 4.2 Schematic design of the laser speckle projection system..

4.3 Artefacts

As we have seen in section 2.7, a sphere and ball bar are required for the verification of a photogrammetry system according to VDI/VDE 2634 part 3. Therefore, one

10 mm diameter and three 5 mm diameter tungsten carbide tooling balls were selected to construct the required artefacts [100]. The tungsten carbide tooling balls have a uncertainty on the radius of 0.2 μm and Ra of 0.25 μm whilst still having a diffusely reflecting surface ideal for photogrammetry. The 10 mm sphere was used as the probing error measurement sphere and placed in a object holder for individual use. The three 5 mm spheres were used to construct a ball plate, the design of which can be seen in figure 4.3. The triangular orientation of spheres in figure 4.3 was chosen such that three individual ball bar lengths could be measured from a single measurement. The ball bar lengths were calibrated using a Ziess F25 CMM with a maximum permissible error of 0.25 μm + L/666 μm, where L is the length of the ball bar. After calibration, the 6 mm, 8 mm and 10 mm lengths were found to be 5.942 mm, 7.956 mm and 9.957 mm respectively.

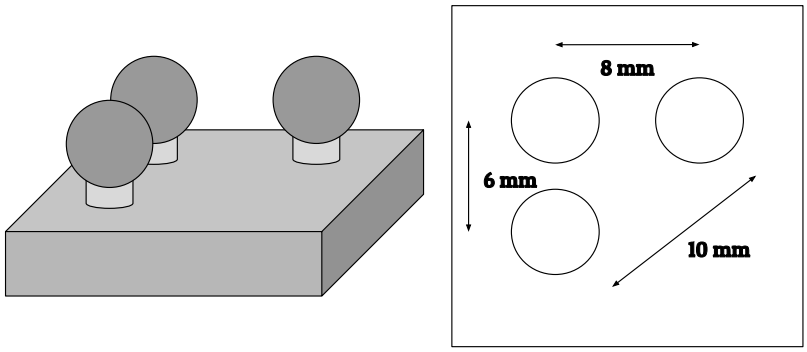

Fig. 4.3 Ball plate design, comprising of three spheres on the corners of a right-angled triangle. This provides three individual ball bar lengths of approximately 6 mm, 8 mm and 10 mm.

4.4 Modified tests

The probing form and size error tests can be performed exactly as described in VDI/VDE 2634 part 3. However, replicating the ball bar arrangements in figure 2.17 proves problematic when including the laser speckle projection system. As can

be seen in figure 4.2, the laser speckle projection system is placed directly above the object to provide optimal coverage of the object's surface. Due to the design of the system, it is not possible to project the speckle pattern onto two spheres when they are vertically aligned. Due to the limiting effect of projecting texture from above, vertical ball bar arrangements such placement one in figure 2.17 are unable to be measured. In order to compensate for this missing position, an additional tilted measurement was taken to give the ball plate orientations shown in figure 4.4.

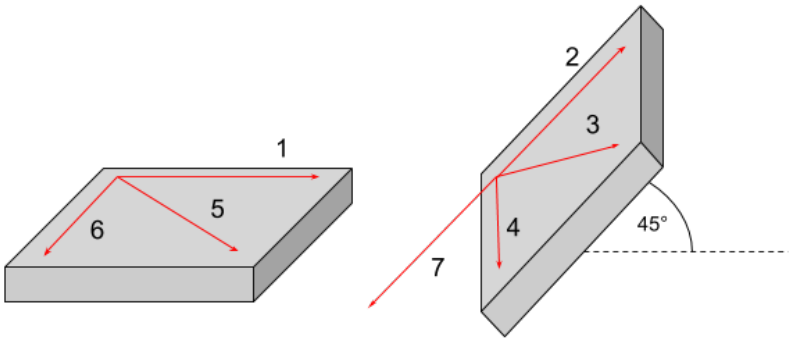

Fig. 4.4 Ball bar plate orientations, as used in the verification tests. Each arrow represents the angular orientation of the plate edge parallel to arrow 1.

Modifications to the evaluation process were also made in order to better agree with other CMM specification standards. ISO 10360 part 8 [52] outlines some acceptance tests for CMMs with optical distance sensors, many of which are similar to those in VDI/VDE 2634 part 3. According to ISO 10360 part 8, each test will be repeated three times in order to provide more data sets for the evaluation of the system. VDI/VDE 2634 part 3 also provides some basic methods for the evaluation of quality parameters. An appropriate method of uncertainty evaluation is outlined by ISO 15530 part 3, suitable for photogrammetry applications [32]. ISO 15530 part 3 describes uncertainty evaluation for a CMM using a calibrated workpiece. As photogrammetry requires some calibrated length to scale a reconstruction, ISO

15530 part 3 provides an ideal method for uncertainty evaluation. ISO 15530 part 3 defines the expanded uncertainty by

$$U = k\sqrt{u_{cal}^2 + u_p^2 + u_b^2 + u_w^2} \tag{4.1}$$

where k is the coverage factor ($k = 2$ for a 95% confidence interval), u_{cal} is the standard uncertainty of the calibrated workpiece, u_p is the standard uncertainty of the measurement being made, u_b is the standard uncertainty of the systematic errors in the measurement process and u_w is the standard uncertainty associated with material and manufacturing variations between the object being measured and calibrated workpiece. As the reconstructions are entirely scaled using the calibrated workpiece, u_b will be always be zero. Similarly, as the calibrated workpieces and measurement objects have been manufactured in the same way with the same materials, u_w is also assumed to be zero. The expanded uncertainty can then be evaluated using the standard uncertainty of the measured parameter and the standard uncertainty of the workpiece used to scale the reconstruction.

4.5 Results

This section describes the process of obtaining and evaluating the data for the verification tests described in section 4.4. Each test was performed three times by taking thirty images through 180° of rotation. Once the images had been taken, the reconstruction was performed using commercial photogrammetry software (Agisoft PhotoScan) to produce a dense point cloud of the object [2]. The dense point cloud was then exported from the software for analysis and measurements to be made. All measurements were performed under the same conditions, with temperature variations ($\pm$ 0.5 $^{\circ}$C) being sufficiently small to have no significant

effect on measurements [9]. As the ball bar plate is manufactured from mild steel, a 0.5 $^{\circ C}$) variation in temperature would only result in a length variation of $\pm$ 0.16 μm. The procedure for repeat measurements was to reset the entire system and alter the speckle pattern such that a different pattern is observed on the object surface.

4.5.1 Sphere form and sizing error

The sphere form and sizing error test was performed in agreement with the tests described in Section 2.4. The 10 mm sphere was used as the main sphere for measurement, with the camera placed in five arbitrary positions and each measurement repeated three times. The camera positions were chosen in order to produce approximately the same magnification and elevation. In order to provide a length to scale the reconstruction, the ball plate was placed in close proximity to provide two additional spheres within the reconstruction volume. The calibrated radii of the two ball plate spheres could then be used to accurately scale the main sphere. A magnification of 1:3 was chosen to ensure that all spheres are in focus for the majority of the measurement, whilst maximising the resolution of the main sphere. An elevation of approximately 45° was also chosen to provide the best coverage of the sphere surface. Once all images had been captured, each was reconstructed using commercial photogrammetry software (Agisoft PhotoScan) and each spheres point cloud exported individually [2].

The point cloud data was then analysed by fitting each sphere with a least-squares regression, according to

$$(x_i - a)^2 + (y_i - b)^2 + (z_i - b)^2 = r^2 \tag{4.2}$$

where $[x_i, y_i, z_i]$ is the i^{th} entry of N coordinates, $[a, b, c]$ is the sphere centre and r is the sphere radius. The parameters of equation 4.2 are solved through the simple linear relation

$$A \begin{bmatrix} a \\ b \\ c \\ d \end{bmatrix} = 0 \tag{4.3}$$

where A is defined as

$$A = \begin{bmatrix} x_1 & y_1 & z_1 & 1 \\ x_2 & y_2 & z_2 & 1 \\ \vdots & \vdots & \vdots & \vdots \\ x_N & y_N & z_N & 1 \end{bmatrix} = e, \tag{4.4}$$

e is defined as

$$e = \begin{bmatrix} -(x_1^2 + y_1^2 + z_1^2) \\ -(x_2^2 + y_2^2 + z_2^2) \\ \vdots \\ -(x_N^2 + y_N^2 + z_N^2) \end{bmatrix} \tag{4.5}$$

and $r = \sqrt{a^2 + b^2 + c^2 - d}$. Once equation 4.3 has been solved, the radial error, Δr_i, of each point can be calculated from

$$\Delta r_i = \sqrt{(x_i - a)^2 + (y_i - b)^2 + (z_i - c)^2} - r. \tag{4.6}$$

The sphere fit is then further refined according to the ISO 10360 part 8 standard by removing 5 % of points with the greatest radial errors, according to equation 4.6. With the refined data, the sphere fitting process is repeated to give a final fitted radius r and the radial errors for the refined points Δr. The fitted radius r and the

radial errors Δr can then be scaled using the fitted radii of the two 5 mm spheres. Table 4.1 shows the fitted radius and standard deviation of the radial errors for all measurements. Table 4.1 also shows the mean value of all the fitted radii as well as its associated standard deviation.

As can be seen in table 4.1, the system was able to produce a point cloud with a form standard uncertainty of around 8.3 μm and a sizing standard uncertainty of 4 μm on a sphere of radius 4.999 mm. The expanded uncertainty of the sizing error can then be calculated from equation 4.1 to give 8 μm with a coverage factor of two, according to the ISO 10360 part 8 standard. Similarly, the form errors give a mean expanded uncertainty of 17 μm with a coverage factor of two. As two 5 mm spheres were used as the calibrated workpiece, the radius uncertainty of the 5 mm spheres was used as the standard uncertainty on the calibrated workpiece.

Table 4.1 Sphere form and sizing errors

Camera Position	**Fitted radius, r /mm**			**Standard deviation of Δr / μm**		
A	4.993	5.003	5.001	7.8	8.3	7.6
B	5.003	5.007	4.998	8.9	8.5	8.4
C	5.006	5.006	5.001	7.6	8.5	8.3
D	5.000	5.000	4.998	7.6	7.1	8.3
E	5.005	4.996	5.007	9.4	8.1	10.7
Mean		5.001			8.3	
Standard deviation / μm		4				

4.5.2 Sphere spacing error

Using the ball plate described in section 4.3, the sphere spacing error test was performed as described in section 4.4. All orientations shown in figure 4.4 were measured three times, for all three lengths. As in section 4.5, the camera was placed in order to produce a magnification of 1:3 such that all three spheres were in focus for the majority of the measurement. Unlike the previous section, the camera was

placed at a slightly higher elevation in order to ensure the camera depth of field more evenly covered the ball plate surface.

Again, once all measurements had been taken and reconstructed, all three spheres were fitted using the same process outlined in section 4.5.1. The sphere spacing lengths were then calculated according to

$$L_{r,1} = \sqrt{(a_1 - a_2)^2 + (b_1 - b_2)^2 + (c_1 - c_2)^2}, \tag{4.7}$$

$$L_{r,1} = \sqrt{(a_2 - a_3)^2 + (b_2 - b_3)^2 + (c_2 - c_3)^2}, \tag{4.8}$$

$$L_{r,1} = \sqrt{(a_3 - a_1)^2 + (b_3 - b_1)^2 + (c_3 - c_1)^2} \tag{4.9}$$

where $L_{r,i}$ is the recontruction length i and $[a_i, b_i, c_i]$ are the coordinates for the centree of sphere i. For each length, the metric value can then be calculated from

$$L_{m,1} = L_{r,1}(L_{c,3}/L_{r,3}), \tag{4.10}$$

$$L_{m,2} = L_{r,2}(L_{c,3}/L_{r,3}), \tag{4.11}$$

$$L_{m,3} = 0.5L_{r,3}((L_{c,1}/L_{r,1}) + (L_{c,2}/L_{r,2})) \tag{4.12}$$

where $L_{m,i}$ and $L_{c,i}$ are the metric measurement and calibrated value of length i, respectively. Using this method, the test was performed for all lengths, three times in all seven positions. The measured lengths for the sphere spacing error can be seen in table 4.2 along with the mean of each length, the difference from the calibrated value and the standard deviation on the mean.

Table 4.2 shows that the system was able to measure lengths between 6 mm and 10 mm, to a standard uncertainty of around 10 μm to 12 μm. Based on the maximum permissible error of the sphere spacing calibrations of 0.25 μm, the

Table 4.2 Sphere spacing errors

Position	$L_{m,1}$ /mm			$L_{m,2}$ /mm			$L_{m,3}$ /mm		
1	5.937	5.943	5.946	7.953	7.961	7.964	9.964	9.954	9.949
2	5.917	5.941	5.914	7.960	7.956	7.974	9.977	9.959	9.970
3	5.928	5.938	5.924	7.946	7.971	7.953	9.976	9.952	9.975
4	5.941	5.953	5.936	7.920	7.925	7.957	9.982	9.968	9.962
5	5.952	5.942	5.945	7.952	7.957	7.955	9.952	9.957	9.956
6	5.947	5.950	5.943	7.962	7.959	7.956	9.950	9.949	9.957
7	5.970	5.943	5.934	7.956	7.956	7.946	9.960	9.957	9.971
Mean /mm		5.939			7.954			10.037	
$L_{m,i} - L_{c,i}$ / μm		-3.3			-3.0			4.6	
Uncertianty / μm		13			13			10	

expanded uncertainty on the sphere spacing measurements with a coverage factor of two are 25 μm, 25 μm and 20 μm for the 6 mm, 8 mm and 10 mm lengths respectively, as seen in table 4.2.

4.6 Conclusion

In this chapter, a laser speckle projection system has been used to provide observable texture on the surface of smooth verification artefacts that would otherwise appear featureless. Using the laser speckle, acceptance tests modified from the specification standards VDI/VDE 2634 part 3 were performed on a set of verification artefacts with surface height variations less than 1 μm. With such low surface height variations on the verification artefact, the measurement uncertainty can potentially be evaluated to uncertainties on the order of a micrometre. The sizing, form and sphere to sphere length measurement expanded uncertainties of the photogrammetry system under test were found to be 8 μm, 17 μm and 25 μm over a 95 % confidence interval, respectively.

In conclusion, this chapter has demonstrated a technique for the evaluation of photogrammetry measurement uncertainties on the order of a micrometre. Given the expanded uncertainties achieved by the photogrammetry system under test, this will provide a standard verification method for further advancements in micro-scale photogrammetry technology. In order to develop this methodology as a potential extension to the VDI/VDE standard, further work will also be done on better characterising the effect of laser speckle for texture projection.

Chapter 5

Stereo-camera verification

5.1 Introduction

This chapter aims to apply the VDI/VDE 2634 part 2 standards (discussed in section 2.7.1) to the stereo photogrammetry system discussed in chapter 3 in order to verify the performance of the system. Unlike the DSLR camera used in chapter 4, the cameras used in this chapter are machine vision cameras (Basler Ace acA4024-29um) with a 12 MP sensor and a pixel pitch of 1.85 μm. As DSLR cameras have a mechanical shutter, they produce significant vibration during the imaging process. Therefore, the use of machine vision cameras is required in order to achieve the high accuracy characterisation of the extrinsic properties of the stereo-camera set-up. Unfortunately, the small pixel size of the machine vision cameras compared to the DSLR makes the application of the laser speckle used in chapter 4 problematic. As discussed in section 4.2, the F-stop value for the DSLR camera could be set sufficiently low in order to average out the subjective speckle effect. However, with the machine vision camera, the small pixel pitch and sensor size make limiting the F-stop values unsuitable. The F-stop required to suitably reduce the subjective speckle effect is too low to provide a sufficient depth of field for the required

measurement volume (100 mm $\times$ 100 mm $\times$ 100 mm). The inability to use laser speckle for texture projection makes the measurement of featureless, calibrated objects difficult with the stereo-photogrammetry system described in chapter 3.

In order to produce correspondence of the verification artefacts, fringe projection based methods can instead be applied instead of laser speckle texture projection. For this chapter, temporal methods were utilised due to the independence of each pixel from its neighbours. The exact method of phase calculation will be discussed in detail in section 5.2.3. Once the phase of each camera pixel is calculated, it can then be related back to a particular horizontal pixel coordinate u_p within the projector. The epipolar geometry constraint between the camera and projector discussed in section 2.3.3, can then be used in order to determine the vertical projector pixel coordinate v_p after which the three-dimensional coordinates of the point can be calculated.

This method of finding correspondence between the projector and camera makes the point-to-point uncertainty between correspondences much more consistent than photogrammetry methods. This improved consistency in correspondence is why the accuracy of a fringe projection measurement is typically better than photogrammetry systems with similar measurement volumes [15]. Although this assertion does not hold true for a range of materials and geometries, it is certainly the case for diffusely reflecting calibrated artefacts. As discussed in chapter 3, the uncertainty of any one particular image feature lies on some unknown distribution and is the result of a multitude of factors. However, by finding correspondence between camera images using encoded phase, the influence of feature uncertainty can be greatly reduced, or at the very least made more consistent. Rather than having a distribution of point uncertainties, the phase encoding of the image pixels allows the measurement uncertainty of the stereo-photogrammetry to be

evaluated in optimal conditions. This separation of measurement uncertainty from system characterisation and from the feature matching process allows for a better understanding of the contributions to the uncertainty in stereo-photogrammetry measurement. A better understanding of the uncertainty contributions allows for the identification of key areas for improvement and informs the development process.

In this chapter, a method for the verification of a stereo-photogrammetry system is demonstrated in which a low-cost projector is utilised to provide correspondence. The verification method differs from that in chapter 4 as it is more suitable for cameras with smaller sensor dimensions and for systems based on stereo-photogrammetry principles. This chapter is also a continuation of chapter 3 in which a stereo-photogrammetry system was modelled in order provide theoretical estimations of the uncertainty on form measurements.

5.2 Methodology

5.2.1 Verification tests

The verification tests described in section 2.7.1 can be applied directly to the stereo-photogrammetry system used in chapter 3. According to the VDI/VDE 2634 part 2 standard, a 50 mm long ball bar, a 20 mm diameter sphere and a calibrated flat were all selected as appropriate for the verification test. Although the 50 mm ball bar may be slightly less than 0.3 of the longest diagonal length of the measurement volume, VDI/VDE 2634 part 2 does specify that alternative lengths may be used if required, provided that the length is provided. Given the expanded uncertainties for form measurements in chapter 3, the requirement for the calibration uncertainty should be at substantially less than 5.9 μm. The calibration data shows that the ball

bar length is 49.944 mm ± 0.81 μm (k=2), the sphere has a diameter of 20.001 mm + 1.02 μm/− 0.63 μm (k=2) and the maximum deviation of the calibrated flat from a fitted plane is ± 2.6 μm (k=2). Using the ball bar, sphere and flatness artefacts, the measurements described in section 2.7.1 were all made with the stereo photogrammetry system using phase values to find corresponding pixels.

5.2.2 Fringe projection

Fringe projection methods are in principle similar to stereo-photogrammetry and are based on the triangulation of common points between projectors and cameras. Effectively, one camera within the stereo pair is replaced with a projector and the correspondence is now determined by the properties of the projected light [46]. The method by which the correspondence is evaluated varies, but can be generally dived in discrete and continuous techniques. There is wide range of discrete techniques including De Bruijn sequences [8, 41, 96], M-array techniques [29] and binary encoding and Gray encoding [89]. Although discrete methods have been shown to be effective, the scope of this work will mainly focus on continuous methods.

Continuous methods encode the pixel position within the projector through the phase of a sinusoidal signal . The relationship of the horizontal phase ϕ to the pixel position is described by

$$\phi(u_p, v_p) = u_p \ (2\pi/T) \tag{5.1}$$

where $\phi(u_p, v_p)$ is the phase of the signal at the pixel position (u_p, v_p) within the projector and T is the period of the signal in pixels [46]. There are a range of methods by which the phase of the projector pixel can be captured by the camera and is typically grouped into spatial and temporal methods. Spatial methods are typically faster, but requires a continuous surface as it cannot handle discontinuities

[128]. Temporal methods instead encode phase through a series of images such as heterodyne frequency phase stepping methods [92] and phase stepping with discrete fringe order encoding [89].

5.2.3 Phase extraction

The method of phase encoding used in this work is based on the projection of a sinusoidal pattern at a number of different phase steps. At least three different offsets are applied to the sinusoidal pattern and an image is captured at each step. The captured image is described by

$$I(u,v,k) = I'(u,v) + I''(u,v)cos[\phi(u,v) + \delta(k)] \tag{5.2}$$

where $I(u,v,k)$ is the pixel intensity captured at camera pixel (u,v) at phase offset k, $I'(u,v)$ is the average pixel intensity, $I''(u,v)$ is the intensity modulation of the projected light, $\phi(u,v)$ is the phase of the camera pixel and $\delta(k)$ is the phase offset. The phase value ϕ for any particular pixel can then be retrieved by capturing N images with phase steps distributed between $-\pi$ and $+\pi$ by the equation

$$\phi(u,v) = -tan^{-1}\left(\frac{\sum_{k=1}^{N} I(u,v,k)sin[\delta(k)]}{\sum_{k=1}^{N} I(u,v,k)cos[\delta(k)]}\right). \tag{5.3}$$

As can be seen in equation 5.3, the inverse tangent function results in a 2π modulation of the calculated phase. This 2π modulated phase data is referred to as the wrapped phase and must be unwrapped by applying a fringe order correction by which multiples of 2π are added. The effect of 2π modulation can be seen in figure 5.1. Various methods of unwrapping exist, however, for simplicity a binary encoded pattern was instead projected in which the fringe order map k_{map} is converted to binary values and projected onto the artefact. The globally unwrapped phase map

Φ, can then be calculated through

$$\Phi = \phi + (2\pi k_{map}). \tag{5.4}$$

Although conventional decimal to binary vector conversion could encode the fringe order of each pixel, a further improvement was implemented by instead encoding the fringe order in Gray code. As can be seen in figure 5.2, binary and Gray code have a different structure. The rows in figure 5.2 correspond to the values 0 to 127, with the columns representing each bit of the converted decimal value. As can also be seen in figure 5.2, Gray code benefits from the different structure as ambiguity in the final bit will only lead to errors of 1, whereas binary code leads to random jumps in the decimal value. Gray code, therefore, allows for a simple search for 2π jumps in the phase map with respect to neighbouring pixels, allowing an additional correction to be made.

5.2.4 Disparity map calculation

Rather than directly triangulating corresponding features, the rectification of the stereo images and the calculation of a disparity map is more efficient for the triangulation of a large number of points. The first stage of the disparity map calculation process is the rectification of the stereo images, in which a transformation is applied to the images in order to project them onto the same plane. A physical representation of the rectification process is shown in figure 5.3 and demonstrates that image rectification effectively transforms each image such that epipolar lines (shown in a dotted line in figure 5.3 (c)) are parallel. Effectively, a point from an object shown in figure 5.3 (a) is projected onto the left image 5.3 (b) which is then transformed into the rectified image.

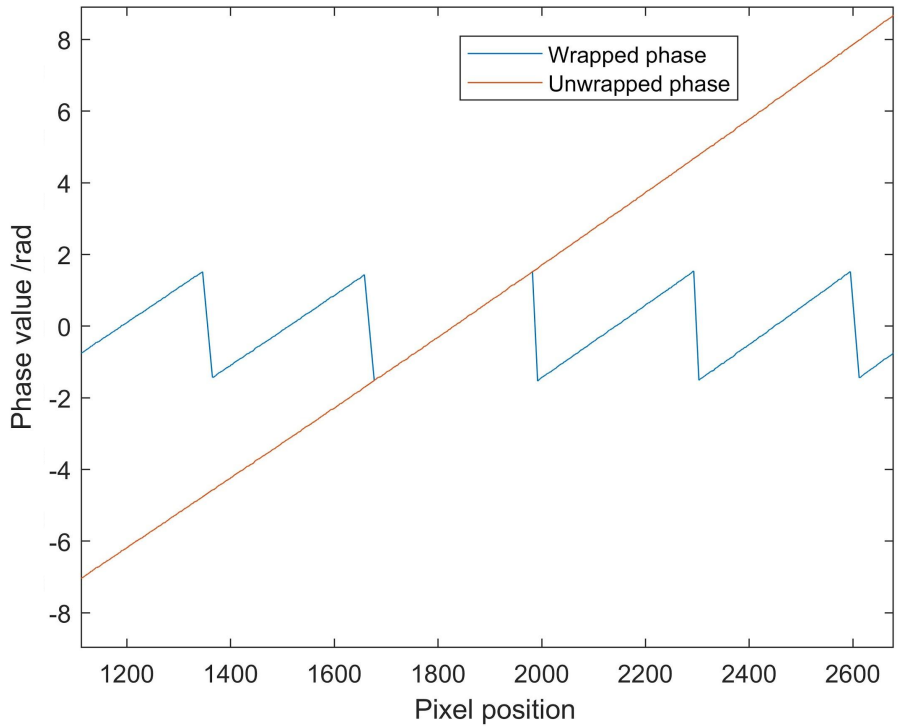

Fig. 5.1 Comparison between wrapped and unwrapped phase maps.

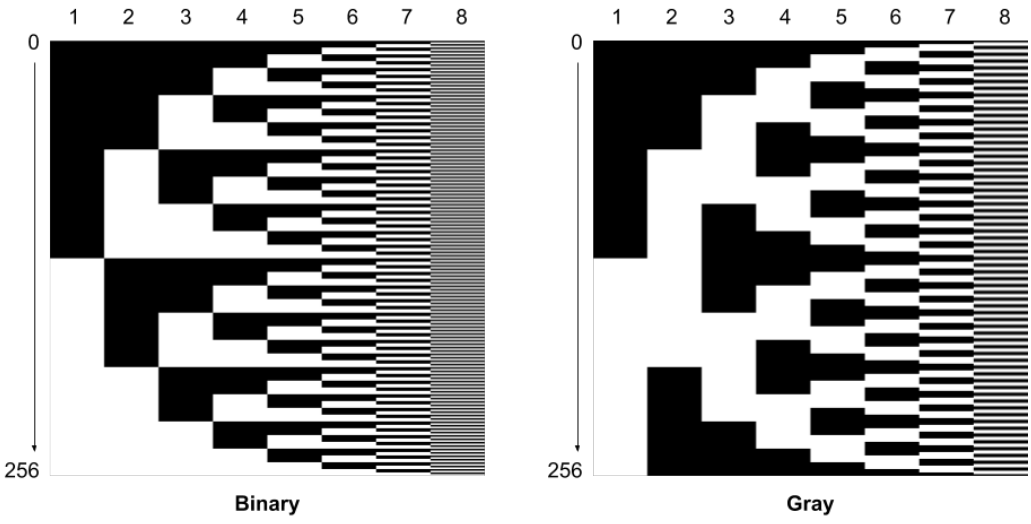

Fig. 5.2 8-bit encode binary and Gray code in which rows correspond to 0 to 128 and columns represent each bit.

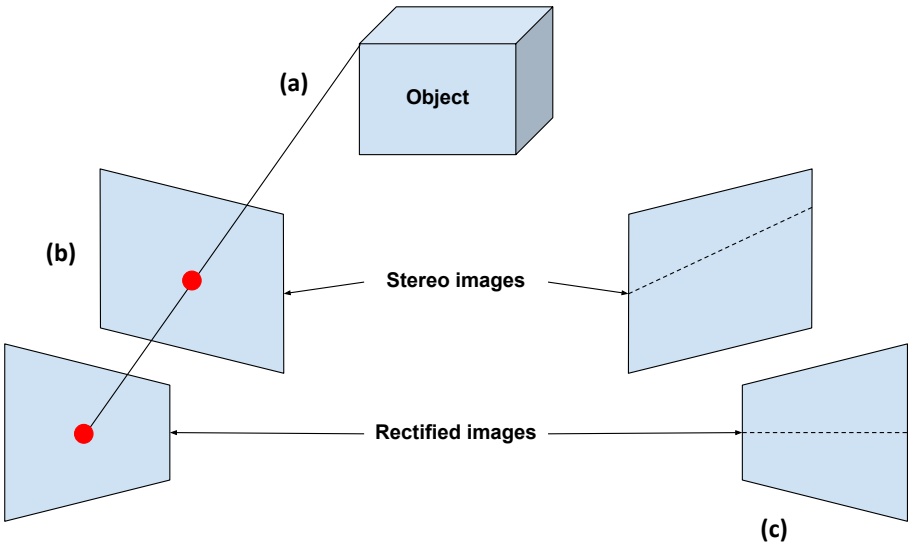

Fig. 5.3 Image rectification principle.

The benefit of the rectification process is that the search for correspondences is limited to a single line. By extracting the same line from both rectified unwrapped phase images, the search for correspondences is simply achieved by finding points at which the phase value matches. A slice of phase values for each rectified phase map can be seen in figure 5.4 in which the distance between the corresponding phases in the left and right images is the disparity value.

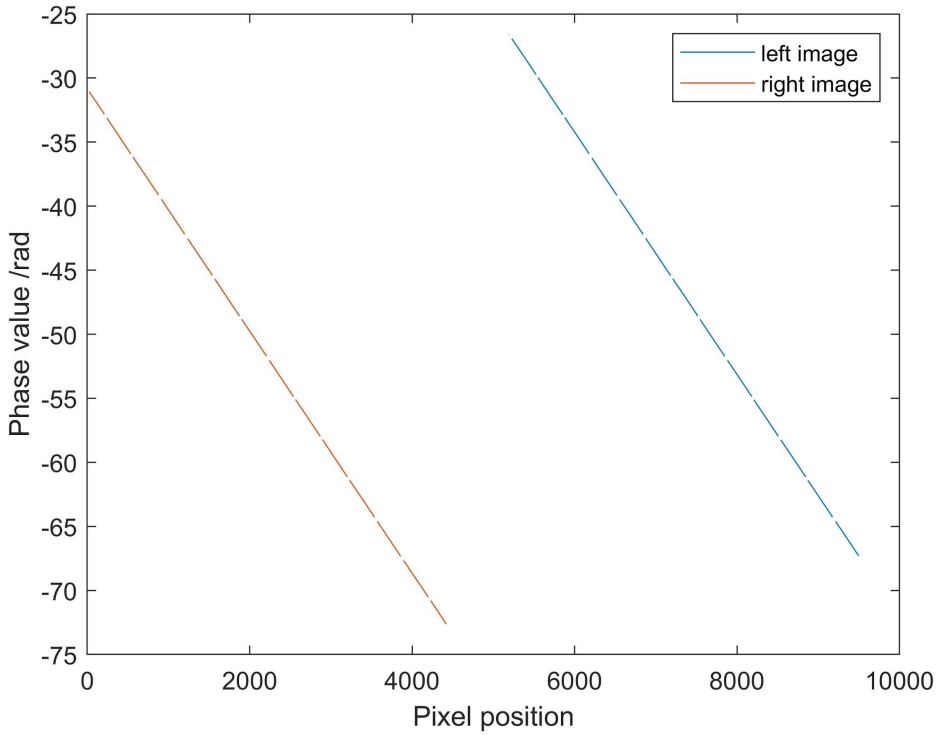

Fig. 5.4 Slice of each rectified phase map demonstrating the disparity offset between images.

The generation of the disparity map is achieved by iteratively taking each phase value in the left image and comparing it with the corresponding slice of the right image. The absolute difference of the right image slice phase and a single pixel in the left image is shown in figure 5.5. By extracting the two lowest phase differences from the line shown in figure 5.5, a linear fit between the two points can

be determined, giving a sub-pixel level disparity value between the left and right image. The disparity map can then be used to generate point clouds for analysis.

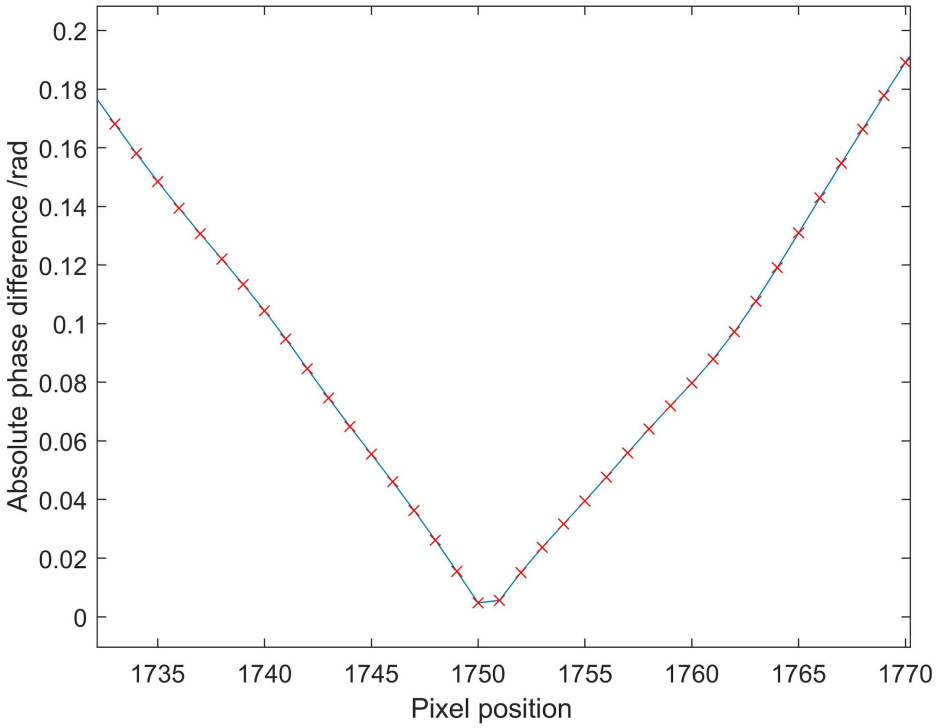

Fig. 5.5 Evaluation of disparity through the sub-pixel localisation of the zero crossing.

5.3 Results

The results for the sphere measurements can be seen in table 5.1. The 20 mm sphere was measured in the ten positions shown in figure 2.16 and a least-squares sphere fit was applied to each point cloud. The sphere fitting process was performed iteratively, removing the point with the maximum radial deviation until three points per 1000 of the original data were removed. The fitted sphere radius and maximum radial deviation from the nominal radius were taken and is shown in table 5.1. The mean sphere diameter was found to be 19.993 mm $\pm$ 123 μm with

a maximum deviation from the calibrated value of 146 μm. The maximum form deviation of all the sphere measurements was also found to be 0.106 mm.

Table 5.1 Sphere fitted radii, maximum radial deviations and radial standard deviations

Sphere position	**Fitted diameter /mm**	**Difference from calibration /μm**	**Maximum radial deviation /μm**	**Standard deviation /μm**
1	20.026	25	69	22
2	19.781	-22	80	24
3	20.109	108	77	19
4	19.978	-23	11	26
5	19.902	-99	102	30
6	20.144	143	67	20
7	19.855	-146	75	20
8	20.071	70	77	22
9	20.120	119	75	27
10	19.940	-61	106	29
Mean	19.993	-8		

Similar to the sphere measurements, the ball bar was measured in the orientations specified by the VDI/VDE 2634 part 2 standard, and is shown in figure 2.17. The points corresponding to each sphere were then separated and the same least-squares fitting protocol as used for the sphere measurements was applied.Once the worst three in every 1000 points was removed from each sphere, according to the VDI/VDE 2634 part 2 standard, the fitted sphere centre for each sphere was taken. The geometric distance between the sphere was then calculated for each position and can be seen in table 5.2. The average ball bar length was found to be 49.986 mm $\pm$ 36 μm with a maximum deviation from the calibrated value of 97 μm.

Finally, the calibrated plane was measured in the positions shown in figure 2.18 according to the VDI/VDE 2634 part 2 standard. The central flat section was then extracted from the point cloud and a plane was fit to the point cloud using a least-squares algorithm. Again, an iterative approach to the fitting is applied in order to remove the worst three points per 1000. The maximum deviation from the

Table 5.2 Sphere to sphere distance measurements

Ball bar orientation	Sphere to sphere distance /mm	Deviation from calibration /μm
1	49.969	25
2	49.982	38
3	49.982	38
4	49.934	-10
5	49.969	25
6	50.041	97
7	50.025	81
Mean	49.986	42

fitted plane was then taken and is shown in table 5.3, in which the highest recorded value was 0.236 mm.

Table 5.3 Flatness maximum deviations and standard deviations

Flat position	Maximum deviation from flat /μm	Standard deviation from flat /μm
1	144	58
2	138	51
3	236	99
4	140	47
5	105	35
6	77	22

5.4 Discussion

5.4.1 System measurement uncertainty

According to the VDI/VDE 2634 part 2 standards, the acceptance tests are successful if the required maximum permissible error is not passed by any of the measurement results. Based on the acceptance test requirements, the maximum permissible error for the sphere form, sphere size, length measurement and flatness are 186 μm, 143 μm, 96 μm and 243 μm, respectively. Although these maximum errors are

substantially higher than the expanded measurement uncertainties predicted in chapter 3, the standard deviations of the sphere form and flatness measurements do correspond to measurement uncertainties for feature location uncertainties on the order of 1 pixel. As the feature location uncertainty is unknown, it is difficult to ascertain how accurate the uncertainty model is, but the relatively close agreement does suggest the model is somewhat accurate.

5.4.2 Systematic effects

As section 3.3.1 in chapter 3 suggests, there are expected to be some systematic errors in the characterisation of the stereo-photogrammetry system that will manifest in the measurement data. As systematic errors will effectively result in non-linear offsets in the measurement volume, this can be effectively thought of as variations in the local scale factor throughout the measurement volume. This will manifest as slight scale differences in the sphere measurements depending on the sphere position within the measurement volume, as well as a distortion of the apparent length of ball bars. This effect can be seen in the sphere size measurement data with consistent decreases in sphere radius from position 1 to 2, 4 to 5, 6 to 7 and 9 to 10, all corresponding to shifts from the right side to the left side of the measurement volume. The effect is also demonstrated by the lower errors in the length measurement errors compared to the sphere size errors. As the ball bar length is larger than the sphere diameter, it will effectively average over a larger range of scale factor variations than the single sphere. This leads to a scenario in which the length measurement error decreases with longer lengths as the local variations in the scale factor are averaged until the global scale factor uncertainty is reached. This local scale factor also accounts for the substantially larger standard

deviation in the sphere sizes and length measurements compared to the standard deviation on the sphere form.

5.4.3 Correspondence

As can be seen in table 5.3, the flatness maximum errors and standard deviations are both substantially higher than the sphere form standard deviations and ball bar length measurement errors. The reason for this can be seen in figure 5.6 in the structured pattern to the deviations from a plane. Through repeat measurements made to produce this data and refine the process, it was found that the magnitude and spatial frequency of this deviation becomes lower when the characterisation of the stereo-photogrammetry parameters is more accurate. As such, this dependence of the structured deviations on the characterised system parameters suggests some complex relationship with the calibration accuracy and the correspondence method proposed in this chapter. A strength of this method is that non-linearities in the projector intensity should be heavily reduced as the same cameras with the same settings are used. Effectively, both cameras should always "see" the same phase for the same point, regardless of the non-linear response of the projector. However, this is only true in the case of a perfectly calibrated system. As the correspondence method used relies on epipolar geometry to refine the phase matching search to a single line, the accuracy of the characterisation will determine the effectiveness of the matching process. Any offset in the stereo-camera parameters will result in a slightly different search line that will effectively destroy the robustness of the system to non-linearities.

Although the correspondence method outlined in this chapter generates its own systematic errors, it does provide an interesting potential to quantify the "accuracy" of the system under test. Rather than relying on the time consuming

process of repeat measurements, a non-linearity could be induced in the projector resulting in magnified flatness deviations. The effect of systematic offsets in the stereo-photogrammetry measurements would effectively be magnified allowing for a much finer evaluation accuracy than other methods. Potentially, through the measurement of planes in multiple orientations, this method could also allow for a more accurate characterisation of the stereo-photogrammetry system.

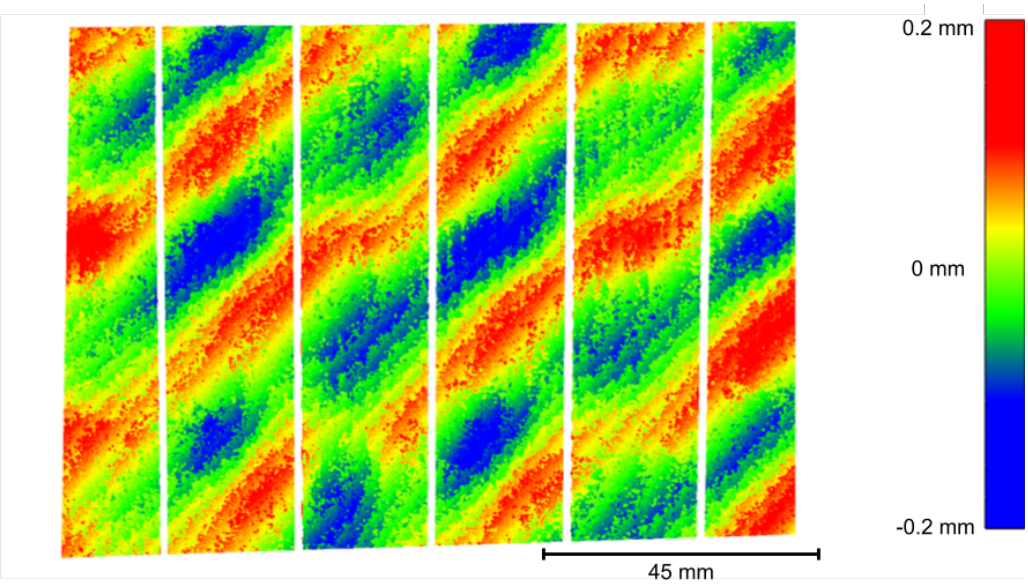

Fig. 5.6 Flatness measurement deviation from a plane in position 1.

5.5 Conclusion

Through the use of a low-cost projector to provide correspondence between cameras, a methodology has been presented that allows for the VDI/VDE 2634 part 2 acceptance tests to be performed on a stereo-photogrammetry system. The methodology is particularly suited to systems composed of cameras with small sensor sizes, making the use of laser speckle texture projection unsuitable. The methodology was then applied to the stereo-photogrammetry system modelled in chapter 3 and the measurement results compared with the results from the uncertainty modelling

results of this chapter. The theoretical and experimental measurement uncertainties were generally in agreement, with variations being explained by the anticipated effects of systematic offsets in the system parameters. Although the phase correspondence method was successful on measurements with a small area, such as with the spheres, a low spatial frequency variation in the measurements was seen on large flat surfaces. The variability of the low spatial frequency variations was shown to be dependant on calibration accuracy, and as such, is likely to the be the result of a magnification of errors caused by non-linearities in the projector. Although this low spatial frequency error likely results in an increase in the measurement errors, it does provide a strong indicator of measurement accuracy. In future work, the exact nature of the low spatial frequency variation will be further investigated and its use as a novel calibration metric will be tested.

Chapter 6

Case studies

In this chapter, several case studies are presented that were aided by the knowledge and systems developed through the work performed in chapters 3 to 5. The work ranges from the data fusion of photogrammetry with additional measurement technologies to the applications of laser speckle texture projection.

6.1 Fusion of photogrammetry and CSI data

6.1.1 Introduction to fusion of photogrammetry and CSI data

Multisensor data fusion is a promising approach to enlarge the spatial bandwidth of measuring techniques and improve accuracy, taking advantage of the strengths of different techniques. The 2009 CIRP Keynote [119] provides excellent insight into the use of multisensor data fusion for dimensional metrology in order to get holistic, more accurate and complete information about a workpiece based on measurement from one or more sensors, data processing and modelling of the measurement procedure. Different data types can be integrated in dimensional geometry. Generally, data types are indexed as homogeneous integration when

combining the same type of data (e.g. 3D point clouds), while inhomogeneous integration is required in all other cases. Different methods have been developed for the fusion of information from different sensors. A two-stage multisensor data fusion model (Gaussian model) is presented by Colosimo et al. [19]. Fringe projection data (high density points but low accuracy) are fused with a smaller set of data acquired with a touch-probe coordinate measuring machine (CMM) (lower point density but higher accuracy). The Gaussian process model is built using the high-density dataset, then the two datasets (homogeneous data sets) are linked through a linkage model. In reference [126], the Gaussian process method for measurement of complex geometries is presented and the validity and application of the method is evaluated. Moreover, the same approach is applied by Chen [16]; changing the systems and using artificial datasets (fusion of point scanning laser scanning microscopy and atomic force microscopy). Different methods, based on weighted fusion functions, are described elsewhere [116]. All the previously described methods only work effectively for homogeneous datasets.

Ramasamy [90] compared different data fusion algorithms for coherence scanning interferometry (CSI) using three different methods: Regional energy based, regional edge intensity based, and a combination of wavelet coefficients and local gradients were applied on different samples. Regional edge intensity was selected as the preferred fusion method for surface metrology, considering that the method was mainly focused on homogeneous datasets (CSI data at different magnifications). A multi-scale approach was presented and discussed both for the fine registration and for the fusion. A more general study was developed in reference [90], in which inhomogeneous data sets are fused: from an optical CMM and CSI.

In this section, a registration method and a fusion of data from different domains (inhomogeneous data sets), moreover from completely different scales is presented.

The two methods are photogrammetry data, as a 3D point cloud, and CSI data, as a series of heights on a uniform 2D grid. The higher resolution component of the photogrammetry data is the colour information rather than the 3D shape of the measured sample, as is seen in figure 6.2. The previous work outlined in this section was mainly focused on the fusion of surface topography measurements over similar measurement areas, using different measurement methods. However, in this work we attempt to register data on completely different scales, focusing on the localisation of micro-scale surface texture with respect to macro-scale form information.

6.1.2 Methodology for fusion of photogrammetry and CSI data

CSI is a measurement technique typically used for the measurement of micro-features and surface texture [60]. The field of view (FOV) for CSI methods typically ranges from tens of micrometres to a few millimetres, requiring many stitched measurements to cover larger areas. Surface topography measurement within a single FOV for CSI has relatively high accuracy compared to stitching of a large number of single measurements. Stitching of multiple CSI measurements can result in significant error of the surface form, due to the increased measurement uncertainty from the complex form and surfaces with high roughness [105] and as a result of the lateral distortion of the CSI system [27]. If lateral distortion is not corrected for, it can result in distortions to the measured surface geometry depending on where in the field-of-view a region is located. In turn, this negatively effects the registration of overlapping regions when stitching multiple CSI measurements.

At a FOV of around 10 mm to 20 mm, photogrammetry can achieve spatial resolutions on the order of 4 µm to 10 µm, depending of the camera being used. Recent work has also shown that photogrammetry is able to obtain measurement

uncertainties on the order of 10 µm over a FOV of around 20 mm [101], although accurate scaling methods over such ranges is problematic. Photogrammetry is able to capture form information at a lower spatial resolution than CSI with arbitrary scale, but can do so over a much larger FOV.

However, despite the lower spatial resolution of the form information captured by photogrammetry, the colour or image intensity information provides much higher resolution information about the object's surface. It is the colour information, or intensity for gray-scale images, of the photogrammetry data that provides sufficient overlap in sampled spatial frequencies that allows pre-alignment of the CSI point cloud to be achieved. The pre-alignment is required in order to account for the significant differences in the geometries measured by the CSI and photogrammetry. As there is a significant difference in the spatial bandwidths captured by the photogrammetry and CSI measurement methods, the direct application of ICP algorithms to the data will not result in a successful registration [6]. The nature of photogrammetry also means the resultant point cloud will have an arbitrary scale, requiring additional calibration to extract metric information. Fortunately, by pre-aligning the photogrammetry data with the CSI data, the photogrammetry point cloud can be appropriately scaled prior to the final registration.

The general pipeline for the fusion process can be seen in figure 6.1. Initially, the point cloud from the photogrammetry system is sampled as a 2D image and the CSI intensity map is processed in order to better represent the visual appearance of the region being measured. Feature matching algorithms are applied to the photogrammetry and CSI images in order to generate a planar transformation and scaling between the two data sets. This planar transform and scale factor allows the photogrammetry scale to be determined and the CSI data to be aligned in a single plane. This planar alignment of the CSI data fixes three degrees of freedom,

ensuring an ICP algorithm will successfully minimise the point cloud differences in an acceptable time frame. Finally, the point clouds are fused by removing points in the photogrammetry data that overlap with the CSI measurement region. The CSI data is then merged with the photogrammetry point cloud, replacing the original low-resolution data.

For this application, the CSI data were acquired with a ZYGO NewView™ 8300 CSI system using a Michelson 5.5× objective lens and a 0.5× zoom lens. The images used for the photogrammetry were acquired with a Nikon D3300 DSLR with a 60 mm macro lens and covering a FOV of approximately (20 × 20) mm. A total of thirty images were taken at a single camera elevataion and radius through a full rotation of the coin in the axis normal to the coin surface. The reconstruction of the images was achieved with Agisoft PhotoScan [2] and the final point cloud was exported as a tab-delimited text file (the point cloud).

6.1.3 Results for fusion of photogrammetry and CSI data

The first stage of the pipeline (shown in figure 6.1) requires both data sets to be projected into a 2D image for feature recognition methods to be applied. The nature of the CSI measurement means the CSI intensity map is already in the correct format. However, the photogrammetry data must be projected on to a plane and sampled into a discrete image. For this work, a one pence coin (British sterling) was used to demonstrate the procedure. For the coin sample, the point cloud was fitted to the x-y plane and projected along the z-axis to produce an image. The intensity image of the photogrammetry data is generated by sampling the RGB data of the point cloud in the x-y plane and then converting to a grey-scale image. The sampling frequency used to generate the image was chosen to approximately match the number of points in the point cloud. Assuming a square image, the

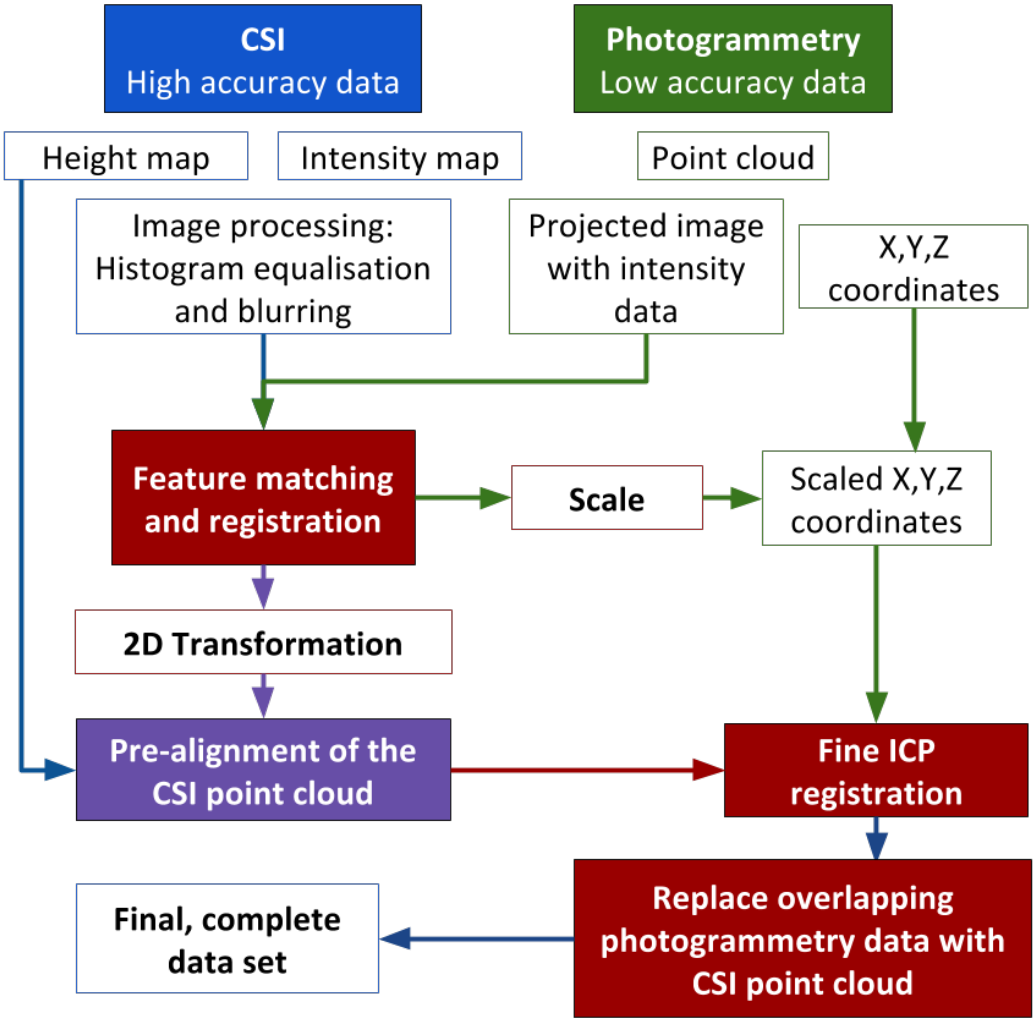

Fig. 6.1 Pipeline for the fusion of the CSI and photogrammetry data

number of samples was calculated as the square root of the total number of points to maximise the spatial resolution of the intensity image.

Once the intensity images for both the CSI and photogrammetry data have been generated, simple image processing is applied to the CSI intensity map to increase the contrast of any features in the image.

Prior to the feature detection process, the CSI data is further processed in order to account for the high number of high spatial frequency features visible in the intensity images. A Gaussian filter with a standard deviation of 6 pixels is applied to the CSI intensity image effectively blurring high-frequency features, such that only features visible in both data sets are detected. Effectively, the spatial bandwidth of the CSI data is reduced in order to only leave the region overlapping with the photogrammetry data.

With two images for comparison, image feature recognition algorithms can now be applied to determine the corresponding points between the data sets. Due to their performance under scale, rotation and illumination differences, scale-invariant feature transform (SIFT) algorithms where used to find corresponding features between the images. Once the SIFT features have been detected in both images and the descriptor vectors are assigned, the features are matched, and a set of corresponding pixel coordinates are produced [68]. In order to remove any false-positive matches, a fundamental matrix is calculated for the matched image coordinates and any points that do not satisfy the matrix are removed. As the fundamental matrix describes the relationship between points under different views, this removes false-positive matches that do not follow the general trend in point translation.

Finally, the relative rotation, translation and scale factor between the remaining point correspondences can be calculated. This will provide further refinement of

the data points until only positive matches remain. The translation matrix between the two data sets is described by the equation

$$\begin{bmatrix} x_{CSI} \\ y_{CSI} \\ 1 \end{bmatrix} = T \begin{bmatrix} x'_{CSI} \\ y'_{CSI} \\ 1 \end{bmatrix} \tag{6.1}$$

where T is a 2D rigid homogeneous transform, (x'_{CSI},y'_{CSI}) are the old CSI coordinates and (x_{CSI},y_{CSI}) are the shifted CSI data points. The 2D homogeneous transform matrix encodes the relative translation and rotation to align the CSI data in the x- and y-axes. The scale information is inversely applied to the photogrammetry point cloud in order to scale the data. In the case of multiple CSI measurements, an average scale can be calculated and applied to the data post-registration.

With the application of the 2D transformation matrix shown above, the CSI data is now registered in the x-y plane. This 2D registration is shown in figure 6.2, where the intensity image of the CSI and photogrammetry measurements are shown.

A simple z-axis registration is then applied by shifting the mean z heights of both data sets to zero. With the CSI data now fixed in three degrees of freedom, ICP algorithms can be applied to the CSI and photogrammetry point clouds in order to refine the z-axis translation and rotations about the x- and y-axes. The preliminary alignment is clearly necessary in order to reduce the number of iterations required in the ICP algorithm and to ensure a convergence of the ICP algorithm in a reasonable amount of time (the degrees of freedom are reduced from six to three thanks to the preliminary phases).

After the registration, the data are fused in to a single point cloud. The area of the photogrammetry point cloud corresponding to the CSI registered image is

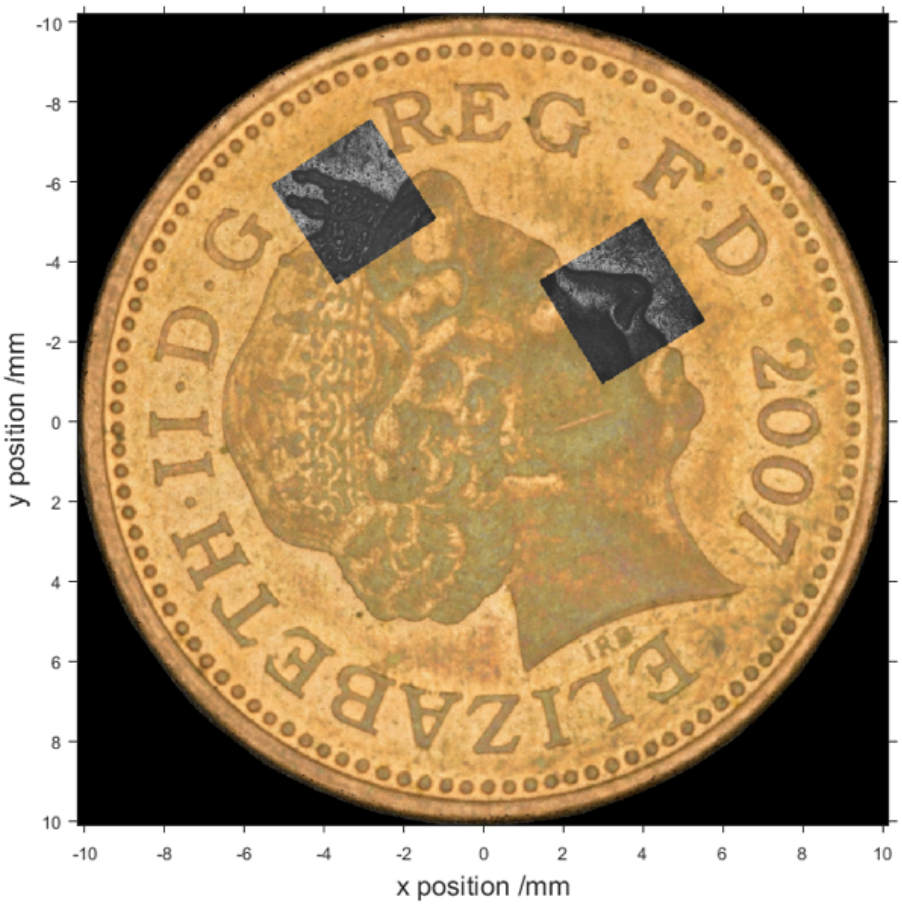

Fig. 6.2 CSI data alignment in the x-y plane

removed and the CSI data substituted. The final point cloud is shown around the CSI measurement regions in figure 6.3 and figure 6.4.

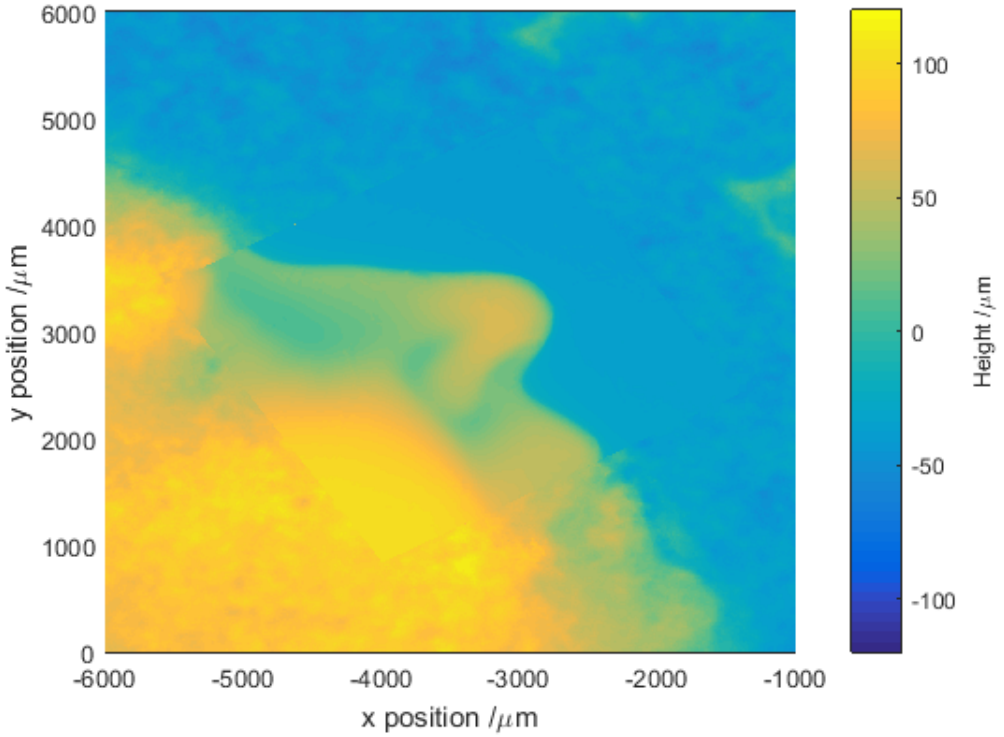

Fig. 6.3 Height map of the fused photogrammetry and CSI point clouds in the nose measurement region

As expected, discontinuities are observed in the fused point cloud around sharp transitions in height. The main difference in the CSI height map and photogrammetry data is not the heights of any particular region, but the distinction of where the step in height appears. As the CSI data provides a relatively high resolution height map of the coin surface, there is a distinct step in height between different regions, whereas the photogrammetry data shows a slope causing an apparent shift in the position of the edge. The improved resolution allows the localisation of micro-scale features, demonstrating the success of the methodology in increasing the bandwidth of the fused point cloud. Additionally, the CSI data also shows a significantly lower noise level compared to the photogrammetry data. This differ-

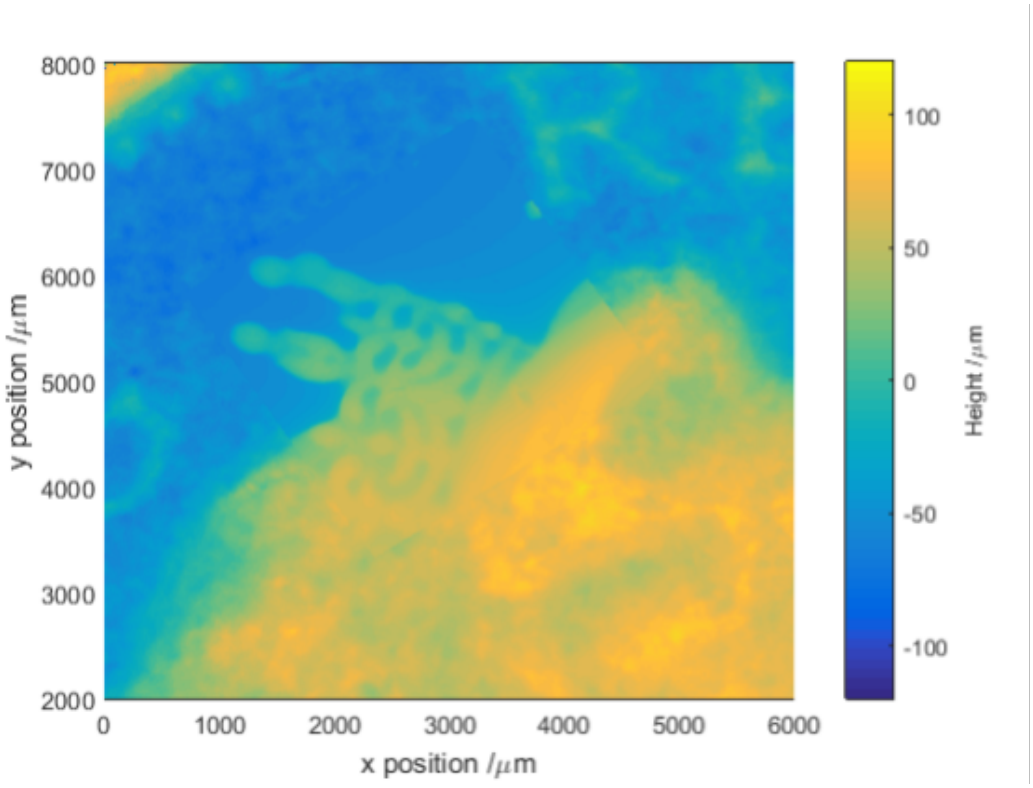

Fig. 6.4 Height map of the fused photogrammetry and CSI point clouds in the crown measurement region with magnified region

ence in noise is to be expected as the the feature size on the coin is very close to the resolution limit of the photogrammetry system. As a result, correspondence becomes difficult to accurately define at the pixel level, resulting in high frequency noise in the photogrammetry measurement.

With the CSI and photogrammetry data now registered, the topographies can be compared in order to determine the effectiveness of the registration procedure. The topography differences can be seen in figure 6.5 and figure 6.6 for the nose and crown measurement, respectively.

The the comparisons between CSI and photogrammetry data can also be represented as Abbot-Firestone curves, in which the cumulative material ratio is shown as function of height difference. The Abbot-Firestone curves for the nose and crown regions are shown in figures 6.7 and 6.8. As can be seen in figures 6.7 and 6.8, 95 % of topography differences lie within + 24 μm / - 33 μm and + 22 μm / - 29 μm, respectively . As would be expected, the most significant differences are observed on high spatial frequency features, such as edge responses and finer details not observed in the photogrammetry point cloud. These results confirm that the final point cloud presents an increased resolution and accuracy in the areas measured by the CSI (small details), and the overall and large-scale information from the photogrammetry.

6.1.4 Discussion of fusion of photogrammetry and CSI data

In this section, a methodology for the fusion of CSI and photogrammetry data has been presented with a test case scenario. A comparison of the final point clouds shows reasonable agreement in the registration of the CSI point cloud with the photogrammetry data, with only high spatial frequency features leading to substantial differences. Considering the minimal overlap in spatial bandwidth

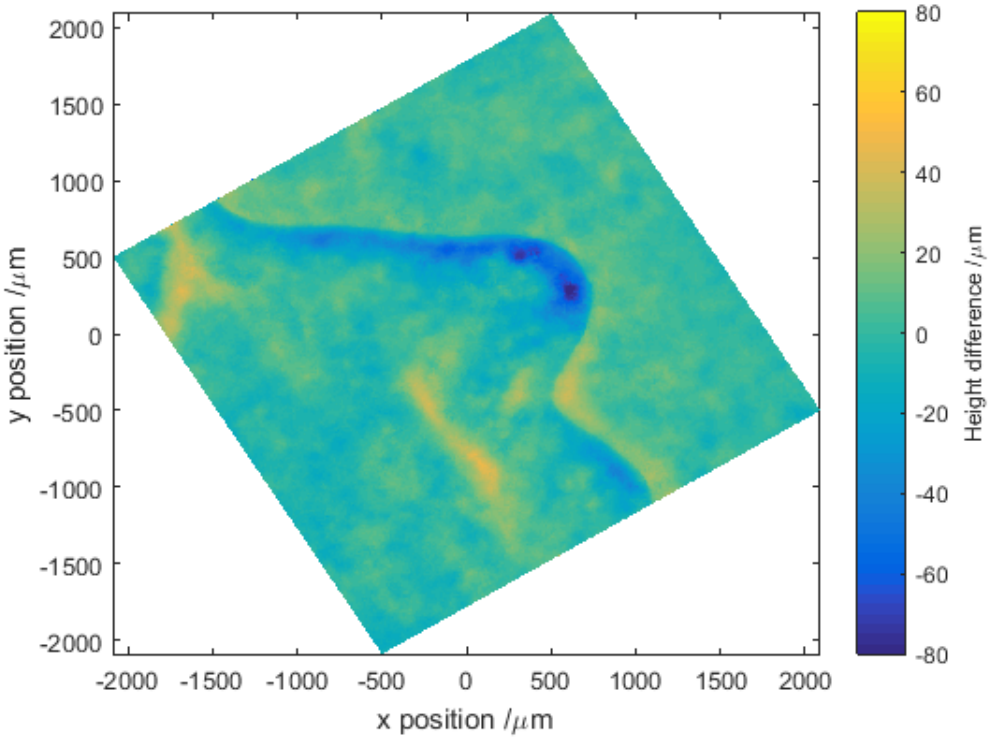

Fig. 6.5 Difference map between the photogrammetry and CSI point cloud data at the nose measurement region

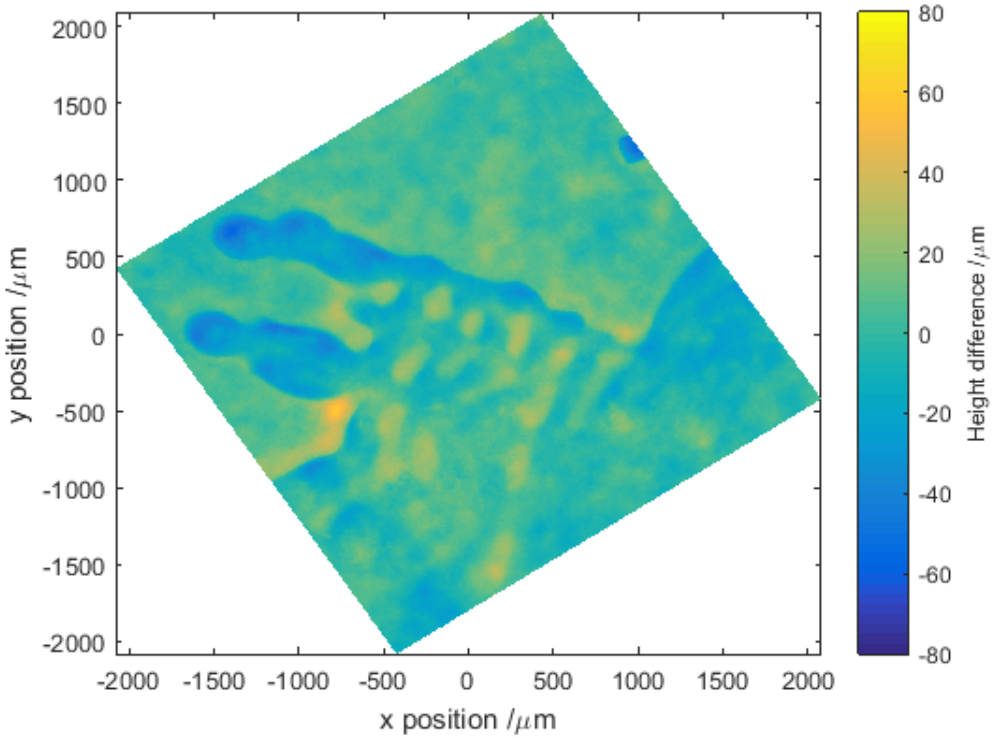

Fig. 6.6 Difference map between the photogrammetry and CSI point cloud data at the crown measurement region

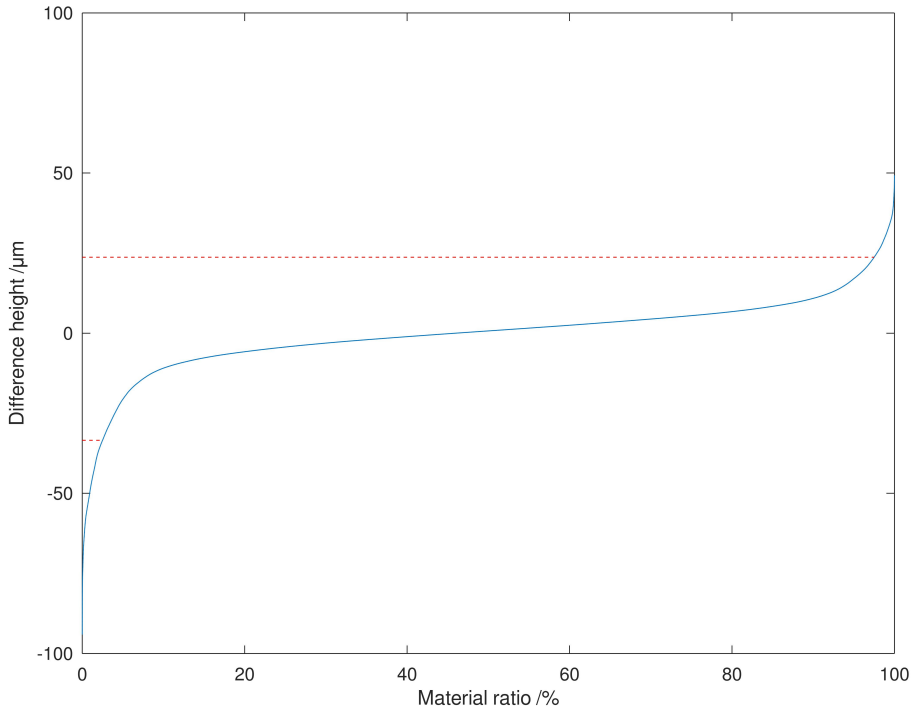

Fig. 6.7 Abbott-Firestone curve for the nose measurement region

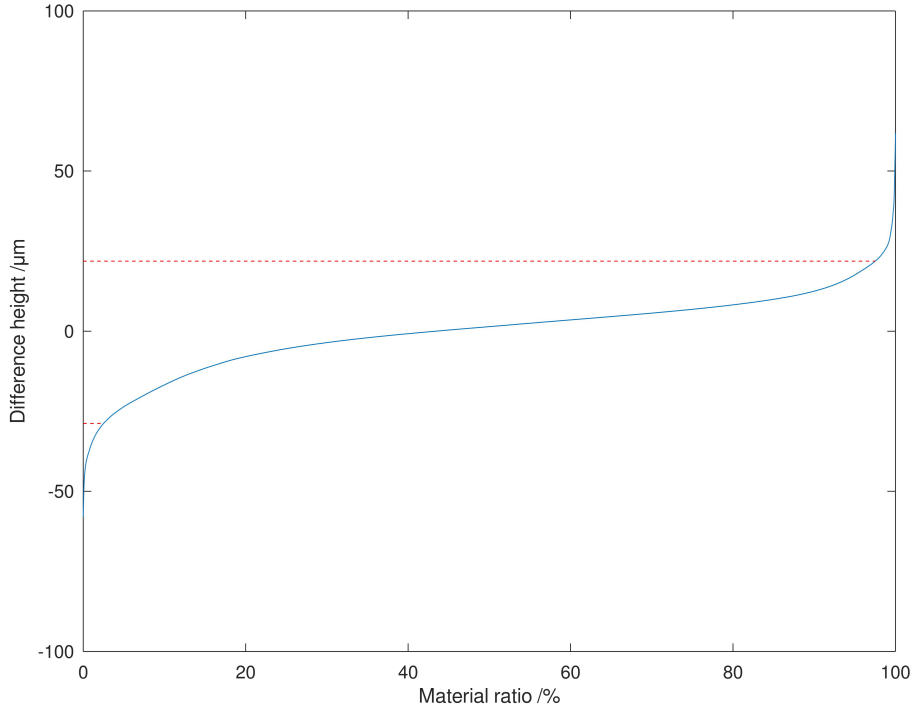

Fig. 6.8 Abbott-Firestone curve for the crown measurement region

between the two measurements, significant differences in small-scale features is to be expected. However, 95 % of the topographies have differences of under 34 μm, in agreement with measurement uncertainties typically achieved by photogrammetry systems [14]. Based on the general agreement of the point clouds, this verifies the CSI-photogrammetry fusion methodology's potential to substantially increase the spatial bandwidth of the subsequent point cloud. The fused point cloud covers features on the order of 4 µm to 20 mm, allowing form and micro-scale texture measurement simultaneously.

As a result of the significant difference in spatial frequencies captured by CSI and photogrammetry measurements, comparison of the point clouds results in differences of more than 10 µm. However, considering the nature of this fusion methodology, significant differences are expected and demonstrate the additional surface texture information gained. As can be seen in figure 6.3 and figure 6.4, there is a general agreement in the aligned data sets, with differences mainly occurring around edges and small-scale features. Figure 6.5 and figure 6.6 further demonstrate the success of the registration with flatter regions at different heights exhibiting similar levels of differences. In future work, the accuracy of the registration process will be evaluated through the measurement of a pre-calibrated geometry. The CSI data will be used for a high accuracy localisation of multiple features and the fused photogrammetry data will provide geometric distances between those features for comparison.

In conclusion, this section presents a new methodology for the fusion of CSI and photogrammetry data. The fused point cloud presents a substantially increased spatial bandwidth and accurate scaling of the photogrammetry data. With further development, the methodology will allow accurate stitching of CSI data over large areas without the need for high-precision motion stages.

6.2 Laser speckle for additive manufactured parts

6.2.1 Introduction to laser speckle for additive manufactured parts

Metrology for additive manufacturing (AM) is still in the early stages of development [111, 109, 30, 107]. The ability to measure highly complex and free-form parts from a diverse range of materials is both beneficial, and problematic from a metrological standpoint [62]. Mechanical contact techniques can provide accurate 3D measurements, but for complex parts, measurement times can be substantial. As has been discussed in chapter 2, photogrammetry can provide dense reconstructions of highly complex parts. A requirement of photogrammetry is that some texture must be observable on the object surface, making the highly textured surfaces of many AM parts ideal for finding point correspondences. For samples that do not display sufficient surface texture for correspondences to be found, a laser speckle projection system has been developed to project observable texture onto the object surface [101].

In this section, measurement uncertainties for a series of AM test artefacts are experimentally determined. The test artefacts have been produced in three materials: polymer powder bed fusion (Nylon 12), metal powder bed fusion (Ti-6Al-4V) and polymer material extrusion (ABS plastic). The design freedom of AM allows a CAD design to be easily produced in a wide range of materials. This range of materials, and hence surface textures, provides an opportunity to compare measurements of nominally the same geometry with a variety of surface textures. Each test artefact was measured with the photogrammetry system both without and with laser speckle projection modes and the resulting point clouds compared with the artefact CAD model. By then comparing the relative improvements in

reconstruction quality, coverage and accuracy, the effectiveness of the laser speckle projection system can be determined over a variety of materials and geometries.

6.2.2 Methodology for laser speckle for additive manufactured parts

Photogrammetry system

The photogrammetry system used in this section is the same system as used in chapter 4 utlising a laser speckle projection system. For the measurements in this section, the camera was placed at an elevation of approximately 45° in order to provide the best image coverage of both horizontal and vertical features. A lighting enclosure was also used in order to provide a diffuse and uniform light source for photogrammetry measurements in the absence of laser speckle. The diffuse lighting is produced with an open-sided box with a white diffusely reflecting internal surface and LED strip lighting placed on the top inner surface.

Due to the success of the laser projection system implemented in chapter 4, the same method was used for the laser projection in this work. The laser speckle projection system utilised a laser diode (532 nm, 4.5 mW), focusing lens (50 mm, biconvex) and a glass diffuser (600 grit polished). By focusing the laser beam onto the ground glass, a random interference pattern could be produced and projected onto the artefact surface. As in chapter 4, the projected laser speckle pattern also results in some subjective speckle due to interactions with the object surface. However, an F-stop value of eleven was chosen in order to produce a balance between a sufficiently large depth of field and sufficient reduction in the contrast of any subjective speckle.

Artefact designs

The four artefacts were produced based on a previously designed artefact made by the National Institute of Standards and Technology (NIST) [78], which was designed to enable manufacturers to investigate the performance and capabilities of their AM systems, with a variety of different geometrical features printed and measured. The shapes included in the four designed artefacts were specifically chosen based on a review of optical measurement techniques, as they have been highlighted as problematic shapes to measure. As such, these artefacts have been chosen to test the measurement technique with a variety of geometric features.

Figure 6.9 shows the artefacts that were additively manufactured in Ti-6Al-4V. Artefact (a) was made to test recess geometry, as opposed to the majority of features which extrude off the surface. Artefact (b) containing a sphere mounted in the centre is problematic for optical techniques due to the steep and varying surface slope angle. Artefact (c) was designed to test changing step heights, and the depth of field when measuring features at different/increasing heights. Artefact (d) containing pillars of different height and diameter poses problems for optical techniques as the larger pillars create occlusions for the smaller ones, resulting in missing data in the point clouds. By capturing a sufficient number of images, the amount of occlusions can be minimised, however, this may be difficult when the range of views is limited.

Scanning methodology

In order to compare photogrammetry with and without laser speckle, each artefact was measured in the same position for both conditions. Each artefact was also imaged thirty times through an angle of 270°, at equal spacing, in order to provide the best coverage of the sample without risking collision with the laser speckle

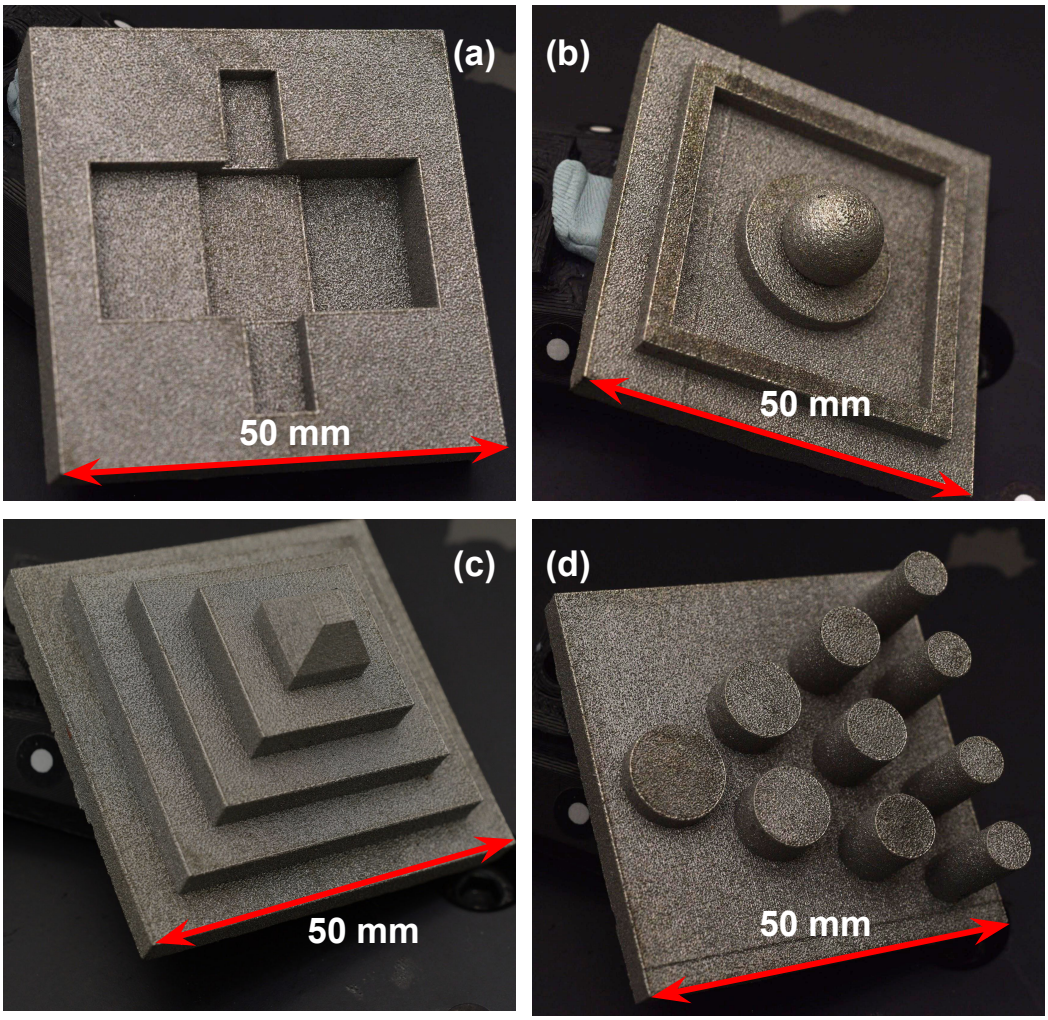

Fig. 6.9 AM artefacts produced in Titanium: (a) recess artefact; (b) sphere artefact; (c) pyramid artefact; (d) pillar artefact.

projection mounting. Each artefact was imaged successively, with and without the presence of laser speckle, in order to ensure that all conditions for both measurements were equal. This process was repeated for all four artefact designs in each material in order to provide a range of data for the comparison of the effect of laser speckle on both geometry and material differences.

Once all images had been captured, the photogrammetric reconstruction and calibration was achieved using commercial software (Agisoft PhotoScan) [2]. Each set of images produced a dense point cloud for which the 3D data could be extracted and exported for comparison to the original CAD information. The form measurement uncertainties for standard artefacts were around 17 μm with a 95 % confidence interval, as determined in previous work [101].

Data analysis

For the comparison with the CAD data, each point cloud was aligned and compared using commercial comparison software (CloudCompare) [43]. Due to the arbitrary scale of photogrammetric reconstructions, the point clouds were initially registered with the CAD data manually in order to provide an approximate registration for further refinement. The point clouds were then finely adjusted using a least-squares minimisation technique in order to match the CAD data as closely as possible. Calculating the distance of each point to a mesh generated from the CAD data, the error of each reconstruction could be determined. The standard deviation of the point cloud to mesh errors was then calculated for each point cloud and recorded as a measure of the accuracy of the reconstruction.

As the manufacturing methods used to produce the artefacts in Figure 6.9 have tolerances significantly larger than the measurement uncertainty of the photogrammetry system, it is also useful to make some qualitative comparisons between

reconstructions. The laser speckle projection method will result in complex interactions with both the surface texture and geometry of the samples that will not necessarily be reflected in the deviation from the CAD data. As a result, comparisons such as increases in surface area covered, distortions in geometry, differences in texture and general appearance were evaluated.

6.2.3 Results for laser speckle for additive manufactured parts

Qualitative analysis

For a qualitative analysis of the effect of the laser speckle projection system, the coverage area and visual quality of the reconstructions were compared. In turn, the coverage and apparent quality of each reconstruction was a significant indicator as to the ease at which it could be registered to the CAD data. A visual analysis of each artefact and material has also been useful in determining the effect of laser speckle on a variety of geometries and textures.

As can be seen in figure 6.10 (a), the laser speckle projection system was particularly effective for nylon-12 artefacts, compared to the image without speckle (Figure 6.10 (b)). The shift in the deviation values shown in figure 6.10 (a) is a result of the lack of measured points on the vertical side faces of the artefact. The lack of data on the vertical faces of the part results in a shift in the data points during the process of registration to the CAD data. Although relatively rough, nylon-12 additively manufactured parts exhibit very little observable texture due to the translucence of the material and lack of colour variation. This lack of observable texture on the nylon-12 samples effectively manifests as substantial reduction in the number of detected image features. As a high number of images features are required in order to provide an accurate estimation of the fundamental matrix, a reduced number of detected features negatively effects the self-calibration process.

The comparison shown in figure 6.10 demonstrates that the addition of high signal-to-noise ratio laser speckle features improves the quality of the resultant point cloud. However, the rise in signal-to-noise ratio results in either data drop-out or increased noise in areas that are occluded from the speckle projection, such as side walls. Despite the loss of some data points, the laser speckle projection method produced a consistently better coverage of the nylon artefacts compared to the image without laser speckle demonstrated by the reduction in the deviations from CAD. A detailed analysis of the deviation from CAD will be discussed in the following section.

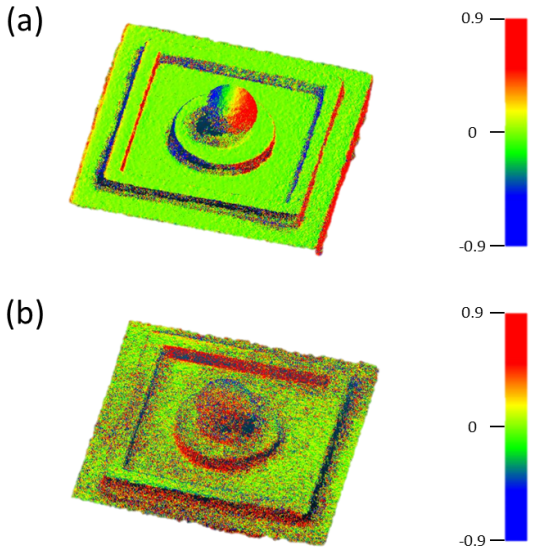

Fig. 6.10 Deviation of point cloud in millimetres from the CAD information for the sphere artefact with speckle (a) and without (b).

Although the ABS plastic extrusion manufactured artefacts provided substantially more observable surface texture than the nylon-12 versions, they still do not show as much much observable texture as the Titanium samples. Figure 6.11 shows the resultant point clouds for the ABS plastic recessed artefact with and without speckle, as well as each point's deviation from the original CAD data. Although the laser speckle measurement shown in figure 6.11(b) has a substantially

decreased level of error, there is evident loss of small scale features compared to the measurement without speckle. This loss of small-scale features is most likely a result of the feature density of the projected laser speckle acting as a filter for high-frequency features. This is demonstrated by the loss of the visibility of the track geometry of the top layer on the print, shown in Figure 6.11.

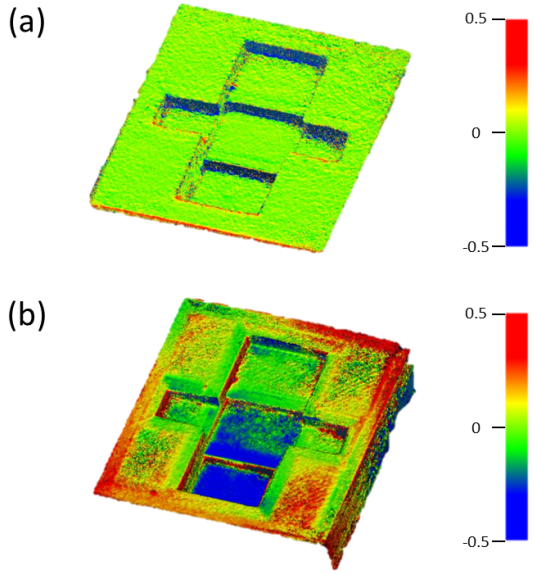

Fig. 6.11 Deviation of point cloud in millimetres from the CAD information for the ABS plastic recess artefact with speckle (a) and without (b).

Unlike the Nylon-12 and ABS plastic artefacts, the Ti-6Al-4V artefacts had very little to no difference in the coverage and quality of reconstruction with or without the application of speckle. As can be seen in figure 6.12, there is very little or no observable difference in the point clouds produced for the pyramid artefact. This lack of visual differences between measurements is due to the highly textured surface that is observable on the surface of parts additively manufactured in Ti-6Al-4V. It is still possible that the high spatial frequency filtering effect of the laser speckle pattern is having some influence on the reconstructed point cloud. However, due to the random nature of the small scale features on the Ti-6Al-4V

artefacts, the spatial frequency filtering effect is masked. While in truth there would be a filtering effect on the surface of the titanium parts, it is visually indiscernible.

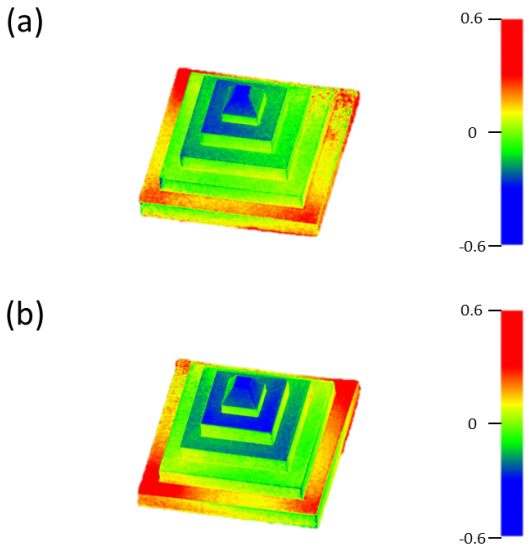

Fig. 6.12 Deviation of point cloud in millimetres from the CAD information for the Ti-6Al-4V pyramid artefact with speckle (a) and without (b).

A similar analysis can be carried out on the reconstructed images of the nylon pillar artefacts with and without speckle, shown in figure 6.13. From this qualitative analysis we can summarise that Figures 6.10 to 6.12 demonstrate some of the key behaviours of laser speckle projection based photogrammetry through the quality of reconstruction for a variety of geometries. All the measurements demonstrated a visual improvement in the measurement quality in the case of flat surfaces, with the main issues arising with surfaces that were not perpendicular to the laser speckle projection pattern. Given that vertical surfaces were not visually improved by the addition of speckle, it would suggest that occlusion of the laser speckle is the limiting factor for the measurement of vertical surfaces. In principle, a more effectively placed laser speckle projector should greatly reduce this issue.

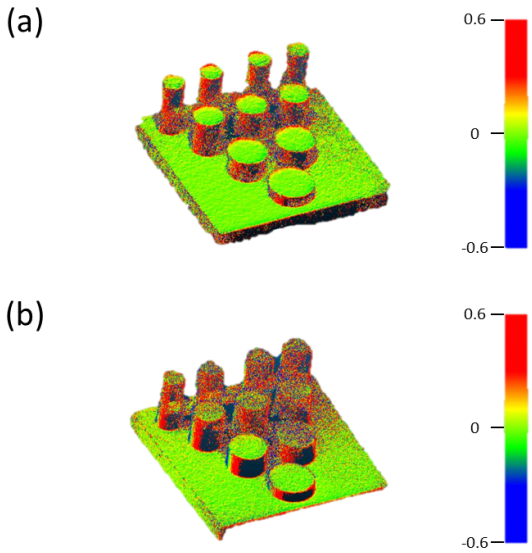

Fig. 6.13 Deviation of point cloud in millimetres from the CAD information for the Ti-6Al-4V pillar artefact with speckle (a) and without (b).

Quantitative analysis

The data produced by comparing the photogrammetry point cloud data and the original CAD design can be seen in table 6.1. As described in section 6.2.2, all point clouds were approximately aligned with the CAD data manually, and then finely registered automatically using a least-squares minimisation method. On average, the addition of laser speckle resulted in a 101 μm decrease in reconstruction error for the nylon artefacts, an 86 μm decrease for the ABS plastic artefacts and a 3 μm increase for the Ti-6Al-4V artefacts.

Table 6.1 Standard deviation in micrometres of the point cloud data from the CAD for all artefacts in Ti-6Al-4V, nylon and ABS plastic with ambient lighting and laser speckle.

Artefact	**Nylon**		**ABS Plastic**		**Titanium**	
	Non-speckle /μm	**Speckle /μm**	**Non-speckle /μm**	**Speckle /μm**	**Non-speckle /μm**	**Speckle /μm**
Pyramid	232	175	238	199	149	128
Recess	228	113	270	116	158	171
Sphere	368	174	242	173	190	215
Pillars	186	149	218	136	160	156

Table 6.2 Point count for the measurements of the artefacts in Ti-6Al-4V, nylon and ABS plastic with ambient lighting and laser speckle.

Artefact	Nylon		**ABS Plastic**		**Titanium**	
	Non-speckle	**Speckle**	**Non-speckle**	**Speckle**	**Non-speckle**	**Speckle**
Pyramid	1,519,347	1,229,514	972,701	1,306,432	1,779,431	1,705,338
Recess	1,049,288	846,994	1,107,917	935,352	1,233,845	1,199,809
Sphere	882,240	965,120	1,104,900	1,052,396	1,243,825	1,130,948
Pillars	1,356,018	1,067,613	1,291,530	1,138,872	1,426,925	1,370,095

The data in table 6.1 demonstrates a general trend of reduced reconstruction errors with the application of a laser speckle pattern with the nylon and ABS plastic artefacts. However, the Ti-6Al-4V artefacts displayed no significant difference in measurement error with or without laser speckle projection. Similarly, as table 6.2 shows, the titanium artefacts do not exhibit a significant difference in the total number of reconstructed points. However, the nylon and ABS plastic artefacts do not show an increase in measured data points, as would be expected. This is likely a result of the limited coverage of the laser speckle projection, as well as reduced contrast in region that the speckle does not cover. As such, the laser speckle in fact shows a reduction in points, but an increase in the accuracy of those points.

6.2.4 Conclusion of laser speckle for additive manufactured parts

From the qualitative and quantitative analysis, it can be concluded that the addition of laser speckle can significantly improve the quality and accuracy of a photogrammetric measurement. The improvement in photogrammetry data is most notable for objects that exhibit very little surface texture, with no significant effects in highly textured materials. This effect has been particularly evident on artefacts manufactured in Nylon-12 and ABS plastic due to their relatively low texture surfaces. In the case of the Nylon artefacts, a reduction in the point cloud standard deviation from the CAD data was as on average 101 μm or 40 % lower. Work on improvement of the laser speckle system positioning and control will be carried out in the future in order to further enhance the efficiency of the system. Furthermore, the qualitative analysis of the reconstructions has shown that the effect of the laser speckle on measurements is complex and dependant on surface texture and the geometry of the object. With the ABS plastic artefacts, the laser speckle appears to filter out the high spatial frequencies associated with the extrusion tracks that are clearly

visible when only ambient lighting is used. Conversely, with the Ti-6Al-4V artefacts, no obvious signs of filtering of high spatial frequencies is observed. Whether or not this disparity is a result of the lack of structure making the effect unclear, or differences in surface texture and material instead. In the future, more detailed theoretical and experimental work will be carried out to fully characterise the effects of geometry, material and surface texture on photogrammetric measurements. Additionally, a more effective method of evaluating the coverage of the artefacts will be investigated. Specifically, coverage in terms of surface area, rather than the total number of points that are captured.

6.3 Photogrammetry and light-field fusion

6.3.1 Introduction to photogrammetry and light-field fusion

A traditional camera system [71] can give a fast image of an object; moreover, a camera takes 2D images of a 3D object, and this transfer induces some loss of information. This loss of information is due to the inability of a camera to capture phase and depth information. Starting from this consideration, Adelson and Bergen [1] derived a new function, called the plenoptic function, able to describe all aspects of an image: motion, colour, amplitude, depth and orientation. They developed the 5D plenoptic function; where 3D are the spatial coordinates of a point which a ray from the object passes through and 2D are the angular coordinates indicating the direction of the ray. In this model, known as light-field imaging, the focus is not on the object, with its geometry and surface, but on the light rays; and by measuring the intensity of the ray, it is possible to get information about the 3D object. Later, Levoy and Hanrahan [63] defined the light-field as the radiance at a point in a given

direction, and because it remains constant as the ray propagates, they reduced the dimensionality of the plenoptic function from 5D to 4D.

In 2005, Ng [82] introduced the first portable plenoptic camera to sample light-fields. Lytro's camera is currently one of most popular, commercially available devices for light-field photography. Light-field cameras are able to capture 4D light fields, but do not record images at the same resolution as the image sensor. Each pixel is used to record a light ray, and multiple light rays are required to form a pixel that is produced by a traditional camera, as is discussed in chapter 2. This causes the final image recorded with a light-field camera to have a lower resolution than a traditional camera with the same image sensor. To overcome this limitation, different methods and techniques have been proposed [42, 123, 117, 113]. These include new designs for the light-field camera, such as hybrid imaging systems, attenuation masks or focused plenoptic cameras [91]. Also, various ray-or wave-optics models and computational algorithms have been employed to reconstruct high-resolution images [81, 110].

Despite different models, in order to use a camera as a metrology tool, it is necessary to express the obtained images in real-world coordinates; to achieve this, it is necessary to know the appropriate rigid transformations required to transform pixel measures into metric values, and the intrinsic parameters of the camera. The knowledge of these factors will influence the accuracy of the measurements. Different methods have been proposed for calibration of a plenoptic camera [21, 124, 11], however, they are sensitive to the position of the camera and can be time consuming. In this work, we implement a light-field camera within a photogrammetry system in order to capture additional depth information, as well as the photogrammetric point cloud. Through the fusion of the light-field and photogrammetric data, we show that it is possible to improve the measurement uncertainty compared to that

from the individual systems. In this work, different additive manufactured test artefacts were measured at different focal lengths. Point clouds were produced and depth-maps from photogrammetric data were compared to the Lytro depth map information, and triangulation of corresponding features between images. Using both measurements, fusion of the high density photogrammetric point cloud and light-field scale information was used to produce enhanced accuracy form measurement.

6.3.2 Methodology for photogrammetry and light-field fusion

Photogrammetry system

The photogrammetry system consists of a rotating stage with a camera mount that allows images to be taken at a predefined camera elevation through the required range of rotation (see [101] for details). The imaging system consists of a Lytro Illum light-field camera with a 40 mega-light-ray resolution. Mega-light-rays refers to the total number of individual light rays than can be detected and corresponds to a final image size of 2022×1404 pixels (2.8 MP). The rotating platform, where the samples were placed, was covered with a sheet of random texture. The additional texture provided correspondences for both the photogrammetric reconstruction and light-field depth map calculation, ensuring depth map data for the entirety of the field of view.

Experimental procedure

The first aim of this work was to show that, given a particular set of light-field camera parameters, there will be a repeatable relationship between the light-field depth map and the depth map calculated from the photogrammetric reconstruction. In order to determine if there is a repeatable relationship, four different additively

manufactured artefacts were imaged from six different camera positions with varying focal lengths. Based on the original CAD data, each point cloud and set of camera parameters could be scaled in order to have the correct scale information. Thirty images were captured through 360° for each artefact and for each position, after which the photogrammetric reconstruction for each was produced using commercial software [2]. Given all the photogrammetric reconstructions and light-field images, two depth map images can be produced for each view: the light-field based depth map and the photogrammetry point cloud depth map. Given the two depth maps for each image, comparisons can be made in order to determine if, with the same camera parameters, there is a repeatable relationship between the two depth maps. A more detailed description of the comparison process will be given in section 6.3.2. A repeatable relationship between both depth maps allows the Lytro depth map to be calibrated according to scales determined by the photogrammetric reconstruction. Subsequent scans would, therefore, be able to extract metric information from the photogrammetric reconstruction that has been scaled by the light-field depth map data. However, in order for this methodology to be applied to a generic sample, it is necessary to determine a general relationship between the camera parameters and the depth map. As focal length is the only user-defined factor that will affect the camera's intrinsic parameters, the least-squares gradient between depth maps was taken for a set of ten reconstructions with focal lengths varying between 30 mm and 50 mm.

Photogrammetric depth map

The commercial photogrammetry software produces both a point cloud for the sample and calibrated camera parameters for each individual reconstruction. The calibrated camera parameters are based on the pin-hole camera model and give a

camera projection matrix in the form

$$P = K \begin{bmatrix} R & T \end{bmatrix} \tag{6.2}$$

where K is the intrinsic camera matrix, R is the camera rotation matrix and T is the camera translation matrix. The later part of equation 6.2, $[R\ T]$ transforms the world coordinate system into the camera reference frame. The distance from the camera projection centre to an individual point D can be calculated according to

$$D = \sqrt{X'^2 + Y'^2 + Z'^2} \tag{6.3}$$

and

$$\begin{bmatrix} X' \\ Y' \\ Z' \end{bmatrix} = \begin{bmatrix} R & T \end{bmatrix} \begin{bmatrix} X \\ Y \\ Z \\ 1 \end{bmatrix} \tag{6.4}$$

where $[X\ Y\ Z\ 1]^T$ is the homogeneous world coordinate and $[X'\ Y'\ Z']^T$ is the coordinate in the camera reference frame. For all points in the point cloud, the image coordinates (u, v) can be calculated from equation 6.2 and the corresponding depth calculated from equation 6.3. However, before the photogrammetric depth map can be calculated, an appropriate scale must be applied in order to ensure the depths represent real dimensions. The scaling is achieved by first aligning the initial point cloud with the original CAD data by using an open-source software [43], then the transformation scale from the original data to the CAD can be applied to both the point cloud coordinates $[X\ Y\ Z\ 1]$ and the camera translation matrix T.

After the pixel coordinates and depths have been calculated for each camera, the points are binned into the closest pixel and the corresponding depth map image

$Im_{depth,Photo}(u,v)$ can be calculated. Issues in calculating the depth map can occur when considering pixel projections that pass through multiple surfaces on the sample to be measured. As can be seen in figure 6.14, some pixel projections may result in intersections with coordinates on the rear side of the sample, leading to a false depth. In order to avoid this issue, only flat sections have been selected from the point cloud; specifically, the flat background is selected in order to provide a consistent flat in all reconstructions.

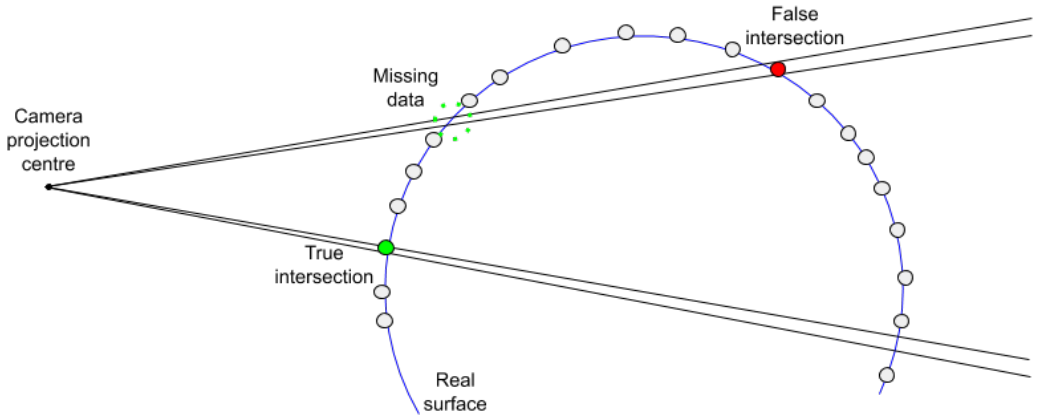

Fig. 6.14 Pixel projections through the artefact point cloud results in intersections with the rear face giving incorrect depths.

Comparison procedure

The Lytro software allows the user to produce a depth map image from any light-field image in the format of a 16-bit image and a minimum and a maximum lambda value; the image values are related to the difference in focus between the optical focal plane of the main lens at the time of capture and the virtual focal plane of the refocused image [72]. In order to correctly scale all light-field images, the 16-bit values must be altered according to

$$Im_{depth,Lytro,scaled}(u,v) = (Im_{depth,Lytro}(u,v)/2^{16}) \times (\lambda_{max} - \lambda_{min}) \qquad (6.5)$$

where $Im_{depth,Lytro,scaled}(u,v)$ is the scaled Lytro depth map image at pixel coordinates (u,v) and $Im_{depth,Lytro}(u,v)$ is the unscaled Lytro depth map, and λ_{max} and λ_{min} are the maximum and minimum lambda values, respectively. In this case, lambda refers to the pixel disparity value in the Lytro depth map.

With the corresponding depth maps $Im_{depth,Lytro,scaled}$ and $Im_{depth,Photo}$ it is then possible to compare the depth value at corresponding pixel coordinates. As can be seen in figure 6.15, there is an approximately linear relationship between the Lytro and photogrammetry depth map values. Variations in the graph shown in figure 6.15 are a result of errors in both the photogrammetry and lytro depth maps, particularly at the lambda is equal to zero point, in which the disparity in the light field images is minimised. A linear least-squares algorithm was used to fit the depth map data, and the gradient term is then used for comparison among different measurements.

6.3.3 Results for photogrammetry and light-field fusion

Depth analysis

The same Titanium artefacts described in section 4.3 were used in this work due to their high level of observable surface texture. Each artefact was imaged thirty times through 360° in order to capture the entire object from six different camera positions. Thirty images were captured in order to ensure a successful reconstruction without requiring long reconstruction times and six camera locations were used in order to ensure the behaviour is consistent for a range of depths. For each set of images, the process outlined in section 6.3.2 was performed on each image and the average gradient from the linear fits was calculated. The average gradients for each artefact in different camera positions are su mmarised in table 6.3.

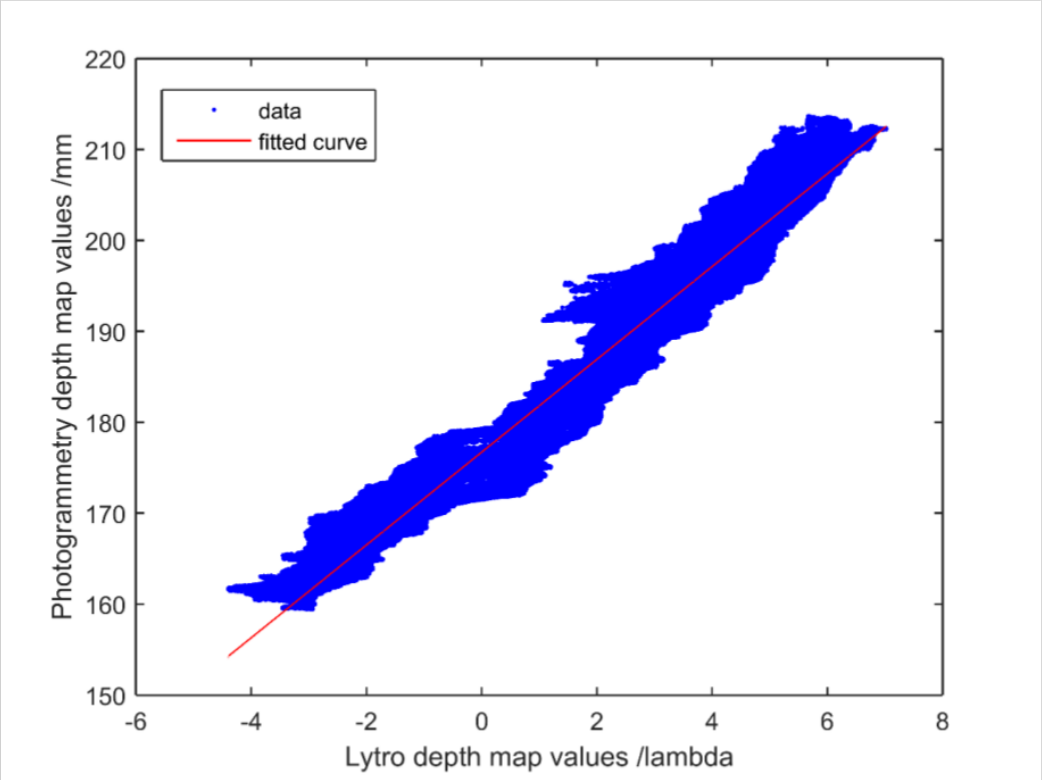

Fig. 6.15 Graph of the relationship between depth maps calculated from the light-field image and photogrammetry data. A linear least-squares fit was chosen to fit to the data.

Table 6.3 Gradient data for all four artefacts at six different positions. The standard deviation for each set has also been taken.

Artefact	**Gradient/ mmλ^{-1}**					
	Set 1	Set 2	Set 3	Set 4	Set 5	Set 6
Pillars	3.8357	3.6521	5.0192	7.7975	5.9465	5.1287
Pyramid	3.9422	3.5772	5.0437	7.7361	5.9335	5.2545
Recess	3.9641	3.6645	5.0728	7.7887	6.0401	5.1974
Sphere	3.9327	3.6616	5.0378	7.7872	5.9790	5.2184
Standard deviation /μmλ^{-1}	57	41	22	28	48	53

As can be seen in table 6.3, there is a consistent gradient between reconstructions made from the same camera positions with variations on the order of 1 % to 2 %. As described in section 6.3.2, the gradient values were analysed as a function of the chosen camera focal length in order to determine whether there is some predictable behaviour between the two variables. Eleven focal lengths between 30 mm and 50 mm were chosen and twenty images through 360° were taken and the mean linear gradient calculated for each set. As can be seen in figure 6.16, the calibrated focal lengths were then plotted against the mean gradient and a first order polynomial fit applied to determine the behaviour of the depth map gradients with focal lengths.

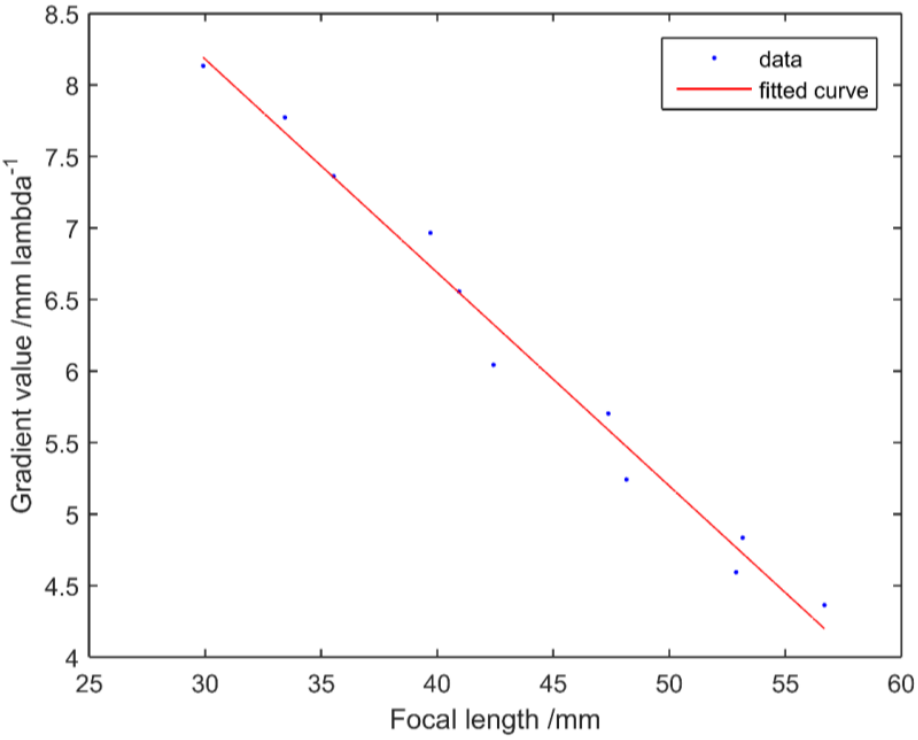

Fig. 6.16 Graph of the gradient of the Lytro to photogrammetric depth maps as a function of the camera focal length. The first order polynomial has also been fit to the data to show the relation between the two values.

Figure 6.16 shows that there is a clear relationship between the camera focal length and the depth map gradient, allowing the prediction of the reconstruction scale given a known focal length.

Measurement analysis

The artefact point clouds were also compared to the CAD data in order to provide a comparison with the measurement uncertainties taken with a conventional camera. In previous work, point cloud standard deviations from the CAD data were 149 μm, 158 μm, 190 μm and 160 μm for the Pyramid, Recess, Sphere and Pillars artefacts, respectively. The mean standard deviations for each measurement described in table 6.3 were 155 μm, 126 μm, 154 μm and 173 μm for the Pyramid, Recess, Sphere and Pillars artefacts, respectively. The difference in standard deviations from the standard camera and light-field camera set-up are comparable, with some improvement with the Recess and Sphere artefacts. However, considering the image resolution achieved by the light-field camera is almost an order of magnitude smaller, these results demonstrate the significant improvement in measurement quality that can be achieved with light-field technology.

6.3.4 Conclusion of photogrammetry and light-field fusion

In this section, photogrammetric data has been combined with light-field camera data in order to improve measurement uncertainty. Four additive manufactured parts with different geometric features has been measured with a Lytro Illum camera at different focal lengths. By using a rotating stage, thirty images were captured through 360° for each artefact for each position and the point clouds were produced from photogrammetric data. At this point, the depth maps from the photogrammetric data were plotted against the Lytro depth map information,

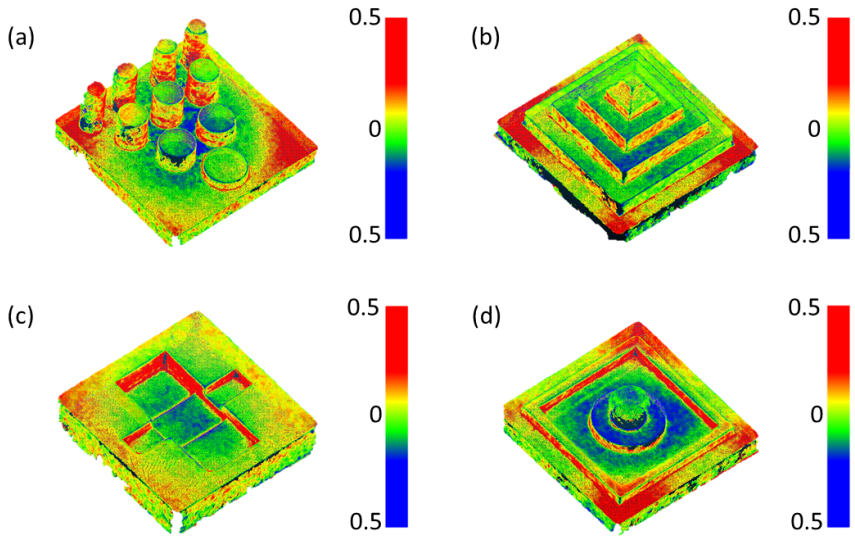

Fig. 6.17 Point cloud deviations from the original data for the Pillar (a), Pyramid (b), Recess (c) and Sphere (d) artefacts. The colour maps refer to the deviation from the CAD for each part of the sample and units are in millimetres.

showing an approximately linear relationship. Moreover, the depth map gradient was analysed with respect to the camera focal length; the data shows a clear relationship, allowing prediction of the reconstruction scale given the focal length. In conclusion, the comparison of the artefact point clouds with the CAD data showed a clear improvement in the measurement quality achieved with light-field technology.

Chapter 7

Conclusion and future work

7.1 Conclusions

The main focus of this work was to develop techniques to further advance the application of photogrammetry to coordinate metrology. This includes methods to better understand the propagation of of uncertainty through photogrammetry measurements, application of traceable scaling to reconstructions and methods for applying existing verification standards to photogrammetry systems. Several photogrammetry systems were developed, as well as several methods for the uncertainty evaluation and application of verification tests to the developed systems were proposed. Additionally, several case studies were applied using the developed systems and techniques, such as the fusion of photogrammetry data with other measurement technologies and the application of a novel laser speckle texture projection system in order to produce material agnostic measurements.

In chapter 3, a methodology for the evaluation of the three dimensional coordinate measurement uncertainty was described, as well as a method for the traceable calibration of the stereo systems scale factor. Additionally, the propagation of systematic errors in the stereo systems parameters through the measurement pro-

cedure was also investigated and experimentally verified during the scale factor calibration process, shown in section 3.3.1. The outcome of chapter 3 was a better understanding of the contributions of each parameter uncertainty to the expanded uncertainty on the three dimensional point measurement. This understanding of the contributions to the expanded uncertainty has allowed the key areas of improvement in the calibration and design of the stereo photogrammetry system to be highlighted for future work. The gauge block measurement process in section 3.3.3 also demonstrated a method for the calibration of the scale factor of the stereo system using a widely available and traceable, calibrated artefact. Finally, chapter 3 also provided an indication of the effect of systematic errors in the stereo parameters on the measurement volume and experimentally verified this effect through the comparison of the system with a laser interferometer, shown in section 3.3.2.

Through the use of laser speckle texture projection, chapter 4 demonstrates a novel methodology for the application of existing verification standards to conventional photogrammetry systems. The laser speckle texture projection system allowed conventional photogrammetry systems to measure smooth objects that do not exhibit any visible surface texture required for correspondences to be found, shown through the measurements in section 4.5. The laser speckle provided an artificial surface texture that allowed verification artefacts to be measured according to the verification standards and demonstrating the capacity of micro-scale photogrammetry systems to achieve form measurement uncertainties on the order of 10 μm.

For the stereo photogrammetry system developed in chapter 3, the verification procedure described in chapter 4 could not be applied due to the limitation of the camera optics and sensor. As a result, chapter 5 outlines an alternative verification

methodology based on the use of fringe projection principles in order to provide correspondence between the cameras in the stereo-camera pair. Additionally, by applying the VDI/VDE 2634 part 2 standards to the stereo photogrammetry system, further agreement with the three dimensional point measurement standard deviation predicted in chapter 3 was also provided. The final outcome of chapter 5 was the potential for a novel calibration procedure based on the structured errors, shown in section 5.3, on the measurement of large flats due to the non-linearities between the cameras and projector coupled with the imperfect calibration of the stereo system. The presence of structured errors in the reconstruction provides an ideal metric for the quality of the calibration, hence providing a more sensitive methodology compared to the calibration method used in the chapter.

Finally, in chapter 6 a range of novel applications of photogrammetry methods are presented. Firstly, a portable photogrammetry system was designed and developed for the measurement of dental fossil samples for a very large range of measurement volumes. The portable photogrammetry system is still in use in dental anthropology research based in the University of Arkansas. A method of fusing photogrammetry and CSI measurements was also presented in which the higher spatial frequencies captured in the colour information of photogrammetry measurements was utilised to find correspondence with CSI measurements. SIFT features and ICP algorithms were then utilised in order to accurately register the photogrammetry and CSI data, creating a fused data set with a vastly larger bandwidth than either individual measurement technology. The application of the laser speckle texture projection system described in chapter 4 was also investigated for its effect on the measurement of the same geometries with vastly different material properties. Through the measurement of a variety of materials with and without laser speckle, it was shown that the application of laser speckle allows

measurements of form without the influence of the material of the part. This allows the photogrammetry system to be much more robust to variations in surface properties, compared to other optical form measurement systems. The last section of chapter 6 demonstrates a methodology that allowed the automatic scaling of photogrammetry measurements through the fusion of photogrammetry and light-field camera data. The fusion of the light-field and photogrammetry data allows a scale factor to be applied to the reconstruction based on the intrinsic properties of the camera. This method was relatively low accuracy, but provided a highly robust method of scaling reconstructions that did not require any calibrated artefacts or extrinsic properties.

7.2 Future work

The Monte Carlo simulations developed in chapter 3 were applied to a single stereo pair of cameras. By extending this computational model in order to account for many cameras, the uncertainty of more complex photogrammetry systems could be evaluated. This ability to computationally model high complexity photogrammetry measurements would provide a better understanding of more complex interactions in multi-view photogrammetry automatically, removing the need for trial and error. For instance, the influence of the number of images used and the relative location of those images can be investigated for arbitrary measurements or specific geometries. This information would allow future systems to reduce the number of images that need to be captured whilst minimising the measurement uncertainty . Additionally, chapter 3 evaluated the influence feature location uncertainty on the measurement uncertainty. The next stage of development of the Monte Carlo simulation would be to consider the true probability distribution of the feature locations. The feature location uncertainty will be evaluated through a similar Monte Carlo based method,

in which all contribution factors to the feature location are accurately modelled in order to determine their contribution to the combined uncertainty. Not only would a better understanding of the feature location uncertainty allow for an accurate evaluation of the combined uncertainty for the coordinate measurements, it would also further improve the ability to highlight particular contribution factors and further reduce the measurement uncertainty of photogrammetry measurements.

The laser speckle texture projection system developed in chapter 4 was effective for the measurement of smooth objects. By implementing multiple speckle projector units within conventional single camera systems, or mounting the speckle projection unit stationary with respect to a stereo-camera system, coverage issues due to occlusions could be eliminated. By ensuring complete coverage of the part with laser speckle, this would ensure that entire object could be captured regardless of the contrast of the material texture. This would allow coordinate measurement systems to be developed that produce the same measurement performance regardless of material.

The method of using fringe projection techniques to provide correspondence between stereo cameras in chapter 5 could potentially be applied as a hybrid measurement system that combines the strengths of both photogrammetry and fringe projection. As the projector properties do not need to be characterised, the thermal and non-linear effects do not need to be accounted for, removing them as potential sources of error. Additionally, the use of phase to encode correspondence between images allows for a much more accurate localisation of corresponding points. As discussed in chapter 5, by developing a calibration process in which the low frequency errors seen in the measurement of a flat plane is minimised, significant improvement in the characterisation of the stereo-camera properties can be achieved. The integration of fringe projection and photogrammetry will allow

for better characterisation of the camera properties, hence reducing the overall measurement uncertainty, as suggested by chapter 3. Additionally, the reduced reliance on the characterisation of the projector can potentially increase the possible measurement accuracy of fringe projection.

The fusion of photogrammetry and CSI data based on feature matching between data sets was effective for the case provided, however, further work is required for a more robust methodology. By instead calibrating the coordinate system of the photogrammetry system and CSI in the same frame of reference, CSI measurements could be automatically located within photogrammetry measurements regardless of common visible features. This common frame of reference could be established through the use of targets easily visible by both systems, such as a checkerboard typically used for camera calibration. Furthermore, the photogrammetry system could track the location of the part to be measured within the CSI measurement volume, removing the need for a high-accuracy motion system for the CSI. This localisation of the part to be measured prior to CSI measurement then allows for a series of other complex developments, such as automated measurement positioning, collision avoidance and providing a priori information for the CSI measurement process.

References

[1] E. H. Adelson and J. R. Bergen. The plenoptic function and the elements of early vision. In *Computational Models of Visual Processing*, pages 3–20. MIT Press, 1991.

[2] Agisoft. Agisoft PhotoSCan, 2017.

[3] M. Aliverti, G. Pariani, M. Riva, B. Saggin, and M. Tarabini. Mechanical alignment of optical system: CMMs forces and damages on optical elements. In R. Navarro and R. Geyl, editors, *Advances in Optical and Mechanical Technologies for Telescopes and Instrumentation III*, volume 10706, pages 1323 – 1339. International Society for Optics and Photonics, SPIE, 2018.

[4] M. C. Arriaza, J. Yravedra, M. Domínguez-Rodrigo, M. Ángel Mate-González, E. G. Vargas, J. F. Palomeque-González, J. Aramendi, D. González-Aguilera, and E. Baquedano. On applications of micro-photogrammetry and geometric morphometrics to studies of tooth mark morphology: The modern olduvai carnivore site (tanzania). *Palaeogeography, Palaeoclimatology, Palaeoecology*, 488:103 – 112, 2017. Paleoecological reconstructions of the Bed I and Bed II lacustrine basins of Olduvai Gorge (Tanzania) and insights into early human behavior.

[5] M. M. Auerswald, A. von Freyberg, and A. Fischer. Laser line triangulation for fast 3d measurements on large gears. *The International Journal of Advanced Manufacturing Technology*, 100(9):2423–2433, Feb 2019.

[6] A. Babaei, M. Saadatseresht, and J. Kofman. Exponential fringe pattern projection approach to gamma-independent phase computation without calibration for gamma nonlinearity in 3d optical metrology. *Opt. Express*, 25(21):24927–24938, Oct 2017.

[7] A. Balsamo, M. Di Ciommo, R. Mugno, B. Rebaglia, E. Ricci, and R. Grella. Evaluation of CMM uncertainty through Monte Carlo simulations. *CIRP Annals - Manufacturing Technology*, 48(1):425–428, 1999.

[8] J. Batlle, E. Mouaddib, and J. Salvi. Recent progress in coded structured light as a technique to solve the correspondence problem: A survey. *Pattern Recognition*, 31(7):963–982, 1998.

[9] J.-A. Beraldin, B. Carrier, D. Mackinnon, and L. Cournoyer. Characterization of Triangulation- Based 3D Imaging Systems Using Certified Artifacts. *NCSL International Measure: The Journal of Measurement Science*, 7(4):50–60, 2012.

[10] C. Bergeles, P. Pratt, and R. Merrifield. Multi-view Stereo and Advanced Navigation for Transanal Endoscopic Microsurgery. *Miccai*, pages 332–339, 2014.

[11] Y. Bok, H.-G. Jeon, and I. Kweon. Geometric calibration of micro-lens-based light-field cameras using line features. *IEEE Transactions on Pattern Analysis and Machine Intelligence*, 8694:47–61, 09 2014.

[12] M. Born, E. Wolf, A. B. Bhatia, P. C. Clemmow, D. Gabor, A. R. Stokes, A. M. Taylor, P. A. Wayman, and W. L. Wilcock. *Principles of Optics: Electromagnetic Theory of Propagation, Interference and Diffraction of Light*. Cambridge University Press, 7 edition, 1999.

[13] A. K. Boyat and B. K. Joshi. A review paper: Noise models in digital image processing. *ArXiv*, abs/1505.03489, 2015.

[14] M. Brückner, F. Bajramovic, and J. Denzler. Intrinsic and extrinsic active self-calibration of multi-camera systems. *Machine Vision and Applications*, 25(2):389–403, 2014.

[15] W. Bösemann. Industrial photogrammetry - accepted metrology tool or exotic niche. *ISPRS - International Archives of the Photogrammetry, Remote Sensing and Spatial Information Sciences*, XLI-B5:15–24, 06 2016.

[16] Z. Chen, Y. Hu, X. Jiang, and Y. Chao. Light filed-based 3D reconstruction technique for micro-structure measurement. *Optics Express*, 24(2):1118–1132, 2016.

[17] Z. Chen, H. Liao, and X. Zhang. Telecentric stereo micro-vision system: Calibration method and experiments. *Optics and Lasers in Engineering*, 57:82–92, 2014.

[18] J. Claverley and R. Leach. A review of the existing performance verification infrastructure for micro-CMMs. *Precision Engineering*, 39:1–15, 2015.

[19] B. M. Colosimo, M. Pacella, and N. Senin. Multisensor data fusion via Gaussian process models for dimensional and geometric verification. *Precision Engineering*, 40:199–213, 2015.

[20] T. Coveney. Good Practice Guide No.39. *Dimensional Measurement using Vision Systems*, (2), 2014.

[21] D. G. Dansereau, O. Pizarro, and S. B. Williams. Decoding, calibration and rectification for lenselet-based plenoptic cameras. In *Proceedings of the 2013 IEEE Conference on Computer Vision and Pattern Recognition*, CVPR '13, pages 1027–1034, Washington, DC, USA, 2013. IEEE Computer Society.

[22] R. Danzl, F. Helmli, and S. Scherer. Focus Variation - A new Technology for High Resolution Optical 3D Surface Metrology. *10th International Conference of Slovenian Society for Non-Destructive Testing*, pages 1–10, 2009.

[23] G. Di Leo, C. Liguori, and A. Paolillo. Propagation of uncertainty through stereo triangulation. *2010 IEEE International Instrumentation and Measurement Technology Conference, I2MTC 2010 - Proceedings*, pages 12–17, 2010.

[24] Z. Dong, X. Sun, W. Liu, and H. Yang. Measurement of free-form curved surfaces using laser triangulation. *Sensors*, 18(10), 2018.

[25] P. Drap and J. Lefèvre. An exact formula for calculating inverse radial lens distortions. *Sensors (Switzerland)*, 16(6):1–18, 2016.

[26] X. Duan, C. Wang, J. Wang, and H. Zhao. A new calibration method and optimization of structure parameters under the non-ideal condition for 3D measurement system based on fiber-optic interference fringe projection. *Optik*, 172(May):424–430, 2018.

[27] P. Ekberg, R. Su, and R. K. Leach. High-precision lateral distortion measurement and correction in coherence scanning interferometry using an arbitrary surface. *Optics Express*, 25(16):18703, 2017.

[28] N. El Akkad, M. Merras, A. Saaidi, and K. Satori. Camera self-calibration with varying intrinsic parameters by an unknown three-dimensional scene. *The Visual Computer*, 30(5):519–530, 2013.

[29] T. Etzion. Constructions for perfect maps and pseudorandom arrays. *IEEE Trans. Inf. Theor.*, 34(5):1308–1316, Sept. 2006.

[30] S. K. Everton, M. Hirsch, P. Stravroulakis, R. K. Leach, and A. T. Clare. Review of in-situ process monitoring and in-situ metrology for metal additive manufacturing. *Materials Design*, 95:431 – 445, 2016.

[31] H. Fathi and I. Brilakis. Multistep Explicit Stereo Camera Calibration Approach to Improve Euclidean Accuracy of Large-Scale 3D Reconstruction. *Journal of Computing in Civil Engineering*, page 04014120, 2014.

[32] I. O. for Standardization. ISO 3650:1998 Geometrical Product Specifications (GPS) — Length standards — Gauge blocks. *ISO*, 1998.

[33] A. Fragione, A. Sanchez Salmeron, F. Modica, and G. Percoco. Multi-step approach for automated scaling of photogrammetric micro-measurements. *International Journal of Advanced Manufacturing Technology*, pages 747–757, 2019.

[34] C. Fraser, S. Cronk, and H. Hanley. Close-range photogrammetry in traffic incident management. *ISPRS Congress*, pages 3–6, 2008.

[35] R. Furukawa, D. Miyazaki, M. Baba, S. Hiura, and H. Kawasaki. Robust structured light system against subsurface scattering effects achieved by cnn-based pattern detection and decoding algorithm. In *The European Conference on Computer Vision (ECCV) Workshops*, September 2018.

[36] L. Galantucci, M. Pesce, and F. Lavecchia. A stereo photogrammetry scanning methodology, for precise and accurate 3D digitization of small parts with sub-millimeter sized features. *CIRP Annals - Manufacturing Technology*, 64(1):507–510, 2015.

[37] L. M. Galantucci, P. Bari, and P. Bari. Accuracy Issues of Digital Photogrammetry for 3D Digitization of Industrial Products. *Revue Internationale de Ingegnerie Numerique,*, 2(1-2):29–40, 2006.

[38] L. M. Galantucci, F. Lavecchia, G. Percoco, and S. Raspatelli. New method to calibrate and validate a high-resolution 3D scanner, based on photogrammetry. *Precision Engineering*, 38(2):279–291, 2014.

[39] L. M. Galantucci, M. Pesce, and F. Lavecchia. A powerful scanning methodology for 3D measurements of small parts with complex surfaces and sub millimeter-sized features, based on close range photogrammetry. *Precision Engineering*, 43:211–219, 2016.

[40] A. Gallo, M. Muzzupappa, and F. Bruno. 3D reconstruction of small sized objects from a sequence of multi-focused images. *Journal of Cultural Heritage*, 15(2):173–182, 2014.

[41] J. Geng. Structured-light 3D surface imaging: a tutorial. *Advances in Optics and Photonics*, 3(2):128, 2011.

[42] T. Georgiev, G. Chunev, and A. Lumsdaine. Superresolution with the focused plenoptic camera. In *Computational Imaging*, 2011.

[43] D. Girardeau-Montaut. Cloudcompare (2.x) [gpl software]. http://www.cloudcompare.org/, 2017.

[44] H. González-Jorge. Verification artifact for photogrammetric measurement systems. *Optical Engineering*, 50(7):073603, 2011.

[45] J. Goodman. *Speckle Phenomena in Optics: Theory and Applications*. Roberts & Company, 2007.

[46] S. S. Gorthi and P. Rastogi. Fringe projection techniques: Whither we are? *Optics and Lasers in Engineering*, 48(2):133–140, 2010.

[47] F. Gu, H. Zhao, Y. Ma, and P. Bu. Camera calibration based on the back projection process. *Measurement Science and Technology*, 26(12):125004, 2015.

[48] O. Guarneros, J. de Vicente, M. Maya, J. L. Ocaña, C. Molpeceres, J. J. García-Ballesteros, S. R. Rodríguez, and H. M. Duran. Uncertainty Estimation for Performance Evaluation of a Confocal Microscope as Metrology Equipment. *Mapan*, 29(1):29–42, 2014.

[49] M. Guerra, C. Volpone, L. Galantucci, and G. Percoco. Photogrammetric measurements of 3d printed microfluidic devices. *Additive Manufacturing*, 21:53 – 62, 2018.

[50] R. Hartley and A. Zisserman. *Multiple view geometry in computer vision*. Cambridge University Press, 2nd edition, 2004.

[51] M. Hong and G. Meng. Laser scanning confocal microscopy 3d surface metrology applications. *Microscopy and Microanalysis*, 24(S1):1140–1141, 2018.

[52] ISO. Geometrical product specifications (GPS) — Acceptance and reverification tests for coordinate measuring machines Part 8 : CMMs with optical distance sensors ISO / CEN PARALLEL PROCESSING. *ISO 10360*, 2013.

[53] J. C. F. G. I. M. Jcgm. Evaluation of measurement data — Guide to the expression of uncertainty in measurement. *International Organization for Standardization Geneva ISBN*, 50(September):134, 2008.

[54] Joint Committee for Guides in Metrology. Evaluation of measurement data — Supplement 1 to the "Guide to the expression of uncertainty in measurement" — Propagation of distributions using a Monte Carlo method. *Evaluation*, JCGM 101:2:90, 2008.

[55] X. Ju, H. Henseler, M. J.-q. Peng, B. S. Khambay, A. K. Ray, and A. F. Ayoub. Multi-view stereophotogrammetry for post-mastectomy breast reconstruction. *Medical & Biological Engineering & Computing*, 2015.

[56] R. Klowsky, A. Kuijper, and M. Goesele. Modulation transfer function of patch-based stereo systems. *Proceedings of the IEEE Computer Society Conference on Computer Vision and Pattern Recognition*, pages 1386–1393, 2012.

[57] A. Koutsoudis, G. Ioannakis, B. Vidmar, F. Arnaoutoglou, and C. Chamzas. Using noise function-based patterns to enhance photogrammetric 3D reconstruction performance of featureless surfaces. *Journal of Cultural Heritage*, 16(5):664–670, 2015.

[58] F. Lavecchia, M. G. Guerra, and L. M. Galantucci. The influence of software algorithms on photogrammetric micro-feature measurement's uncertainty. *The International Journal of Advanced Manufacturing Technology*, 93(9):3991–4005, Dec 2017.

[59] F. Lavecchia, M. G. Guerra, and L. M. Galantucci. Performance verification of a photogrammetric scanning system for micro-parts using a three-dimensional artifact: adjustment and calibration. *International Journal of Advanced Manufacturing Technology*, 96(9-12):4267–4279, 2018.

[60] R. K. Leach, editor. *Optical Measurement of Surface Topography*, volume 53. Springer-Verlag Berlin Heidelberg, 1 edition, 2011.

[61] R. K. Leach. *Fundemental Principles of Engineering Nanometrology*. Elsevier, 2nd edition, 2014.

[62] R. K. Leach, D. Bourell, S. Carmignato, M. Donmez, and N. Senin. Geometrical metrology for metal additive manufacturing - keynote presentation at cirp ga, birmingham 2019. 08 2019.

[63] M. Levoy and P. Hanrahan. Light field rendering. In *SIGGRAPH*, 1996.

[64] J. Li, H. Ren, P. Luo, X. Gao, and Z. Wang. Specular reflection compensation in homography fringe projection profilometry. *Optik*, 140:413–422, 2017.

[65] A. Lingua, D. Marenchino, and F. Nex. Performance Analysis of the SIFT Operator for Automatic Feature Extraction and Matching in Photogrammetric Applications. *Sensors*, 9(5):3745–3766, 2009.

[66] A. Loderer and T. Hausotte. Qualification concept for optical multi-scale multi-sensor systems. *Journal of Sensors and Sensor Systems*, 5(1):1–8, 2016.

[67] M. Lourakis and R. Deriche. Camera self-calibration using the singular value decomposition of the fundamental matrix: From point correspondences to 3D measurements. *De Recherche En Informatique Et En*, page 45, 1999.

[68] D. G. Lowe. Distinctive image features from scale-invariant keypoints. *International Journal of Computer Vision*, 60(2):91–110, 2004.

[69] T. Luhmann. Close range photogrammetry for industrial applications. *ISPRS Journal of Photogrammetry and Remote Sensing*, 65(6):558–569, 2010.

[70] T. Luhmann, C. Fraser, and H. G. Maas. Sensor modelling and camera calibration for close-range photogrammetry. *ISPRS Journal of Photogrammetry and Remote Sensing*, 115:37–46, 2016.

[71] T. Luhmann and S. Robson. *Close Range Photogrammetry : Principles, Techniques and Applications*. Whittles Publishing, 2011.

[72] Lytro. Lytro support.

[73] I. Martynov, J.-K. Kamarainen, and L. Lensu. Projector calibration by "inverse camera calibration". In A. Heyden and F. Kahl, editors, *Image Analysis*, pages 536–544, Berlin, Heidelberg, 2011. Springer Berlin Heidelberg.

[74] P. M. Mather and M. Koch. *Computer Processing of Remotely-Sensed Images*. Wiley-Blackwell, fourth edi edition, 2011.

[75] L. Mignard-Debise and I. Ihrke. Light-Field Microscopy with a Consumer Light-Field Camera. *Proceedings - 2015 International Conference on 3D Vision, 3DV 2015*, pages 335–343, 2015.

[76] Y. Miura, S. Nakanishi, E. Higuchi, K. Takamasu, M. Abe, and O. Sato. Comparative evaluation of estimation of hole plate measurement uncertainty via Monte Carlo simulation. *Precision Engineering*, 56(May 2018):496–505, 2019.

[77] J. J. Moré. The levenberg-marquardt algorithm: Implementation and theory. In G. A. Watson, editor, *Numerical Analysis*, pages 105–116, Berlin, Heidelberg, 1978. Springer Berlin Heidelberg.

[78] S. Moylan, J. Slotwinski, A. Cooke, K. Jurrens, and M. A. Donmez. An additive manufacturing test artifact. *Journal of Research of the National Institute of Standards and Technology*, 119:429–459, 2014.

[79] C. Möller, H. C. Schmidt, N. H. Shah, and J. Wollnack. Enhanced absolute accuracy of an industrial milling robot using stereo camera system. *Procedia Technology*, 26:389 – 398, 2016. 3rd International Conference on System-Integrated Intelligence: New Challenges for Product and Production Engineering.

[80] L. Newton, N. Senin, C. Gomez, R. Danzl, F. Helmli, L. Blunt, and R. Leach. Areal topography measurement of metal additive surfaces using focus variation microscopy. *Additive Manufacturing*, 25:365 – 389, 2019.

[81] R. Ng. Fourier slice photography. *ACM Trans. Graph.*, 24(3):735–744, July 2005.

[82] R. Ng, M. Levoy, M. Brédif, and G. Duval. Light field photography with a hand-held plenoptic camera. *Stanford University Computer Science Tech Report CSTR 2005-02*, pages 1–11, 2005.

[83] J. Pan, X. Yang, H. Cai, and B. Mu. Image noise smoothing using a modified kalman filter. *Neurocomputing*, 173:1625 – 1629, 2016.

[84] G. Percoco, F. Lavecchia, and A. J. S. Salmerón. Preliminary Study on the 3D Digitization of Millimeter Scale Products by Means of Photogrammetry. *Procedia CIRP*, 33:257–262, 2015.

[85] G. Percoco, F. Modica, and F. Stefano. 'image analysis for 3d micro-features: A new hybrid measurement method. *Precision Engineering*, 11 2016.

[86] G. Percoco and A. J. Sánchez Salmerón. Photogrammetric measurement of 3D freeform millimetre-sized objects with micro features: an experimental validation of the close-range camera calibration model for narrow angles of view. *Measurement Science and Technology*, 26(9):095203, 2015.

[87] M. Pesce, L. Galantucci, G. Percoco, and F. Lavecchia. A Low-cost Multi Camera 3D Scanning System for Quality Measurement of Non-static Subjects. *Procedia CIRP*, 28:88–93, 2015.

[88] T. Pinto, C. Kohler, and A. Albertazzi. Regular mesh measurement of large free form surfaces using stereo vision and fringe projection. *Optics and Lasers in Engineering*, 50(7):910–916, 2012.

[89] T. Pribanić, H. Džapo, and J. Salvi. Efficient and low-cost 3D structured light system based on a modified number-theoretic approach. *Eurasip Journal on Advances in Signal Processing*, 2010(November 2015), 2010.

[90] S. K. Ramasamy. *Multi-scale Data Fusion for Surface Metrology*. Proquest Dissertation Publishing, 2012.

[91] Raytrix. Raytrix:3d light field camera technology.

[92] C. Reich, R. Ritter, and J. Thesing. White light heterodyne principle for 3D-measurement. In O. Loffeld, editor, *Sensors, Sensor Systems, and Sensor Data Processing*, volume 3100, pages 236 – 244. International Society for Optics and Photonics, SPIE, 1997.

[93] F. Remondino, E. Baltsavias, S. El-Hakim, M. Picard, and L. Grammatikopoulos. Image-Based 3D Modeling of the Erechteion, Acropolis of Athens. *International Archives of the Photogrammetry, Remote Sensing and Spatial Information Sciences*, pages 1083–1092, 2008.

[94] R. Saiga, A. Takeuchi, K. Uesugi, Y. Terada, Y. Suzuki, and R. Mizutani. Method for estimating modulation transfer function from sample images. *Micron*, 105:64 – 69, 2018.

[95] J. Salvi, X. Armanguã, and J. Batlle. A comparative review of camera calibrating methods with accuracy evaluation. *Pattern Recognition*, 35:1617–1635, 2002.

[96] J. Salvi, S. Fernandez, T. Pribanic, and X. Llado. A state of the art in structured light patterns for surface profilometry. *Pattern Recognition*, 43(8):2666–2680, 2010.

[97] W. Sankowski, M. Włodarczyk, D. Kacperski, and K. Grabowski. Estimation of measurement uncertainty in stereo vision system . *Image and Vision Computing*, 61:70–81, 2017.

[98] M. Schaffer, M. Grosse, and R. Kowarschik. High-speed pattern projection for three-dimensional shape measurement using laser speckles. *Applied optics*, 49:3622–3629, 2010.

[99] B. Sheta, M. Elhabiby, and N. El-Sheimy. Comparison and analysis of nonlinear least squares methods for vision based navigation (vbn) algorithms. *XXII ISPRS Congress,, Melbourne, Australia*, 39, 07 2012.

[100] J. Siebert and S. Marshall. Human body 3D imaging by speckle texture projection photogrammetry. *Sensor Review*, 20(3):218–226, 2000.

[101] D. Sims-Waterhouse, S. Piano, and R. K. Leach. Verification of micro-scale photogrammetry for smooth three-dimensional object measurement. *Measurement Science and Technology*, 28(5), 2017.

[102] C. Stamatopoulos and C. S. Fraser. Calibration of long focal length cameras in close range photogrammetry. *The Photogrammetric Record*, 26(135):339–360, 2011.

[103] P. Stavroulakis and R. K. Leach. Review of post-process optical form metrology for industrial-grade metal additive manufactured parts. *Review of Scientific Instruments*, 87:041101, 04 2016.

[104] Stelzer. Contrast, resolution, pixelation, dynamic range and signal-to-noise ratio: fundamental limits to resolution in fluorescence light microscopy. *Journal of Microscopy*, 189(1):15–24, 1998.

[105] R. Su, Y. Wang, J. Coupland, and R. K. Leach. On tilt and curvature dependent errors and the calibration of coherence scanning interferometry. *Opt. Express*, 25(4):3297–3310, 2017.

[106] P. Sun, N. G. Lu, M. L. Dong, B. X. Yan, and J. Wang. Simultaneous All-Parameters Calibration and Assessment of a Stereo Camera Pair Using a Scale Bar. *Sensors (Basel, Switzerland)*, 18(11):1–19, 2018.

[107] G. Tapia and A. Elwany. A Review on Process Monitoring and Control in Metal-Based Additive Manufacturing. *Journal of Manufacturing Science and Engineering*, 136(6), 10 2014. 060801.

[108] A. J. Theuwissen. CMOS image sensors: State-of-the-art. *Solid-State Electronics*, 52(9):1401–1406, 2008.

[109] A. Thompson, I. Maskery, and R. K. Leach. X-ray computed tomography for additive manufacturing: a review. *Measurement Science and Technology*, 27(7):072001, jun 2016.

[110] L. Tian, Z. Zhang, J. C. Petruccelli, and G. Barbastathis. Wigner function measurement using a lenslet array. *Opt. Express*, 21(9):10511–10525, May 2013.

[111] A. Townsend, N. Senin, L. Blunt, R. Leach, and J. Taylor. Surface texture metrology for metal additive manufacturing: a review. *Precision Engineering*, 46:34 – 47, 2016.

[112] T. Vaudrey and R. Klette. Computer Analysis of Images and Patterns. *Computer Analysis of Images and Patterns*, 5702:541–548, 2009.

[113] A. Veeraraghavan, R. Raskar, A. Agrawal, A. Mohan, and J. Tumblin. Dappled photography: Mask enhanced cameras for heterodyned light fields and coded aperture refocusing. *ACM Trans. Graph.*, 26(3), July 2007.

[114] Verband. Vdi / Vde 2634 Part III. *VDI*, pages 1–20, 2011.

[115] Verband. Vdi / Vde 2634 Part II. *VDI*, pages 1–16, 2012.

[116] J. Wang, R. K. K. Leach, and X. Jiang. Review of the mathematical foundations of data fusion techniques in surface metrology. *Surface Topography: Metrology and Properties*, 3(2), 2015.

[117] X. Wang, L. Li, and G. Hou. High-resolution light field reconstruction using a hybrid imaging system. *Appl. Opt.*, 55(10):2580–2593, Apr 2016.

[118] X. Wang, J. Liu, S. Liu, P. Jin, T. Wu, and Z. Wang. Accurate radius measurement of multi-bend tubes based on stereo vision. *Measurement*, 117:326 – 338, 2018.

[119] A. Weckenmann, X. Jiang, K. D. Sommer, U. Neuschaefer-Rube, J. Seewig, L. Shaw, and T. Estler. Multisensor data fusion in dimensional metrology. *CIRP Annals - Manufacturing Technology*, 58(2):701–721, 2009.

[120] D. Weimer, H. Thamer, C. Fellmann, M. Lütjen, K. D. Thoben, and B. Scholz-Reiter. Towards 100% in-situ 2D/3D quality inspection of metallic micro components using plenoptic cameras. *Procedia CIRP*, 17:847–852, 2014.

[121] Z. Xiao, J. Liang, D. Yu, Z. Tang, and A. Asundi. An accurate stereo vision system using cross-shaped target self-calibration method based on photogrammetry. *Optics and Lasers in Engineering*, 48(12):1252–1261, 2010.

[122] Y. Xu, Y. Zhao, F. Wu, and K. Yang. Error analysis of calibration parameters estimation for binocular stereo vision system. *IST 2013 - 2013 IEEE International Conference on Imaging Systems and Techniques, Proceedings*, pages 317–320, 2013.

[123] Z. Xu, J. Ke, and E. Y. Lam. High-resolution lightfield photography using two masks. *Opt. Express*, 20(10):10971–10983, May 2012.

[124] P. Yang, Z. Wang, Y. Yan, W. Qu, H. Zhao, A. Asundi, and L. Yan. Close-range photogrammetry with light field camera: from disparity map to absolute distance. *Appl. Opt.*, 55(27):7477–7486, Sep 2016.

[125] X. Yang and S. Fang. Effect of field of view on the accuracy of camera calibration. *Optik - International Journal for Light and Electron Optics*, 125(2):844–849, 2014.

[126] Y. Yin, M. J. Ren, L. Sun, and L. Kong. Gaussian process based multi-scale modelling for precision measurement of complex surfaces. *CIRP Annals - Manufacturing Technology*, 65(1):487–490, 2016.

[127] N. Zeller, F. Quint, and U. Stilla. Calibration and accuracy analysis of a focused plenoptic camera. *ISPRS Annals of Photogrammetry, Remote Sensing and Spatial Information Sciences*, II-3(September):205–212, 2014.

[128] S. Zhang. Absolute phase retrieval methods for digital fringe projection profilometry: A review. *Optics and Lasers in Engineering*, 107:28 – 37, 2018.

[129] Y. Zhang, H. Lv, Y. Liu, H. Wang, X. Wang, Q. Huang, X. Xiang, and Q. Dai. Light Field Depth Estimation via Epipolar Plane Image Analysis and Locally Linear Embedding. *IEEE Transactions on Circuits and Systems for Video Technology*, 8215(c):1–1, 2016.

[130] Z. Zhang. Flexible camera calibration by viewing a plane from unknown orientations. *Proceedings of the Seventh IEEE International Conference on Computer Vision*, 1:666–673 vol.1, 1999.

[131] Z. Zhang. Camera Calibration. *Emerging Topics in Computer Vision, Prentice Hall Professional Technical Reference*, pages 4–43, 2004.

[132] Y. Zhou, C. Sun, Y. Song, and J. Chen. Image pre-filtering for measurement error reduction in digital image correlation. *Optics and Lasers in Engineering*, 65:46 – 56, 2015. Special Issue on Digital Image Correlation.